

DESIGN AND EXPERIMENTAL ANALYSIS OF MECHANICAL FORCE
GENERATORS FOR PERFORMANCE IMPROVEMENT OF MACHINES

A THESIS SUBMITTED TO
THE GRADUATE SCHOOL OF NATURAL AND APPLIED SCIENCES
OF
MIDDLE EAST TECHNICAL UNIVERSITY

BY

MEHMET BURAK EKİNCİ

IN PARTIAL FULFILLMENT OF THE REQUIREMENTS
FOR
THE DEGREE OF MASTER OF SCIENCE
IN
MECHANICAL ENGINEERING

AUGUST 2019

Approval of the thesis:

DESIGN AND EXPERIMENTAL ANALYSIS OF MECHANICAL FORCE GENERATORS FOR PERFORMANCE IMPROVEMENT OF MACHINES

submitted by **MEHMET BURAK EKİNCİ** in partial fulfillment of the requirements for the degree of **Master of Science in Mechanical Engineering Department, Middle East Technical University** by,

Prof. Dr. Halil Kalıpçılar
Dean, Graduate School of **Natural and Applied Sciences**

Prof. Dr. M. A. Sahir Arıkan
Head of Department, **Mechanical Engineering**

Prof. Dr. Reşit Soylu
Supervisor, **Mechanical Engineering, METU**

Assist. Prof. Dr. Ulaş Yaman
Co-Supervisor, **Mechanical Engineering, METU**

Examining Committee Members:

Assoc. Prof. Dr. Ergin Tönük
Mechanical Engineering, METU

Prof. Dr. Reşit Soylu
Mechanical Engineering, METU

Assist. Prof. Dr. Ulaş Yaman
Mechanical Engineering, METU

Assist. Prof. Dr. A. Buğra Koku
Mechanical Engineering, METU

Assist. Prof. Dr. Kutluk Bilge Arıkan
Mechanical Engineering, TED University

Date: 27.08.2019

I hereby declare that all information in this document has been obtained and presented in accordance with academic rules and ethical conduct. I also declare that, as required by these rules and conduct, I have fully cited and referenced all material and results that are not original to this work.

Name, Surname: Mehmet Burak EKİNCİ

Signature:

ABSTRACT

DESIGN AND EXPERIMENTAL ANALYSIS OF MECHANICAL FORCE GENERATORS FOR PERFORMANCE IMPROVEMENT OF MACHINES

EKİNCİ, Mehmet Burak
Master of Science, Mechanical Engineering
Supervisor: Prof. Dr. Reşit Soylu
Co-Supervisor: Assist. Prof. Dr. Ulaş Yaman

August 2019, 199 pages

Recently, a novel overconstrained mechanism with favorable dynamic properties, namely the MFG (Mechanical Force Generator), has been proposed. This mechanism can provide a desired mechanical force, or power variation depending on the position of its input links. This power profile can be adjusted in order to improve the performance of a machine and its actuators that are connected to the MFG. In previous works, determination of an optimum power profile for the MFG and determination of the MFG design parameters have already been studied. In this thesis, previously proposed methods are improved. New methods to determine optimum power profiles for MFG, which minimize the required maximum torque, maximum power output and energy consumption of the driving actuator, are proposed. In these methods, the motion of the machine is not changed and only the power and the torque output of the motors are taken as the optimization variables. A method for determining MFG power to obtain an MFG with open slot profile links, which are easy to manufacture, is proposed. The performances of the methods proposed in this study are assessed by applying them to a case study that has been considered in a previous work. It is observed that, for this case study, the performances of the proposed methods are better.

In this thesis, the problem of determining the design parameters of MFG is also studied. It is pointed out that in order to generate an MFG power profile, MFG can be designed with either compression or tension springs. An improved algorithm which yields the design parameters of MFG is proposed.

For the experimental verifications, a symmetrical slider-crank mechanism is used as a machine. A spring is placed between two sliders of the machine to simulate a conservative external load; and an appropriate MFG is designed for the aforementioned machine. An experimental setup is constructed to test the performance of the MFG. It has been shown via simulations and experiments that performance of a machine can be improved extensively by coupling a properly designed MFG to the machine.

Keywords: Mechanical Force Generators, Performance Optimization, Planar Mechanisms

ÖZ

MAKİNELERİN PERFORMANSLARININ ARTIRILMASI İÇİN MEKANİK KUVVET JENERATÖRLERİNİN TASARLANMASI VE DENEYSEL OLARAK İNCELENMESİ

EKİNCİ, Mehmet Burak
Yüksek Lisans, Makina Mühendisliği
Tez Danışmanı: Prof. Dr. Reşit Soylu
Ortak Tez Danışmanı: Dr. Öğr. Üyesi Ulaş Yaman

Ağustos 2019, 199 sayfa

Son zamanlarda, dinamik açıdan faydalı özelliklere sahip, fazla kısıtlı düzlemsel bir mekanizma olan Mekanik Kuvvet Jeneratörü (MKJ) önerilmiştir. Bu mekanizma, uzuvlarının verilen pozisyona göre istenen güç çıktısını sağlayabilmektedir. MKJ'nin sağlayacağı güç çıktısı ayarlanarak makinelerin ve buna bağlı olan eyleyicilerin performansı artırılabilir. Önceki çalışmalarda MKJ için optimum bir güç çıktısı bulmak ve MKJ'nin parametrelerinin belirlenmesi için yöntemler önerilmiştir.

Bu çalışmada ise önceden önerilmiş olan yöntemler iyileştirilmiştir ve yeni yöntemler önerilmiştir. Bir eyleyicinin en fazla güç tüketimini, anlık en fazla tork ihtiyacını ve enerji kaybını azaltmak için MKJ optimum bir güç çıktısı bulan üç ayrı performans iyileştirme yöntemi önerilmiştir. İyileştirme yöntemlerinde makinelerin çalışma rejimi değiştirilmemiştir. İyileştirmede tasarım değişkeni olarak eyleyicinin aktardığı güç veya tork kullanılmıştır. Üretimi ve uygulaması kolay olan MKJ uzvunun tasarımı ele alınmıştır. Önerilen yöntemler önceden uygulanmış çalışmalarla karşılaştırılmış ve daha iyi sonuçlar elde edilmiştir.

Bu çalışmada MKJ tasarım parametrelerinin belirlenmesi de ele alınmıştır. MKJ tasarım parametrelerinin belirlenmesi için bir algoritma önerilmiştir.

MKJ tasarımının deneysel olarak dođrulanması için simetrik krank-biyel mekanizması makine olarak kullanılmıştır. Makineye korunumlu kuvvet uygulayan dış yük olarak da mekanizmanın iki kaydırıcı uzvu arasına yay yerleştirilmiştir. Bu makine için matematiksel durum çalışması olarak uygun bir MKJ tasarımı yapılmıştır. Tasarlanan MKJ'nin deneysel olarak performansının incelenmesi için deney düzeneđi hazırlanmıştır. Yapılan deneylerle ve simülasyonlarla uygun bir MKJ kullanılarak makinelerin performansının büyük ölçüde artırılabilceđi gösterilmiştir.

Anahtar Kelimeler: Mekanik Kuvvet Jeneratörleri, Performans Eniyilemesi, Düzlemsel Mekanizmalar

To my family

ACKNOWLEDGEMENTS

I would like to thank my supervisor Prof. Dr. Reşit Soylu and my co-supervisor Assist. Prof. Dr. Ulaş Yaman for their guidance, support, encouragement throughout the study.

I would like to thank my co-advisor for manufacturing some components of the symmetrical slider-crank mechanism from a 3D printer.

I would like to thank my brother Mustafa Ekinci for his guidance and valuable comments on the manufacturing and assembly of the experimental setup components. Thanks to Ünal Pehlivan from Lamasan company for his valuable assistance on manufacturing the crank assembly and other components. Thanks to Harun Kozan for his tedious work manufacturing the components. I would like to thank Kemal Özer from Küçükpazarlı company to produce slot profile links with CNC machine.

I would like to thank Berk Yurttagül for helping me to find the DC motor, to find encoder boards of the DC motor and giving me his encoder counter board. Also, thanks to him for helping me in controller and estimator design.

I would like to thank my colleagues Önder Tetik, Mustafa Yavuz Öztürk, Ersin Söken, Biter Boğa İnaltekin, Yusuf Acar and Polat Poşpoş for encouraging me and helping me in various parts of the thesis.

The last, but the most important, I would like to thank my parents Ayşe Ekinci and Eyüp Ekinci for their endless love and support.

TABLE OF CONTENTS

ABSTRACT.....	v
ÖZ	vii
ACKNOWLEDGEMENTS	x
TABLE OF CONTENTS	xi
LIST OF TABLES	xviii
LIST OF FIGURES	xx
LIST OF ABBREVIATIONS	xxv
LIST OF SYMBOLS	xxvi
CHAPTERS	
1. Introduction.....	1
1.1. Description of the MFG Model	2
1.2. MFG Properties and Constraints	5
1.2.1. The Special Dimensions	5
1.2.2. Kinematic Relations.....	7
1.2.2.1. Position Relations	7
1.2.2.2. Velocity Relations.....	7
1.2.3. Constraints on the Mass Parameters	9
1.2.4. Constraints on the External Forces	9
1.2.5. MFG Power Output Constraints	12
1.3. MFG Design Methods	13

1.3.1. Determining Optimum Force Variations.....	13
1.3.2. Determining Design Parameters of the MFG.....	17
1.3.2.1. Open and Closed Type Slot Profiles.....	18
1.3.2.2. One-Sided Slots	20
1.3.2.3. Alternative MFG Configurations Depending on Joint Type between Slot Profile and Ground Links	21
1.4. MFG Experimental Analyses.....	23
1.5. Contributions of the Thesis	23
1.6. Organization of the Thesis	25
2. Design of Mechanical Force Generators	27
2.1. Introduction.....	27
2.2. Additional Parameters Used in the Design of MFG	27
2.3. Work-Energy Equations for MFG	29
2.3.1. Extension Springs with Initial Tension	30
2.3.2. Representation of Roller Angular Speed.....	33
2.3.3. Design Equations Based on Virtual Spring Elongation	34
2.4. Parameter Design Suggestions.....	37
2.5. Iterative Solution Method for Spring Length Profile Calculation	39
2.6. Centerline and Contact Curve Calculation on Slot Profile Links	41
2.7. Dynamic Force Analysis.....	43
2.8. Radius of Curvature Consideration.....	46
3. Performance Optimization of Machines Using Mechanical Force Generators.....	47
3.1. Introduction.....	47
3.2. Definition of a Mechanical System to be Optimized	48

3.2.1. Power Transmission Equations.....	48
3.2.2. Motor Based Losses.....	52
3.2.2.1. Copper Losses and Speed Related Losses	54
3.2.2.2. Motor Brake Related Losses	55
3.2.2.3. Motor Driving Related Losses	57
3.2.3. Machine and MFG Losses	58
3.3. MFG Power Flow Design.....	58
3.3.1. Performance Optimization Guideline	59
3.3.2. Performance Measures of the Optimization	59
3.3.3. Performance Optimization with MFG's	61
3.3.3.1. Minimizing the Maximum Power Requirement	61
3.3.3.2. Minimizing the Maximum Torque.....	62
3.3.3.3. Minimizing the Copper Losses on the Motor	64
3.3.4. Zero-Speed Crossing Compensation	67
3.3.5. Energy Drift Compensation.....	70
3.4. MFG Design with Open Slot Profile.....	70
3.4.1. Open Slot Profile Determination	71
3.4.2. Conversion to Open Profiles.....	76
3.4.2.1. Design Guideline.....	76
3.4.2.2. One-Pass-One-Return Condition for Link 2 Motion	77
3.4.2.3. Symmetrizing the Energy Profile.....	77
3.5. Application of the Methods.....	79
3.5.1. Description of the Machine and the Load Force.....	79
3.5.2. MFG Power Design for the Machine.....	83

3.5.2.1. Application of the Optimization Methods	83
3.5.2.2. Application of the Zero Crossing Compensation Method.....	86
3.5.2.3. Application of the Energy Drift Compensation.....	87
3.5.2.4. Performance Comparison with the Previous Method.....	88
3.5.2.5. Slot Profile of the Design	90
3.5.3. Conversion of the Design to Open Slot Profile.....	91
3.5.3.1. Slot Profile of the Design	94
3.6. Discussion of Results	94
4. Mathematical Case Study	97
4.1. Introduction.....	97
4.2. Description of the Machine.....	98
4.2.1. Description of Shared Links of the Machine with MFG.....	99
4.2.2. Description of Reference Frames	100
4.2.3. Crank & Coupler Links	101
4.2.4. Slider	101
4.2.4.1. Friction Forces	101
4.2.4.2. Load Forces	102
4.2.5. Dynamic Analysis of the Machine	103
4.3. Simulation Conditions and Parameter Sets.....	104
4.3.1. Simulation Conditions and Parameter Set for the Machine	104
4.3.2. Parameter Set for MFG design.....	105
4.4. Performance of the Machine without MFG	107
4.5. MFG Power Variation Design	109
4.6. MFG Design.....	113

4.6.1. Design with Different Spring Preload Values	113
4.6.1.1. Design Using Minimum Spring Preload Length.....	114
4.6.1.2. Re-design by Adjusting Spring Preload Length	116
5. Experimental Setup Design	121
5.1. Introduction	121
5.2. Mechanical Design	121
5.2.1. Symmetrical Slider Crank Design	122
5.2.1.1. Problem Statement	122
5.2.1.2. Crank Design.....	126
5.2.1.3. Coupler Design	127
5.2.1.4. Slider-Coupler Connection Design	129
5.2.1.5. Motor Bracket	130
5.2.1.6. Extra Mass Option on the Sliders	130
5.2.1.7. Spring Option between Sliders	132
5.2.1.8. Rail Cart System	132
5.2.2. MFG Design	134
5.2.2.1. Problem Statement	134
5.2.2.2. MFG Slider Alignment	135
5.2.2.3. Reducing the Preload on Sliding Rails	136
5.2.2.4. Cylinder in slot joint option for MFG	137
5.2.2.5. Spring Connections	137
5.3. Experimental Setup Electronical Hardware	139
5.3.1. Problem Statement.....	139
5.3.2. Electronic Hardware Configuration.....	141

5.3.3. Motor	141
5.3.4. DC Motor Driver	144
5.3.5. Current Sensing	147
5.3.6. Microcontroller.....	147
5.4. Experimental Setup Software.....	147
5.4.1. Problem Statement	148
5.4.2. Real-time operation	148
5.4.3. Data transfer	149
5.4.4. Position & Velocity Estimation.....	150
5.4.5. Control algorithm	152
5.4.6. LabVIEW Current Reading.....	153
5.4.7. Software Use Case.....	154
6. Experimental Case Study	157
6.1. Introduction.....	157
6.2. Description of Test Cases	157
6.3. Initial Conditions Associated with the Experiments.....	159
6.4. Control Performance Analysis of the MFG Design.....	161
6.5. Power Analysis for the MFG	166
6.5.1. Motor Power Consumption Calculation of the Experiments	166
6.5.2. Comparison of the Experimental Motor Power with the Motor Power Obtained from the Simulations.....	168
6.5.3. Comparison of Experimental Results with Each Other.....	170
6.6. Energy Consumption Analysis of the MFG.....	172
6.6.1. Energy Consumption Calculation of the Experiments	172

6.6.2. Comparison of the Results	175
6.7. Maximum Torque and Maximum Power Results	178
6.8. Performance Improvement Analysis	179
6.8.1. Definition of Performance Measures	180
6.8.2. Evaluation of the Performance Measures	182
6.8.3. Comparison of MFG Performance with the Motor Braking Methods....	183
6.9. Additional Experiments by Using Regular MFG.....	185
6.10. Discussion of Results	186
7. Conclusions.....	189
REFERENCES.....	193
APPENDICES	
A. CAD Drawing of Symmetrical Slider Crank Machine with MFG.....	197
B. Important Dimensions of the MFG from CAD file	199

LIST OF TABLES

TABLES

Table 3.1. η values for different braking types.....	56
Table 3.2. Specifications of the machine in [4]	80
Table 3.3. Minimum values of the performance measures for the optimization algorithms	86
Table 3.4. Performance measures of the MFG power design.....	88
Table 3.5. Minimum values of JP	89
Table 3.6. Minimum values of ξE which minimizes the total energy consumption .	90
Table 3.7. Performance measures for open slot profile MFG design	93
Table 4.1. Parameters and initial conditions used in simulations (for the machine)	105
Table 4.2. Available parameters and design parameters for the MFG	106
Table 4.3. Minimum values of the performance measures.....	112
Table 5.1. Hardware components used in the experiment.....	142
Table 5.2. DC motor important properties without considering gearbox [11]	143
Table 5.3. Data packet contents to be sent at each period	149
Table 5.4. Software modes of the microprocessor	154
Table 6.1. Descriptions of the six different cases	158
Table 6.2. Initial conditions associated with the six experimental cases.....	159
Table 6.3. Controller Parameters	160
Table 6.4. Energy consumption values (in Joules) of the DC motor obtained from simulations and the experiment results.....	175
Table 6.5. Maximum torque and Powers of simulations and the experiments.....	179
Table 6.6. Performance indices of the simulations and experiments at $\omega_{ref} = 0.1$ rev/s using Cases 1, 5 and 6.....	183
Table 6.7. Performance indices of the simulations at $\omega_{ref} = 1$ rev/s.....	183

Table 6.8. Motor energy consumption of a motor without copper losses (in Joules) for different braking methods	185
Table 6.9. Work done by motor in one period (in Joules)	186
Table 6.10. Performance indices obtained from experiment results	186

LIST OF FIGURES

FIGURES

Figure 1.1. Mechanical Force Generator model	2
Figure 1.2. Partial view of MFG slot profile roller contact to show the velocity constraint.....	8
Figure 1.3. MFG connection methods given in [3]	10
Figure 1.4. MFG connection by using Rack and Pinion mechanism [3].....	11
Figure 1.5. Symmetrical Slider Crank Mechanism used as a machine	11
Figure 1.6. Optimum MFG force search method in [4].....	16
Figure 1.7. Open and closed type slot profiles according to the definition	18
Figure 1.8. A Closed type slot profile [4]	19
Figure 1.9. Slot profiles with one-sided and two-sided slots.....	20
Figure 2.1. Design parameters used in MFG	28
Figure 2.2. Elongation (d), virtual elongation (y) and spring length ($lmfg$) vs spring force ($Fs3$) graphs for the extension springs with initial tension.....	32
Figure 2.3. Elongation (d), virtual elongation (y), spring length ($lmfg$) and virtual elongation at free length ($d0$)	32
Figure 2.4. Roller centerline relative velocity	33
Figure 2.5. Demonstration for calculation of slot profile links contact points	43
Figure 2.6. Free Body Diagram of link 3.....	45
Figure 3.1. Power flow diagram	49
Figure 3.2. DC Motor mathematical model.....	53
Figure 3.3. Permanent DC motor power losses [7]	54
Figure 3.4. DC Motor current ripple experiment with %50 Duty cycle and 20 kHz PWM frequency.....	58
Figure 3.5. Approximation method proposed in [3]	68
Figure 3.6. Approximation method used in this study.....	69

Figure 3.7. The pass and return times for arbitrary periodic s_2 variable.....	72
Figure 3.8. Demonstration of one pass one return type motion	77
Figure 3.9. Sketch of the slider-crank mechanism.....	79
Figure 3.10. Force vs compression distance plot	81
Figure 3.11. Motor torque vs time plot	82
Figure 3.12. Task force, slider velocity and task power vs time plot	82
Figure 3.13. Task, optimum motor, and optimum MFG powers vs time plot	83
Figure 3.14. Optimum motor torque and the task torque vs time plot.....	84
Figure 3.15. Asymptotic discontinuities of the optimum MFG force.....	85
Figure 3.16. Work done by the original mechanism (W_{task}), work done by the optimum motor torque and work done by the optimum MFG force (W_{mfg}^*) vs time plot	85
Figure 3.17. Approximation of the asymptotic discontinuities for the critical times t_{cr1} and t_{cr2}	86
Figure 3.18. The deviation from the conservative work	87
Figure 3.19. The energy drift compensation at t_{cr2}	88
Figure 3.20. Output variables of the MFG power design (T_{motor} , F_{mfg} , P_{motor} , W_{mfg}).....	89
Figure 3.21. Spring elongation vs slider position	91
Figure 3.22. Open slot profile check results	92
Figure 3.23. Even and odd functions of the W_{mfg}	93
Figure 3.24. Results of open slot profile conversion	93
Figure 3.25. Spring elongation vs slider position (similar to the path that the center of the roller follows on link 3).....	94
Figure 4.1. Sketch of the symmetrical slider-crank mechanism, with link numbers, external forces applied on the mechanism (optional force vectors are given with dashed arrows), reference points and reference frames	98
Figure 4.2. Slider position (s_2) and velocity (\dot{s}_2) with respect to time for the symmetrical slider-crank mechanism.....	107

Figure 4.3. u_{11} components of symmetric slider crank spring load and friction force vectors on link 2.....	108
Figure 4.4. Torque (T_{motor}) and power requirement from motor (P_{motor}) without MFG.....	109
Figure 4.5. Torque, Force Power and Energy distribution between the MFG and the Motor (for all performance optimization methods in Section 3.3.3).....	112
Figure 4.6. Open slot profile feasibility test (First two steps in section 3.4.2.1).....	113
Figure 4.7. MFG Spring length vs link 2 position plot for minimum preload	115
Figure 4.8. A possible shape for link 3 (to scale)	115
Figure 4.9. A CAD view of the shape of link 3 (designed with minimum preloaded spring length).....	116
Figure 4.10. Slot profile contact surface normal forces, horizontal and vertical components vs s_2	117
Figure 4.11. MFG Spring length vs link 2 position plot for adjusted preload.....	118
Figure 4.12. To scale shape of link 3 to be used in the experiment.....	118
Figure 4.13. Slot profile contact surface normal forces, horizontal and vertical components	119
Figure 4.14. CAD design of the shape of link 3	119
Figure 4.15. The radius of curvature of the slot centerline.....	120
Figure 5.1. Alignment problem in the identical slider-crank mechanisms.....	123
Figure 5.2. Symmetrical slider-crank mechanism schematics (solution to alignment of slider-ground prismatic joints).....	123
Figure 5.3. Frame used in the experiment of the previous study [3].....	124
Figure 5.4. The estimated available region for symmetrical slider-crank mechanism (shown with the top and front view of the experimental setup CAD model).....	125
Figure 5.5. Cross-section and isometric view of the crank assembly.....	127
Figure 5.6. Coupler CAD model, grooves at the endpoints are designed to insert bearings.....	127
Figure 5.7. Coupler and Crank CAD model, design with zero play tolerance at two zones which are vulnerable to collision.....	128

Figure 5.8. Slider Mount CAD model.....	129
Figure 5.9. Increased play tolerance by fixing bearing at the slider mount such that crank and coupler is slightly tilted.	130
Figure 5.10. The symmetrical slider crank system used in experiment.....	131
Figure 5.11. Spring coefficient measurement	132
Figure 5.12. Recirculation of balls on a linear bearing [15]	133
Figure 5.13. Over-constrain problem due to the misalignment	135
Figure 5.14. Cross-section of sliding rail	136
Figure 5.15. Cylinder in slot option to slot profile – ground joint.....	137
Figure 5.16. Spring coefficient measurement	138
Figure 5.17. MFG spring endpoints on the ground link side	138
Figure 5.18. MFG spring endpoints on link 3 side	139
Figure 5.19. Hardware schematics of the experimental setup	141
Figure 5.20. Electronic hardware of the experimental setup	143
Figure 5.21. DC Motor assembly with its components.....	144
Figure 5.22. DC Motor speed-time plot for various duty cycles (in percent).....	146
Figure 5.23. H Bridge with Flyback diodes	146
Figure 5.24. Speed estimator performance comparison of the Tustin and Backward Euler Methods (right plot is the zoomed version of the left one)	151
Figure 5.25. Acceleration estimation performance using the Tustin method (right plot is the zoomed version of the left one)	152
Figure 5.26. The control system block diagram.....	152
Figure 5.27. LabVIEW software block diagram.....	153
Figure 6.1. Experimental setup for Case 2.....	161
Figure 6.2. Experimental setup for Case 4.....	162
Figure 6.3. Percent error of motor shaft rotational speed	163
Figure 6.4. Controller Duty for each case and for each reference speed	164
Figure 6.5. DC Motor model used in experimental calculations	166
Figure 6.6. Motor output power of the experiments and the simulations	169
Figure 6.7. Time-shift demonstration for Case 2.....	170

Figure 6.8. Motor output power comparison of the experimental cases 1, 2 and 3.	171
Figure 6.9. Motor output power comparison of the experimental cases 4, 5 and 6.	172
Figure 6.10. Circuit diagram for energy consumption calculation	173
Figure 6.11. P in equation (3.24) vs time plot	184
Figure 6.12. Power consumption of a motor without copper losses for different braking methods.....	185
Figure A.1. Front view of the system from the CAD drawing	197
Figure A.2. Top view of the system from the CAD drawing	198

LIST OF ABBREVIATIONS

Abbreviation	Definition
DOF	Degree of Freedom
MFG	Mechanical Force Generator
RMS	Root mean square
PWM	Pulse Width Modulation
SI	International System of Units
DC	Direct Current
ABS	Acrylonitrile Butadiene Styrene
emf	Electromotive force

LIST OF SYMBOLS

Symbol	Definition
A	Coefficient of y^2 terms (in equation of motion of y)
B	Coefficient of \dot{y}^2 terms (in equation of motion of y)
B'	Coefficient of \dot{s}_2^2 terms (in equation of motion of y)
b_i	MFG design dimensions related to link i
\vec{c}	Position vector of roller 6 with respect to link 3 origin
c_x	$\vec{u}_1^{(3)}$ component of \vec{c}
c_y	$\vec{u}_1^{(3)}$ component of \vec{c}
c_1	Motor constant friction coefficient
c_2	Motor velocity dependent friction coefficient
d	Spring elongation (from its free length)
d_0	Virtual spring elongation at springs free length, for the extension springs with initial tension (0 for other spring types)
E_{mfg}	Mechanical energy of the MFG
E_{spring}	Energy of spring(s) connected between link 3 and ground
$E_{k,roller}$	Kinetic energy of a roller
E_{mfg0}	Initial mechanical energy of MFG at t_0
$E_{machine}$	Mechanical energy of the machine
$\dot{E}_{machine}$	Rate of change of mechanical energy of the machine
E_{motor}^e	Experimentally calculated motor energy consumption in one period
E_{motor}	Motor energy consumption calculated by simulation (at the end of period)
E_{in}	Driver energy consumption calculated by simulation (at the end of period)

E_{out}	Total work done by the system on output in one period
E_s^e	Experimentally calculated energy output of power supply in one period
E_{in}^e	Experimentally calculated energy output of driver in one period
\mathcal{F}_i	Reference frame of link i
\vec{F}_i	Force applied on link i
F_{s10}	Initial tension of spring connected to link i
F_{s3}	Force applied by spring to link 3
\vec{F}_{ij}	Force applied by link i to link j
F_{ijx}	x component of the force vector \vec{F}_{ij} (in reference frame i)
F_{ijy}	y component of the force vector \vec{F}_{ij} (in reference frame i)
F_{ijz}	z component of the force vector \vec{F}_{ij} (in reference frame i)
F_{task}	Virtual Force applied on the machine output link which drives the mechanism to accomplish a task, when motor torque is zero (without the aid of MFG)
F_{mfg}	Combined force output applied by MFG input links on the machine
F_{motor}	Virtual Force that appears at the machine output link to drive the machine and external load, when MFG is connected
F_{mfg}^*	Optimum MFG force variation output of the optimization methods
F'_{mfg}	Motor force variation output of the zero-crossing compensation method
f_e	Even part of a function f
f_{odd}	Odd part of a function f
F_{load}	External load on slider crank press
\vec{F}_{f2}	Friction force vector applied on link 2
f_{14}	Magnitude of \vec{F}_{f2}

\vec{F}_{si}	Force applied by spring on link i
F_{s2}	$-\vec{u}_1^{(1)}$ component of \vec{F}_{si}
F_{s20}	Initial tension force on the spring between link 2 and link 4
H	A functional
H^*	Augmented function
I_i	Inertia of link i , with respect to center of mass
i_m	Current passing through motor terminals
J_P	A performance measure for minimizing the maximum power output of motor
J_T	A performance measure for minimizing the maximum torque output of motor
J_E	A performance measure for minimizing the total energy consumption of motor
K	DC motor copper loss coefficient including gear ratio
k_E	Motor back electromotive force constant
k_T	Motor torque constant
k_i	Stiffness of the springs connected to link i ($i=3$ or $i=5$)
k_{sc}	Stiffness of spring between link 2 and link 4
L	Inductance of DC motor
l_{mfg}	Spring length of MFG
$l_{free,mfg}$	Free length of the springs on the MFG
$l_{mfg0min}$	Initial spring length when link 2 velocity is zero (with minimum preload design)
l_{mfg0}	Initial spring length when link 2 velocity is zero (with arbitrary preload design)
l_{crank}	Crank link length measured between its two revolute joints

$l_{coupler}$	Coupler link length measured between its two revolute joints
l_s	Length of the load spring connected between link 2 and link 4
$l_{o,sc}$	Spring hook connection offset to slider motion s_2 reference point on link 2
l_{sc}	Elongation of the spring between link 2 and link 4
$l_{free,sc}$	Free length of the spring between link 2 and link 4
m_i	Mass of link i
\mathcal{N}	The domain of natural numbers
O_i	Origin of the reference frame of link i
p	Slope of tangent of roller – slot profile contact
\vec{p}	Tangent unit vector of the slope between roller and link 3 contact
\vec{p}_β	Vector obtained by rotating the p vector β degrees with respect to the z-axis of link 3 reference frame
P_{in}	Power input of the motor
P_{mfg}	Power output of the MFG
P_{motor}	Mechanical power transmitted by the motor to the machine
$P_{loss,motor}$	Power loss of the motor
$P_{machine}$	Power output of the machine
$P_{loss,machine}$	Power loss of the machine
$P_{loss,mfg}$	Power losses of MFG
P_{out}	Power required from a machine (with or without MFG) to drive an external load
P_{task}	Motor power required to run a task when MFG is not connected,
$P_{loss,copper}$	Motor copper losses

P_{motor}^*	Optimum motor power variation output of the optimization methods
P'_{mfg}	MFG power variation output of the zero-crossing compensation method
P_{mfg}^*	Optimum MFG power variation output of the optimization methods
P'_{motor}	Motor power variation output of the zero-crossing compensation method
P_{motor}^e	Experimentally calculated motor output power
R	Resistance between DC motor terminals
R_{ij}	The j^{th} reference point on link i
r_i	The radius of roller i (Links 6 to 9)
s_2	Machine output link position (MFG link 2 position)
\dot{s}_2	Machine output link velocity (MFG link 2 velocity)
s_3	MFG slot profile link position
\dot{s}_3	MFG slot profile link velocity
s_f	Forging stroke of a slider-crank press
s_c	Compression length of a slider-crank press
s_{2max}	The maximum of link 2 position
T	Period of the task
t^*	Time at which link 2 velocity is zero
t_{cri}	i^{th} time at which the velocity of link 2 (\dot{s}_2) is zero or motor shaft speed (ω) is zero
t_{sp}	Specified time interval to be used in the asymptotical discontinuity approximation
T_f	Motor friction torque
T_{motor}	Net output torque of motor

T_{motor}^*	Optimum motor torque variation output of the optimization methods
T'_{motor}	Motor torque variation output of the zero-crossing compensation method
T_{task}	Motor torque applied on the motor shaft which drives the mechanism to accomplish a task, without the aid of MFG
$\vec{u}_1^{(i)}$	Unit vector in direction of +x-axis of reference frame of link i
$\vec{u}_2^{(i)}$	The unit in direction of +y-axis of reference frame of link i
$\vec{u}_3^{(i)}$	The unit vector in direction of +z-axis of reference frame of link i
V_{in}	Input voltage
V_{emf}	Potential difference caused by back electromotive force of a DC motor
v_t	Velocity of roller center (with respect to link 3 reference frame)
W_{mfg}	Work done by the MFG on the machine (from an initial time to the current time)
$W_{mfg,even}$	Even part of work done by MFG
$W_{mfg,odd}$	Odd part of work done by MFG
y	MFG spring elongation from its virtual free length, for the extension springs with initial tension (equal to d for other spring types)
\dot{y}	Rate of change of y with respect to time
y_0	Initial MFG spring preload from its virtual free length (taking initial tension into account)
$y_{@i}$	Variation of variable y in i^{th} iteration
$\dot{y}_{@i}$	Variation of variable \dot{y} in i^{th} iteration
Δs_3	Change between the maximum and the minimum values of s_3
Δs_{3max}	Maximum change between the maximum and the minimum values of s_3 , with minimum preload design
ϵ	Error term for the iterative approach to determine spring length profile
ϵ_{max}	Threshold for the error term ϵ

θ, ϕ	Crank and coupler angles
θ_{enc}	Position measurement from the encoder
λ	A Lagrange multiplier
τ_e	Electrical time constant of a DC motor
$\dot{\psi}_i$	Magnitude of roller i's angular speed
ω	Motor output shaft rotational speed (Including gearbox if connected)
$\hat{\omega}$	Estimated motor shaft speed
ω_{ref}	Reference motor shaft speed

CHAPTER 1

INTRODUCTION

Mechanisms are widely used in industry for various types of tasks. In order to perform these tasks, actuators are employed. Depending on the task, the actuators supply a specific amount of torque/force and power. Moreover, the actuators also compensate for the losses at the machine and the actuator itself. A company that executes a given task, pays for the actuators and their energy consumption. Therefore, it is important studying to reduce the cost of actuators and their energy consumption while performing the same task.

In order to improve the performance of machines, recently, Soylu [1] has proposed a novel mechanism, namely, the Mechanical Force Generator (MFG), which can provide adjustable periodic power flow through its input links. The mechanism is planar, overconstrained and one degree of freedom (DOF). When the MFG is operated in a specific way, it has been theoretically shown [2] that, MFG has favorable properties (such as having minimum friction and shaking forces and moments). Therefore, MFG can be used to improve the performance of machines connected to it.

In this chapter, firstly, MFG is introduced. Then, previously proposed methods about MFGs are investigated and the methods to be introduced in this study are discussed. In addition to the design methods, experiments conducted in the previous studies and the experimental study to be performed in this work are presented.

1.1. Description of the MFG Model

A model of the MFG is given in Figure 1.1. In the figure, link numbers are shown with balloon annotation. The notation R_{ij} corresponds to the j^{th} reference point on i^{th} link. The reference frame for links 2, 3, 4 and 5 are given in the figure. Origin of the i^{th} link's reference frame is denoted as O_i . The unit vectors on the x, y and z axes of the reference frame of the i^{th} link are labelled with $\vec{u}_1^{(i)}$, $\vec{u}_2^{(i)}$ and $\vec{u}_3^{(i)}$, respectively. The reference frame of the i^{th} link is referred as \mathcal{F}_i .

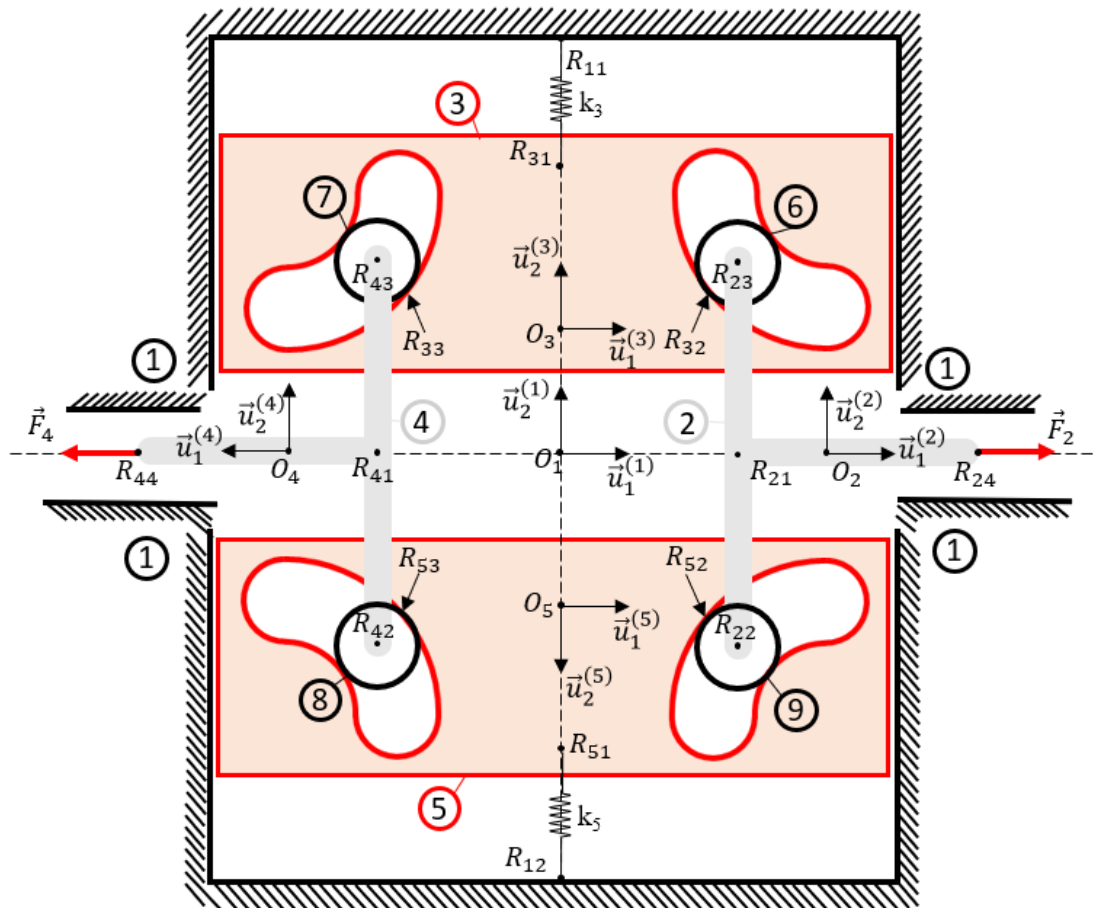


Figure 1.1. Mechanical Force Generator model

In the figure, there are 9 links in the mechanism. The reference points in the figure are placed on special positions to be explained later in the section. Therefore, the reference points and the positions of the links are described as if they are placed arbitrarily.

The links are described in the bullets below:

- **Link 1:** It is the ground link of the mechanism. In the MFG model, links 2 to 5 are connected to link 1 with prismatic joints. Links 2 & 4 can move parallel to the x-axis, links 3 & 5 can move parallel to the y-axis of \mathcal{F}_1 .

Two springs are connected between link 1 and links 3 & 5. The springs' endpoints on the ground link are the reference points R_{11} and R_{12} respectively.

- **Link 2:** It is one of the two input links of the MFG. It is connected to the ground link with a prismatic joint. The position of link 2 (s_2) is defined via the following equation.

$$s_2 = \vec{u}_1^{(1)} \cdot \overrightarrow{O_1 R_{21}} \quad (1.1)$$

where position s_2 is always assumed to be positive.

Links 6 and 9 are connected to link 2 by revolute joints at the reference points R_{23} and R_{22} respectively.

The point of application of the external force \vec{F}_2 (applied on link 2) is R_{24} .

- **Link 3:** Recall that this link is connected to the ground link by means of a prismatic joint, and it is allowed to translate in the y-axis of \mathcal{F}_1 . The position of link 3 is defined via the following equation.

$$s_3 = \vec{u}_2^{(1)} \cdot \overrightarrow{O_1 O_3} \quad (1.2)$$

where position s_3 is always assumed to be positive.

Links 6 and 7 contact link 3 at the reference points R_{32} and R_{33} respectively. Note that, as links 2 & 4 translate, the position of the contact point changes. Therefore, the reference points R_{32} and R_{33} are not fixed on link 3. The reference points R_{32} and R_{33} can be on any side of the slot.

One endpoint of the spring (on link 3) which connects link 3 and the ground link is labelled as R_{31} .

- **Link 4:** It is the other input link of the MFG. It is, again, connected to the ground link with a prismatic joint. The position of link 4 (s_4) is defined via the following equation.

$$s_4 = -\vec{u}_1^{(1)} \cdot \overrightarrow{O_1 R_{41}} \quad (1.3)$$

Similarly, s_4 is always assumed to be positive in this study.

Links 7 and 8 are connected to link 4 by revolute joints at the reference points R_{43} and R_{42} respectively.

The point of application of the external force \vec{F}_4 (applied on link 4) is R_{44} .

- **Link 5:** Similar to link 3, link 5 is connected to the ground link by means of a prismatic joint, and it is allowed to translate parallel to the y-axis of the \mathcal{F}_1 . The position of link 5 is defined via the following equation.

$$s_5 = -\vec{u}_2^{(1)} \cdot \overrightarrow{O_1 O_5} \quad (1.4)$$

Again, position s_5 is always assumed to be positive.

Links 8 and 9 contact link 5 at the reference points R_{53} and R_{52} respectively. Note that, as links 2 & 4 translate, the position of the contact point changes. Therefore, the reference points R_{53} and R_{52} are not fixed on link 5. The reference points R_{53} and R_{52} can be on any side of the slot.

One endpoint of the spring (on link 5) which connects link 5 and the ground link is labelled as R_{51} .

- **Links 6 to 9:** Links 6 to 9 are rollers. The reference points associated with these links have already been explained in the description of links 2 to 5. Therefore, they are not repeated here. The radius of each roller is labelled as r_6 to r_9 respectively.
- **Springs:** As can be seen from the figure there are two springs which connect to ground link to links 3 and 5. The stiffness of these springs are labelled as k_3 and k_5 respectively.

Throughout the study, links 3 and 5 will be referred as slot profile links. Links 2 and 4, on the other hand, will be referred as input links.

It has been shown in [3] and [4] that, according to Chebychev-Grübler-Kutzbach criterion, which is also known as the mobility formula, the DOF of MFG is 4. The calculated DOFs are the rotation freedom of the rollers. However, when there is no slippage at the roller – slot profile contact points, degree of freedom of the MFG is calculated as zero. Only with specific symmetrical dimensions of the links, the degree of freedom becomes one [2], disregarding the rollers rotation freedom. These dimensions are given in the next section.

1.2. MFG Properties and Constraints

In order to obtain 1 degree of freedom, the special dimensions suggested in [1] are repeated in subsection 1.2.1 using the notation of this study. Using the special dimensions, kinematic relations of the links are defined. Afterwards, the constraints on the masses and inertias are given in subsection 1.2.3. The additional constraints on the external forces are given in subsection 1.2.4.

When the abovementioned requirements are satisfied, disregarding the effects of gravitational acceleration, all reaction forces and moments associated with all of the 4 joints connecting the MFG to the ground will be zero. This implies that the MFG does not transmit any shaking forces or moments to the ground. Thus, it is a balanced mechanism [1]. Hence, the MFG is said to have favorable dynamical properties.

1.2.1. The Special Dimensions

The special dimensions for the overconstrained MFG with one DOF are given by the equations and statements below.

- Constraints on the shape of the input links:

$$\angle R_{24}R_{21}R_{23} = \angle R_{24}R_{21}R_{22} = \pi/2 \quad (1.5)$$

$$\angle R_{44}R_{41}R_{43} = \angle R_{44}R_{41}R_{42} = \pi/2 \quad (1.6)$$

$$\overline{R_{21}R_{23}} = \overline{R_{21}R_{22}} = \overline{R_{41}R_{43}} = \overline{R_{41}R_{42}} \quad (1.7)$$

- Constraints on the link reference frame axes:

- x-axes of \mathcal{F}_2 and \mathcal{F}_4 must be collinear with the x-axis of \mathcal{F}_1 (1.8)

- The reference points R_{21} and R_{41} must be on the x-axis of \mathcal{F}_1 (1.9)

- y axes of \mathcal{F}_3 and \mathcal{F}_5 must be collinear with the y-axis of \mathcal{F}_1 (1.10)

- Constraint on the roller radii:

$$r_6 = r_7 = r_8 = r_9 \quad (1.11)$$

- Constraints on the centerlines of the slots:

Referring to Figure 1.1, let \vec{c} be the vector $\overline{O_3R_{23}}$ defined via the equation

$$\vec{c} = c_x \vec{u}_1^{(3)} + c_y \vec{u}_2^{(3)} \quad (1.12)$$

where c_x and c_y are the $\vec{u}_1^{(3)}$ and $\vec{u}_2^{(3)}$ components of the vector \vec{c} . From the special dimensions given in equations and statements (1.5) to (1.10), it follows that

$$c_x = \vec{u}_1^{(3)} \cdot \overline{O_3R_{23}} = s_2 \quad (1.13)$$

$$c_y = \vec{u}_2^{(3)} \cdot \overline{O_3R_{23}} = \overline{R_{21}R_{23}} - s_3 \quad (1.14)$$

Then, the constrains on the location of the centers of the other rollers will be [1] as follows.

For roller 7:

$$\vec{u}_1^{(3)} \cdot \overline{O_3R_{43}} = -c_x \quad (1.15)$$

$$\vec{u}_2^{(3)} \cdot \overline{O_3R_{43}} = c_y \quad (1.16)$$

For roller 8:

$$\vec{u}_1^{(5)} \cdot \overline{O_5R_{42}} = -c_x \quad (1.17)$$

$$\vec{u}_2^{(5)} \cdot \overline{O_5R_{42}} = c_y \quad (1.18)$$

For roller 9:

$$\vec{u}_1^{(5)} \cdot \overrightarrow{O_5 R_{22}} = c_x \quad (1.19)$$

$$\vec{u}_2^{(5)} \cdot \overrightarrow{O_5 R_{22}} = c_y \quad (1.20)$$

1.2.2. Kinematic Relations

Position and velocity relations related to links 2 to 5 are given in the following subsections.

1.2.2.1. Position Relations

If the conditions mentioned in the previous subsection are satisfied, then, according to [1] the mechanism is practically one DOF and there exist kinematic constraints on the position of the input links and the slot profile links, such that:

$$s_2 = s_4 \quad (1.21)$$

$$s_3 = s_5 \quad (1.22)$$

1.2.2.2. Velocity Relations

By differentiating equations (1.21) and (1.22) with respect to time, one obtains that the velocities of the input links are equal. The same applies to the velocity of the slot profile links. In other words, one obtains

$$\frac{ds_2}{dt} = \dot{s}_2 = \dot{s}_4 \quad (1.23)$$

$$\frac{ds_3}{dt} = \dot{s}_3 = \dot{s}_5 \quad (1.24)$$

In order to obtain the relation between \dot{s}_2 and \dot{s}_3 , one solves for the derivatives of the loop closure equation. Let the slope of the centerline be denoted as p (see Figure 1.2). From the figure, note that the slope of the line tangent to the locus of the center of the roller is equal to the slope of the tangent line at the contact point since the roller is circular.

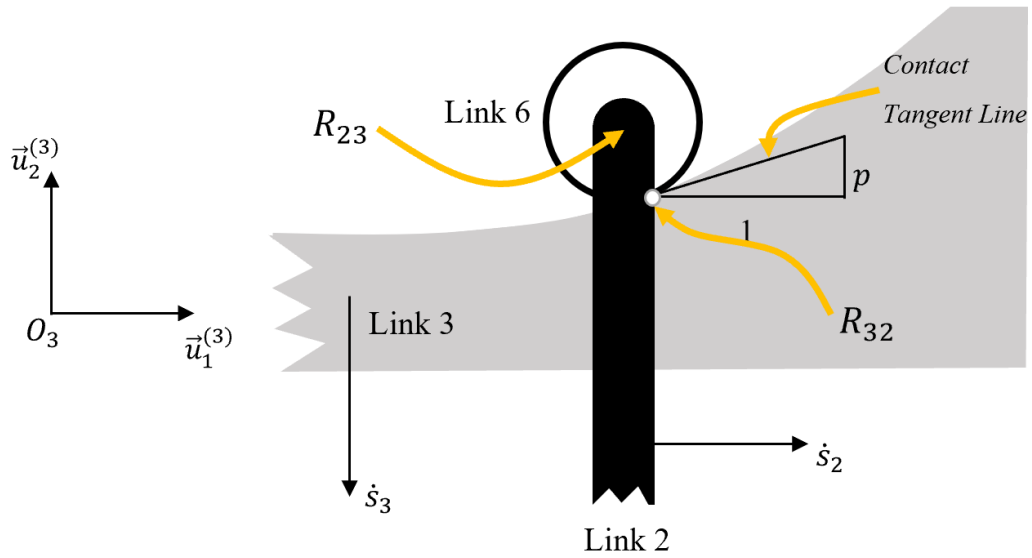


Figure 1.2. Partial view of MFG slot profile roller contact to show the velocity constraint

The slope p may be calculated as shown below.

$$p = \frac{dc_y}{dc_x} = \frac{dc_y/dt}{dc_x/dt} \quad (1.25)$$

By substituting equations (1.13) and (1.14) into (1.25), one obtains the kinematic relationship given below.

$$\dot{s}_3 = -p\dot{s}_2 \quad (1.26)$$

Note that the variable p is equal to infinity when the tangent line in the figure is vertical.

1.2.3. Constraints on the Mass Parameters

The following constraints on the inertial parameters are necessary so that one obtains a dynamically favorable MFG.

- Input links have equal mass

$$m_2 = m_4 \quad (1.27)$$

- Slot profile links have equal mass:

$$m_3 = m_5 \quad (1.28)$$

- Rollers have equal mass and inertia

$$m_6 = m_7 = m_8 = m_9 \quad (1.29)$$

$$I_6 = I_7 = I_8 = I_9 \quad (1.30)$$

- Center of mass positions:

$$\text{Center of mass of the input links are on the x-axis of } \mathcal{F}_1 \quad (1.31)$$

$$\text{Center of mass of the slot profile links are on the y-axis of } \mathcal{F}_1 \quad (1.32)$$

$$\text{Center of mass of the rollers 6 to 9 are on the reference points } R_{23}, R_{43}, R_{42}, \text{ and } R_{22} \text{ respectively.} \quad (1.33)$$

1.2.4. Constraints on the External Forces

The following constraints on the external forces and spring parameters are necessary so that one obtains a dynamically favorable MFG.

- The constraints on the springs:

$$k_3 = k_5 \quad (1.34)$$

$$\text{Endpoints of the springs should be on the y-axis of } \mathcal{F}_1 \quad (1.35)$$

$$\text{The springs should have the same free length} \quad (1.36)$$

- Constraints on the external forces:

$$\vec{F}_2 = -\vec{F}_4 \quad (1.37)$$

In order to connect the MFG to a machine, different methods have been proposed. Direct connection and pulley-cable connection methods have been proposed in [3] and shown in Figure 1.3. In the figure, the MFG springs have not been shown. Direct connection (given in left of the figure) is obtained by rigidly connecting links 2 and 4 to the sliders of twin machines, which perform the same task. In the pulley cable connection method (given in right of the figure), the MFG output links are connected to a single machine by the pulley cable system. In this case, the cables should always be in tension.

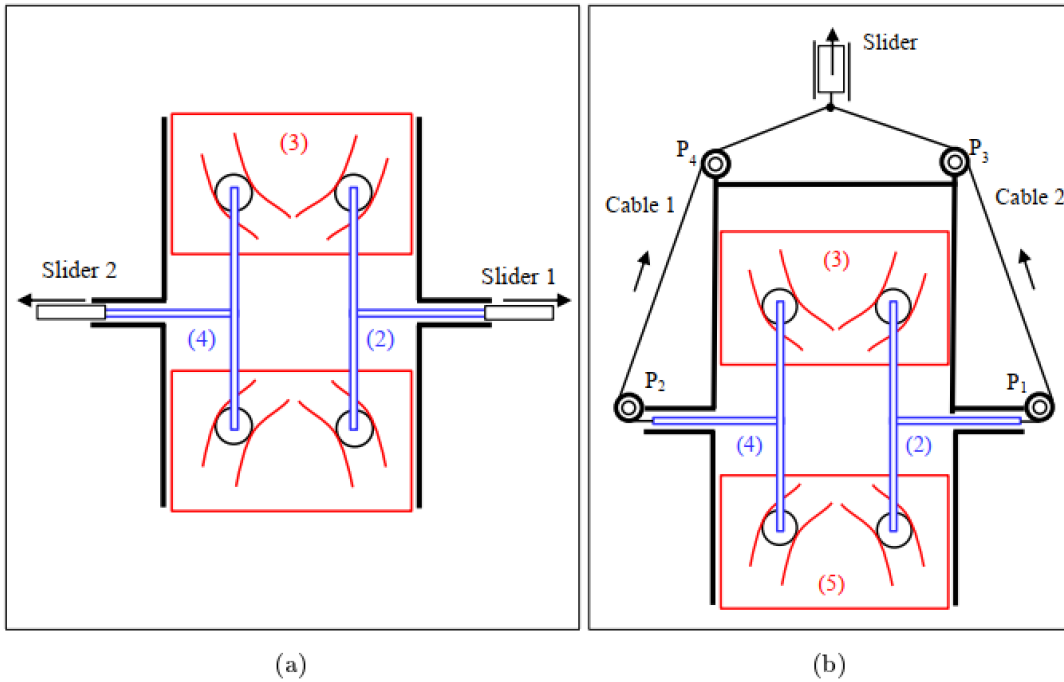


Figure 1.3. MFG connection methods given in [3]

The MFG can also be connected to a single machine by using a rack and pinion mechanism [3]. The application of this method is shown in Figure 1.4. In this method, a pinion P is connected to two racks, which are rigidly connected to the MFG output

links. The MFG's translational outputs can be merged and converted to rotational output, by connecting the pinion (Pinion P in the figure) to the machine. By application of another rack (Rack R in the figure), the MFG outputs can be merged into a rotational output which can be connected to a rotating link of a machine.

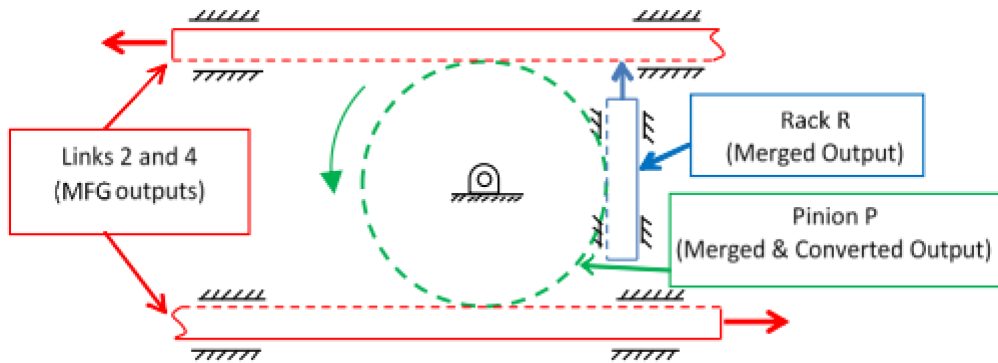


Figure 1.4. MFG connection by using Rack and Pinion mechanism [3]

In this study, in order to satisfy the external force constraint, a symmetrical slider-crank mechanism (see Figure 1.5) is used as a machine. The two sliders of the mechanism are connected to the output links of the MFG.

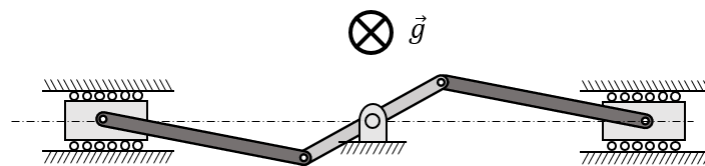


Figure 1.5. Symmetrical Slider Crank Mechanism used as a machine

1.2.5. MFG Power Output Constraints

Due to practical reasons, the motion range of the MFG input links is limited such that

$$s_{2min} \leq s_2 \leq s_{2max} \quad (1.38)$$

Furthermore, it is assumed that the motion of the MFG input links and the external forces are periodic.

As stated in [2], the MFG can provide any conservative force variation with a period T , if the frictional losses are neglected. Provided that,

$$\int_0^T -2F_2 \dot{s}_2 dt = 0 \quad (1.39)$$

where F_2 corresponds to the $\vec{u}_1^{(1)}$ component of the force \vec{F}_2 . The coefficient 2 is due to the addition of the work done by the force \vec{F}_4 . Since the force applied by link 2 on the machine is $(-F_2)$, there is a minus sign in equation (1.39).

If one uses the power output of MFG (P_{mfg}), provided to the machine, as constraint, equation (1.39) can be expressed as in equation (1.41):

$$P_{mfg} = -2F_2 \dot{s}_2 \quad (1.40)$$

$$\int_0^T P_{mfg} dt = 0 \quad (1.41)$$

In this study, equation (1.41) will be referred as the first constraint on the MFG power output.

The second constraint is due to equation (1.40) leading to the fact that, MFG cannot provide any power output when the velocities of its input links are zero.

If one lets t^* to denote the time where $\dot{s}_2(t^*) = 0$, then, the second constraint can be expressed as follows.

$$P_{mfg}(t^*) = 0, \quad \dot{s}_2(t^*) = 0 \quad (1.42)$$

Equation (1.42) is labelled to be the second constraint of the MFG power output throughout the thesis.

For improving performance of machines, these constraints are utilized. If one uses force output as the design variable, then only the constraint in equation (1.39) is enough to describe the limitations on the MFG force output. However, if power output is the design variable, then equations (1.41) and (1.42) must be utilized.

1.3. MFG Design Methods

In this section, the MFG design methods used in the previous studies [3] and [4] and the design method used in this study are briefly described. In all of the methods, the problem is divided into two steps. In the first step, the optimum MFG force (F_2) or power (P_{mfg}) variations, in order to improve a specific aspect of the machine, are determined. In the second step, the aforementioned variations are used to determine the parameters of the MFG (such as link masses, dimensions, spring coefficients, etc.).

1.3.1. Determining Optimum Force Variations

Due to its favorable dynamical properties, MFG's are suggested to be used in performance improvement of mechanisms and actuators driving them [3], for the following purposes.

- In order to reduce the maximum torque/force or power requirement of an actuator for a specific task.
- In order to reduce the power losses of the system.
- In order to reduce the reaction forces between the machine links (in order to reduce friction and elongate machine life).

In [3], for the optimization problems involving the MFG application, deviation from the average power consumption of a machine is utilized, i.e., MFG power is used as the design variable. As the optimal MFG power is calculated, the solution sometimes required non-zero power when the MFG input link velocities are zero. Therefore, the constraint equation (1.42) has not been satisfied. As can be seen from equation (1.40),

asymptotic discontinuities on F_2 will be observed when $\dot{s}_2 = 0$. Such discontinuities have been approximated with spline fitting methods in [3].

A mathematical case study for the suggested method has been performed in [3]. In the case study, two slider cranks have been used as twin machines and they have been connected to the input links of the MFG. The slider-crank mechanisms are driven from their crank link with a constant angular velocity. It is assumed that the actuator only consumes power for the inertial and gravitational forces and moments applied by the slider-crank links. From the results of this mathematical case study, it has been observed that with the optimal power variation, deviation from the average power consumption is reduced to zero. However, with the application of the curve approximation method, the performance is reduced.

Later, in study [4], a numerical minimization algorithm (involving combination of several performance measures) is proposed. The suggested performance measures consist of, but not limited to, minimization of maximum power and minimization of total energy consumption of a DC motor connected to a machine.

In order to obtain the optimum MFG force, $F_2(t)$ is expressed as a Fourier series given by equation (1.43).

$$F_2(t) = a_0 + a_i \cos\left(\frac{2\pi i}{T}t\right) + b_i \sin\left(\frac{2\pi i}{T}t\right) \quad (1.43)$$

$$i \in \mathcal{N}^+, t \in [0, T)$$

Here, the coefficients a_0 , a_i and b_i are the design parameters; and T denotes the period of the task. By assigning arbitrary guesses to the coefficients as initial conditions for the minimization algorithm, optimum MFG force variations have been found. The performance indices have been calculated by using the dynamic analysis of the machine. A gradient-based search algorithm is employed to obtain the optimum coefficients.

The search starts by solving the third order coefficients of Fourier series using 100 arbitrary initial conditions. After the optimal coefficients are found, 100 new arbitrary initial conditions are assigned to determine the coefficients a_4 and b_4 .

In the meantime, the optimization is repeated with, again, 100 arbitrary initial conditions in order to determine 4th order Fourier series coefficients. The coefficients with the best performance amongst the 200 initial conditions are selected to be the optimal coefficients. Higher-order terms are obtained similarly. The method is repeated until the 7th order Fourier series coefficients are obtained. The algorithm given in [4] is summarized in Figure 1.6. In the figure, the notation F_{MFG_i} corresponds to the force variation obtained by the i^{th} order Fourier series approximation.

In this study, MFG power is taken as the design variable and the method proposed in [3] is improved. Three different performance measures are optimized in this study (namely, minimization of maximum power, minimization of maximum torque and minimization of total energy consumption). The asymptotical discontinuity approximation mentioned in [3] is improved. Problems regarding the approximation are discussed and a solution method is proposed. Performances of the methods proposed in this study are assessed using the mathematical case studies presented in [4]; and an improvement in the performance has been observed. The details are given in Chapter 3.

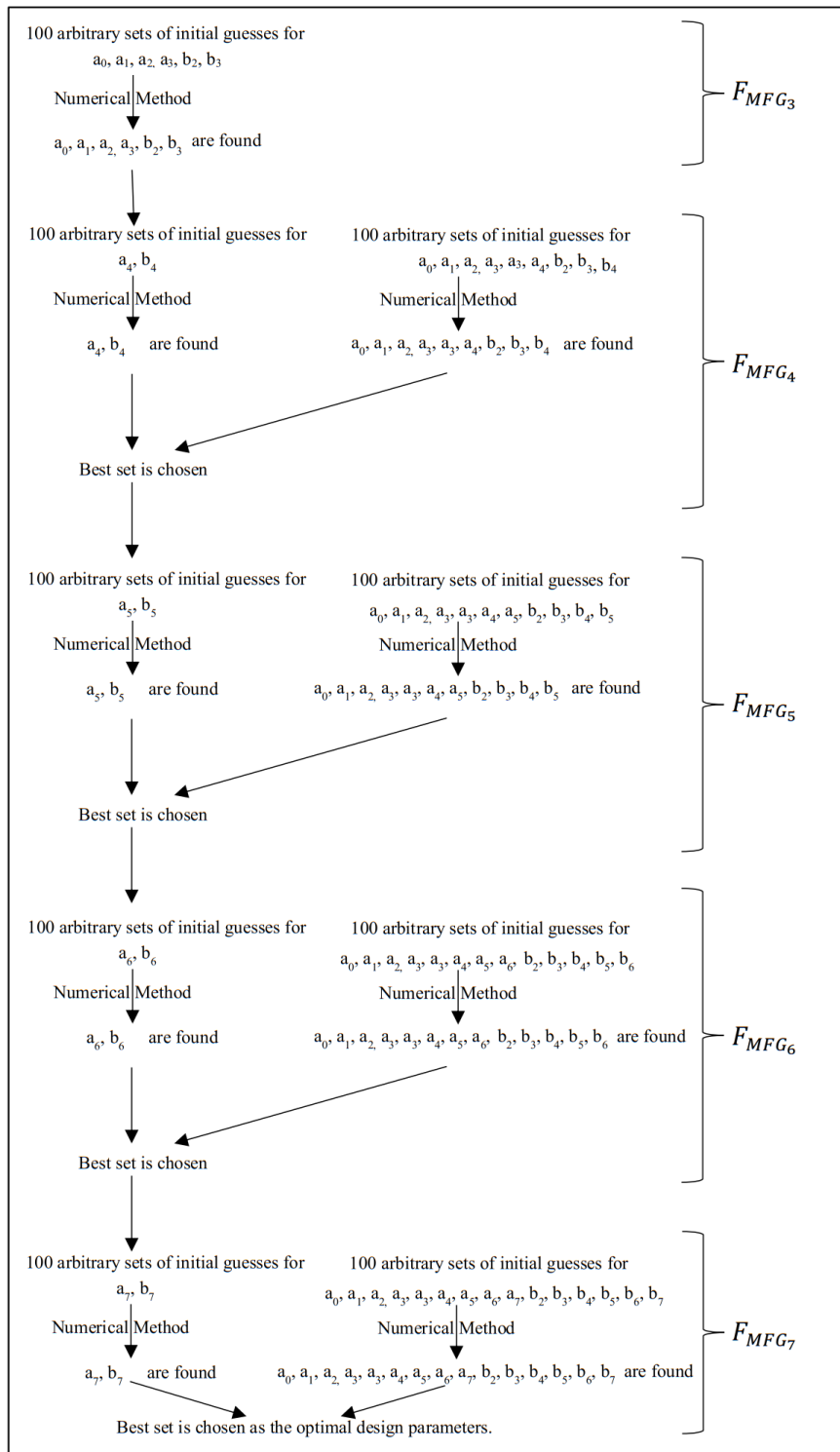


Figure 1.6. Optimum MFG force search method in [4]

1.3.2. Determining Design Parameters of the MFG

In this section, MFG parameter design methods proposed in the previous studies [3], [4] and the design method proposed in this study are briefly described. Recall that in all of the methods, the optimum force or power variation described in the previous section is obtained before determining the design parameters.

In [3], it has been suggested that one may calculate the MFG force if the design parameters and the velocity of link 2 of the MFG are known. The design parameters are the link masses, inertias, link dimensions and parameters for the slot profile centerline. It has been stated that the design parameters can be determined by minimizing the cost function J_{MFG} given by

$$J_{MFG} = \int_t^t (F_{2,des} - F_2)^2 dt \quad (1.44)$$

where $F_{2,des}$, corresponds to the desired force variation and F_2 corresponds to the MFG force variation for the given set of design parameters. In the optimization methods, practical limits on the design variables have been taken into account.

In a later study, in [4], work-energy relations of the external forces applied on the MFG and the mechanical energy change of the MFG have been utilized. In other words, the equation

$$E_{mfg}|_{t_0}^{t_f} = \int_{t_0}^{t_f} -2F_2 \dot{s}_2 dt \quad (1.45)$$

where E_{mfg} denotes the mechanical energy of the MFG, has been employed. Using this relation, an iterative method in order to calculate design variables has been proposed. In this method, by assigning initial guesses to the design parameters position and velocity of link 3 are determined iteratively. The iteration stops when the difference of the successive iterations' position of link 3 is below a specified value.

In this study, the work-energy relation derived in [4] is improved. Using the work-energy relation, equation of motion of the MFG spring elongation from the free length is derived. Conditions to obtain solution to the equation are determined. The work-energy equation is improved by taking into account the extension springs with initial tension. It has been found that the MFG design is applicable to either extension or compression springs. The details are given in Chapter 2.

One of most the challenging part of the MFG design is to obtain a physically feasible slot profile shape. In this study, MFG designs with different types of slot profiles and slot types are investigated. Performances of different types are compared by performing experiments (see Chapter 6).

1.3.2.1. Open and Closed Type Slot Profiles

In this study, a slot profile is called an open slot profile if s_3 is a single-valued function of s_2 . In other words, a slot profile is open slot profile if the centerline vector components c_y is a single valued function of c_x . If a slot profile is not open, then it is called a closed slot profile. Four examples of open and closed slot profiles are shown in Figure 1.7.

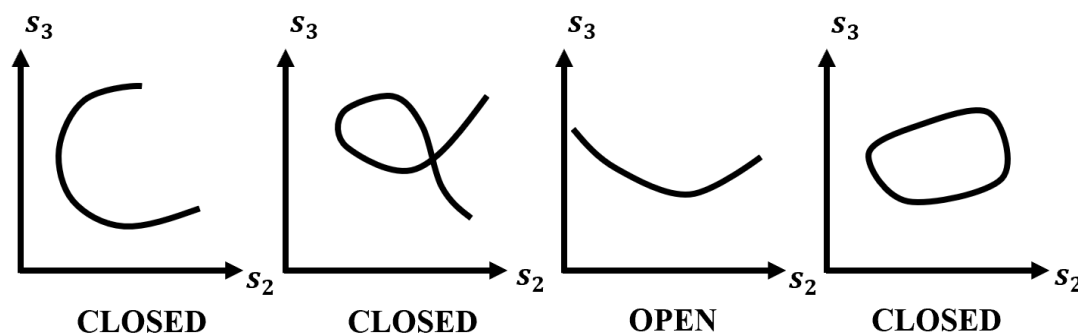


Figure 1.7. Open and closed type slot profiles according to the definition

In [3], polynomial coefficients are used to parameterize the slot shape centerline. Therefore, the slot shapes obtained in [3] are open slot profiles.

In the study where the slot profiles are obtained by the iterative method [4], all of the slot profiles obtained are of the closed type. One slot profile taken from [4], is shown

in Figure 1.8. The x and y axes in the figure correspond to the axes of \mathcal{F}_3 . The roller starts from the position denoted with dot numbered as 1 in the figure and follows the arrows. To realize this kind of a slot profile, three trigger mechanisms (shown in the figure with their numbers) are required to ensure that the roller follows the slot properly [4].

In this study, a new method, to obtain an MFG with open slot profile is proposed. However, this method is applicable for special motions of MFG input links, s_2 and \dot{s}_2 . The method is given in Section 3.4.

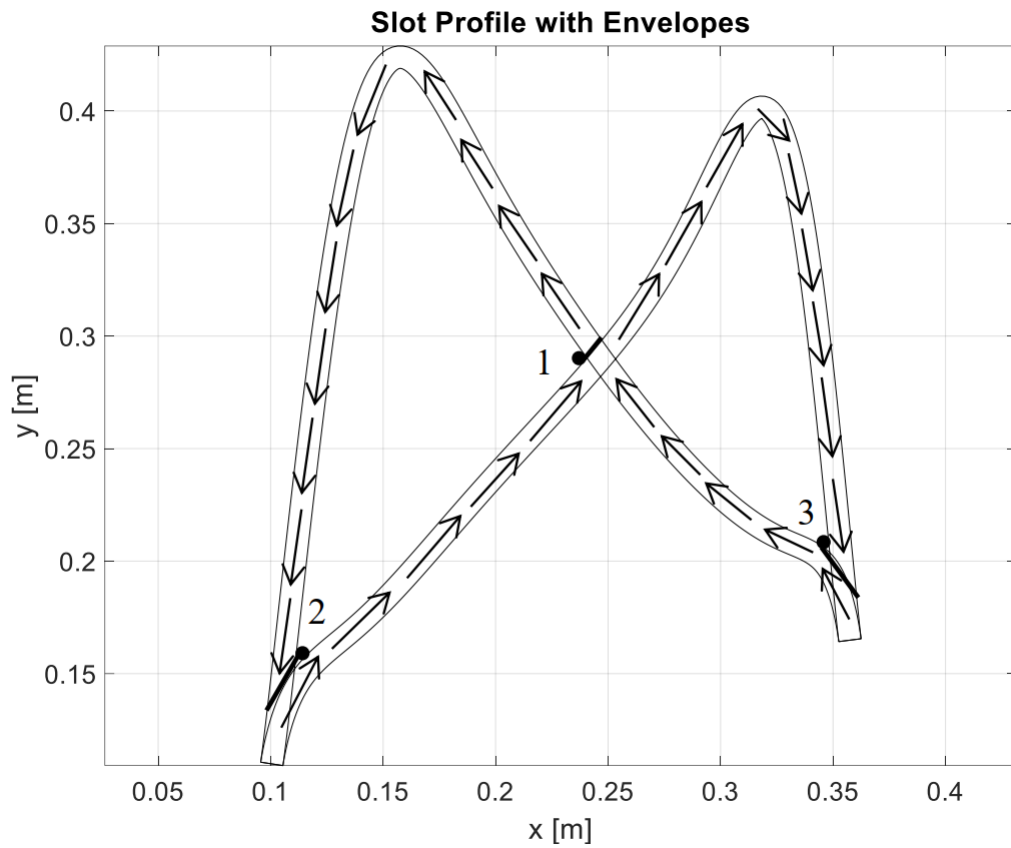


Figure 1.8. A Closed type slot profile [4]

1.3.2.2. One-Sided Slots

If a roller contacts one side of the slot profile throughout the motion, then the other side of the slot profile is unnecessary. Hence, it can be removed to reduce the mass and size of the slot profile links. This further simplifies the implementation of MFGs. Slot profiles with one-sided and two-sided slots are shown in Figure 1.9.

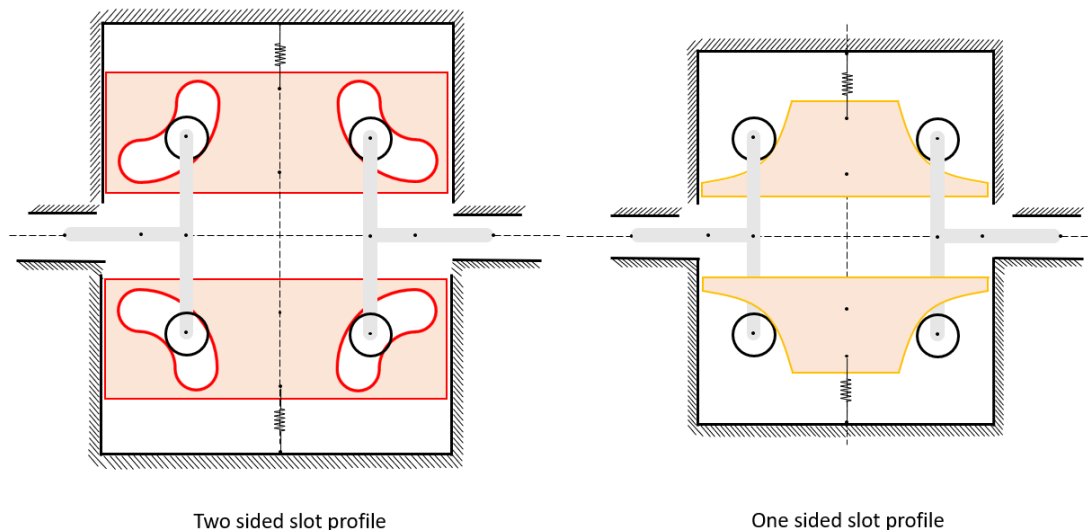


Figure 1.9. Slot profiles with one-sided and two-sided slots

If large tolerances are used in manufacturing and assembly, in the one-sided slot profile case, one or more rollers may lose contact with their corresponding slot profile links. However, motion can still be maintained (with reduced MFG performance). On the other hand, if the two-sided slot profiles are used, roller would be stuck on the other side of the slot and would complicate the motion (Noting that the MFG is overconstrained, the motion in two-sided slot depends on the flexibility of the links and clearances on the joints considering large manufacturing and assembly tolerances).

1.3.2.3. Alternative MFG Configurations Depending on Joint Type between Slot Profile and Ground Links

In the MFG, considering the type of joints connecting links 3 and 5 to the ground, there are 3 different alternatives. These alternatives are listed below.

- **Overconstrained MFG:** The joint between link 3 and the ground is a prismatic joint; and the joint between link 5 and the ground is also a prismatic joint [designated as (MFG)P in this study].
- **Regular MFG:** The joint between link 3 and the ground is a prismatic joint; and the joint between link 5 and the ground is a cylinder in slot joint [designated as (MFG)PC in this study]. Note that, the alternative where the joint between link 3 and the ground is a cylinder in slot joint; and the joint between link 5 and the ground is a prismatic joint is identical with the alternative defined in the previous sentence.
- **Relaxed MFG:** The joint between link 3 and the ground is a cylinder in slot joint; and the joint between link 5 and the ground is also a cylinder in slot joint [designated as (MFG)C in this study].

When there is no slippage between rollers 6, 7, 8, 9 and links 3 & 5, the “actual” degree of freedom of (MFG)P, (MFG)PC and (MFG)C will be 1, 1 and 2, respectively. Note that (MFG)P is an overconstrained mechanism, whereas (MFG)PC and (MFG)C are not. Note also that,

- if the MFG is precisely manufactured and assembled (i.e., if the special kinematic dimensions of the “assembled” MFG are equal to their designed values) [see equations (1.5) to (1.20)],
- if the inertial parameters of the “assembled” MFG are equal to their designed values [see equations (1.27) to (1.33)],
- if the loading on the MFG is balanced [see equations (1.34) to (1.37)]

then, (MFG)P, (MFG)PC and (MFG)C would be kinematically equivalent [i.e., for any given input motion, the motions of (MFG)P, (MFG)PC and (MFG)C would be identical]. Furthermore, disregarding the effect of gravitational acceleration, all reaction forces and moments associated with all of the 4 joints connecting the MFG to the ground will be zero all times. In order for the kinematical equivalency to be valid, one should note that one of the degrees of freedom of (MFG)C becomes inactive; so that, in practice, it behaves as a one degree of freedom mechanism (rather than a two degree of freedom mechanism). If, on the other hand, the aforementioned 3 conditions are only “approximately” satisfied, then (MFG)P, (MFG)PC and (MFG)C would only be “approximately” kinematically equivalent; and the reaction forces and moments associated with the 4 joints connecting the MFG to the ground will be “approximately” zero. Furthermore, one expects the frictional losses associated with the MFG to be maximum in the case of (MFG)P and minimum in the case of (MFG)C. The frictional losses associated with (MFG)PC, on the other hand, is expected to lie somewhere between the maximum and minimum values. Finally, if the first condition of the aforementioned 3 conditions is only “approximately” satisfied, one expects to have deformations in the links (as much as the elasticity of the links would allow). These deformations are expected to be the most in the case of (MFG)P; and the least in the case of (MFG)C. The deformations in the case of (MFG)PC, on the other hand, are expected to be somewhere between the deformations corresponding to (MFG)P and (MFG)C. Therefore, the problems related with large manufacturing and assembly tolerances can be further compensated by using (MFG)C configuration.

Furthermore, since the DOF of the (MFG)C is 2, the kinematic constraints, given by equations (1.21) and (1.23) that must be satisfied by the machines that are connected to the MFG, are also relaxed. Therefore, performance of the (MFG)C is then, less affected by control errors associated with driving machines that are connected to the MFG synchronously.

1.4. MFG Experimental Analyses

In order to demonstrate the performance improvement of machines by using MFGs, an experimental setup has been built previously [3]. In the experiment, two identical slider cranks have been used as twin machines. An MFG has been designed to minimize the deviation from the average motor power. The experiment could not be conducted successfully due to several reasons mentioned in [3].

In this study, solutions for the problems faced previously conducted experiment [3] are sought. Most of the hardware in the previously conducted experiment has been changed and the experiment is repeated with different case studies.

Before conducting the experiments, a mathematical case study (where an MFG is designed to improve the performance of a motor) is performed. The motor in the case study drives an external load on a symmetrical slider-crank (i.e., the symmetrical slider-crank shown in Figure 1.5 is used as a machine). In order to simulate the external load, a spring is attached between the two sliders of the machine. This mathematical case study is discussed in Chapter 4.

After the MFG design, an experimental setup, to validate the results of the mathematical study, has been built. The mechanical design of the machine and the MFG are presented. The electronic and electromechanical components used in the experiment are described. Finally, the software utilized to perform the experiments is explained. The details about the experimental setup are given in Chapter 5. The results of the experiments are given and discussed in Chapter 6.

1.5. Contributions of the Thesis

The contributions of this thesis are listed below:

- New optimization algorithms are proposed to obtain optimum power variations of the MFG (P_{mfg}). The performances of the proposed methods have been compared with a case study discussed in [4], and it has been shown that better results are obtained.

- A new method, which modifies the optimum power variations (P_{mfg}) that produce closed slot profiles, so that one obtains MFGs with open slot profiles, is proposed. The limitations of the algorithm are also discussed.
- MFG design methods are improved in following ways.
 - The minimum values for some design parameters have been determined.
 - It has been proven that either compression or tension springs can be used to obtain the same power variation (P_{mfg}).
 - The suggested algorithm also works with extension springs with an initial tension.
 - Some of the design parameters are uncoupled from each other in order to simplify the parameter design (e.g., link dimensions are not required to find the spring elongation variation with respect to time).
- An experimental setup has been built which can be used with other MFGs (in addition to the MFG designed in this study) with different loadings, machine link masses and machine motion profiles. Some properties of the experimental setup are listed below.
 - The sliders of the machine have adjustable masses
 - Different springs can be loaded between the machine slider links.
 - MFG has an option to convert the prismatic joint between link 3 and the ground link to a cylinder in slot joint. The same option can be applied to link 5.
 - The controller built for the experimental setup can drive the mechanism for different motor shaft motions.
- The experiments in the study are conducted successfully. MFG designs with open-slot profiles and one-sided slots has been considered.
- Performance of MFGs with one-sided slots profile links having prismatic joints and the ones having cylinder in slot joints to the ground, are compared with each other experimentally.

1.6. Organization of the Thesis

In Chapter 2, the MFG parameter design is investigated in detail. The work-energy equation is improved with respect to the one in [4]. Extension springs with initial tension are discussed. A step by step parameter design algorithm is given. Roller centerline curve calculation, contact point calculation methods are also discussed. Simplified force analysis equations are derived.

In Chapter 3, determination of optimum power variations to improve specific performance measures are discussed. Three methods, for minimization of maximum motor mechanical power output, minimization of motor output torque and minimization of motor copper losses, are derived. Compensation methods to convert the obtained power variations to modified power variations that would satisfy constraint equations (1.41) and (1.42) are proposed. A method which predicts whether a given power variation results in an MFG with open slot profile is introduced. In case the power variation does not result in an open slot profile, a method to convert the power variation such that one obtains an open slot profile is explained. The abovementioned methods are demonstrated with a case study introduced in [4].

Chapter 4 is reserved to a mathematical case study. Firstly, the machine and external loads to be used in the experiment are modeled. Then, the optimum power variations are calculated. Finally, the MFG parameters are designed.

In Chapter 5, the problems faced in the previous experiments [3] have been investigated. Then the challenges for the experimental setup construction are discussed. The mechanical construction of the machine and the MFG are described. Methods to decrease friction on the MFG joints are explained. Configurable options for the MFG and the machine are also discussed. The electronic and electromechanical hardware used in the experiments are given. Finally, the software algorithms used for the experiment are explained in detail. The software algorithms consist of motor control, position and velocity estimation, current reading, and a main algorithm to manage the mentioned algorithms.

In Chapter 6 experimental results are presented. Firstly, the experimental cases are described. Then the control performances, power, energy consumption, and MFG performances are calculated and discussed.

CHAPTER 2

DESIGN OF MECHANICAL FORCE GENERATORS

2.1. Introduction

In this chapter, the physical construction of MFG is discussed. Work done by the MFG and motion profile of its links are used as input. These inputs should satisfy MFG power constraints discussed in Section 1.2.5.

For slot profile generation, calculations developed in the previous study [4], are generalized. This helps to distinguish the effects of the design variables, such as the spring stiffness, the link masses, inertias, and their sizes. It is shown that MFG can be designed with either compression or tension springs. The design by using extension springs having initial tension is studied. It is found that the existence of solution for a given MFG power variation input is dependent upon the spring energy when link 2 has zero velocity.

In order to have continuous contact between the slot profile and the roller, the normal force on the profile and the radius of curvature of the profile are investigated.

2.2. Additional Parameters Used in the Design of MFG

For the design of MFG, some additional parameters are also defined using the various reference points on the MFG (see Section 1.1).

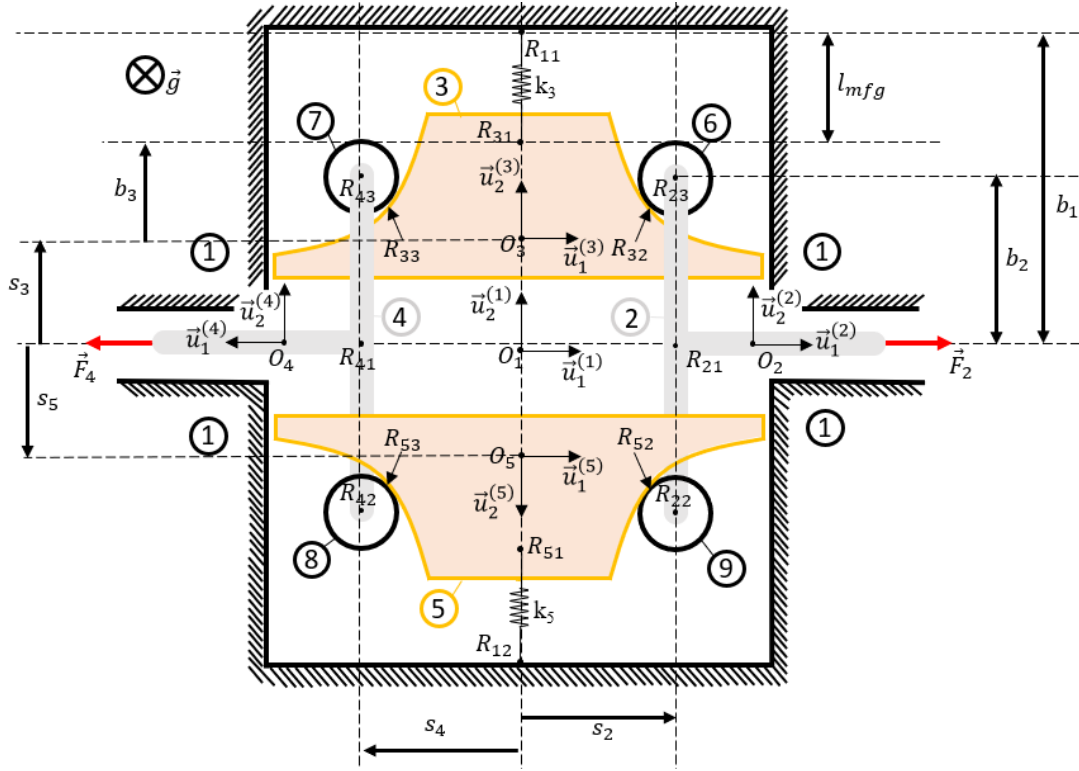


Figure 2.1. Design parameters used in MFG

The design parameters used in the MFG are shown in Figure 2.1. The length and stiffness of the springs are given by

$$l_{mfg} = \overline{R_{31}R_{11}} = \overline{R_{51}R_{12}} \quad (2.1)$$

The dimensions b_1, b_2, b_3 , on the other hand, are defined via the following equations.

$$b_1 = \overline{O_1R_{11}} = \overline{O_1R_{12}}$$

$$b_2 = \overline{R_{21}R_{23}} = \overline{R_{21}R_{22}} = \overline{R_{41}R_{43}} = \overline{R_{41}R_{42}} \quad (2.2)$$

$$b_3 = \overline{O_3R_{31}} \cdot \vec{u}_2^{(3)} = \overline{O_5R_{51}} \cdot \vec{u}_2^{(5)}$$

2.3. Work-Energy Equations for MFG

Following the approach used in [4], the mechanical energy change of the MFG from the initial time (t_0) to the current time (t), neglecting the frictional losses of the MFG, can be written as follows:

$$-W_{mfg}(t) = - \int_{t_0}^t P_{mfg} dt = E_{mfg} \Big|_{t_0}^t = E_{mfg}(t) - E_{mfg}(t_0) \quad (2.3)$$

where E_{mfg} corresponds to the mechanical energy of the MFG. Note that, when $P_{mfg} > 0$, the MFG works as a power source and its mechanical energy decreases. Note also that the work done by the MFG (W_{mfg}) is known and it is an input to the MFG design. The mechanical energy of the MFG, on the other hand, is given by the following equation.

$$\begin{aligned} E_{mfg}(t) &= \frac{1}{2} \sum_{i=2}^5 m_i \dot{s}_i(t)^2 + \frac{1}{2} \sum_{i=6}^9 m_i \dot{s}_2(t)^2 + \frac{1}{2} \sum_{i=6}^9 I_i \dot{\psi}_i(t)^2 \\ &+ 2E_{spring}(t) \end{aligned} \quad (2.4)$$

In equation (2.4), ψ_i denotes the angular speed of the i^{th} roller. Note that the gravity vector is taken into the page as shown in Figure 2.1. Therefore, gravitational potential energy is constant throughout the motion.

Energy of each spring (E_{spring}), which are connected from link 3 and link 5 to the ground link, can be calculated via equation (2.5)

$$E_{spring}(t) = \frac{1}{2} k_3 d(t)^2 \quad (2.5)$$

where it has been noted that $k_5 = k_3$. In equation (2.5), $d(t)$ is the elongation of the spring which is the length of the spring (l_{mfg}) minus its free length ($l_{free,mfg}$). The elongation $d(t)$ can be expressed in terms of the link dimensions, the free length of the spring, and the position of link 3 (s_3) as given in equation (2.6).

$$d(t) = b_1 - b_3 - l_{free,mfg} - s_3(t) \quad (2.6)$$

The spring energy equation (2.5) is valid for compression springs and extension springs without any initial tension, where the initial tension is defined as the minimum force required to extend the spring from its free length. Therefore, in subsection 2.3.1, new expression for the spring energy is derived by using the initial tension force.

2.3.1. Extension Springs with Initial Tension

Extension springs that have coils in contact with each other are called closed wound springs. Spring manufacturers prefer this type of spring in order to adjust (during the production) the free length of the spring more accurately [5]. This type of spring has an initial tension. The initial tension of the springs that are connected to links 3 and 5 are denoted as F_{s30} in this study.

The force vs elongation plot of an extension spring with initial tension is given in Figure 2.2. It is evident that once the elongation parameter (d) is used in the energy calculations, it takes the following form:

$$E_{spring}(t) = \frac{1}{2} k_3 (d(t) + d_0)^2 - \frac{1}{2} k_3 d_0^2 \quad (2.7)$$

$$d \geq 0$$

where d_0 is defined as the virtual elongation at the free length, since the spring length (l_{mfg}) can never be shorter than its free length ($l_{free,mfg}$). Measurement of the spring length definitions are shown in Figure 2.3.

d_0 may be calculated via the following equation.

$$d_0 = \frac{F_{s30}}{k_3} \quad (2.8)$$

For simplicity in notation, a new variable labelled as virtual elongation (y), is introduced via the equation

$$\begin{aligned}y(t) &= d(t) + d_0 \\ y(t) &\geq d_0\end{aligned}\tag{2.9}$$

The inequality constraint in equation (2.9) exists since the spring length cannot be shorter than its free length for extension springs. The spring energy may be defined by using the new variable (y) as:

$$E_{spring} = \frac{1}{2}k_3y(t)^2 - \frac{1}{2}k_3d_0^2\tag{2.10}$$

Note that, for extension springs without initial tension or for compression springs, $d_0 = 0$. Therefore, equation (2.10) is valid for these types of springs as well.

This notation is useful when the energy change from the initial state ($E_{spring}(t) - E_{spring}(0)$) is calculated, where the second terms in equation (2.10) cancel each other and the result is a constant multiplied by the square of the virtual elongation (y). Using the variable y simplifies the expression for the work-energy equation to be discussed in Section 2.3.3.

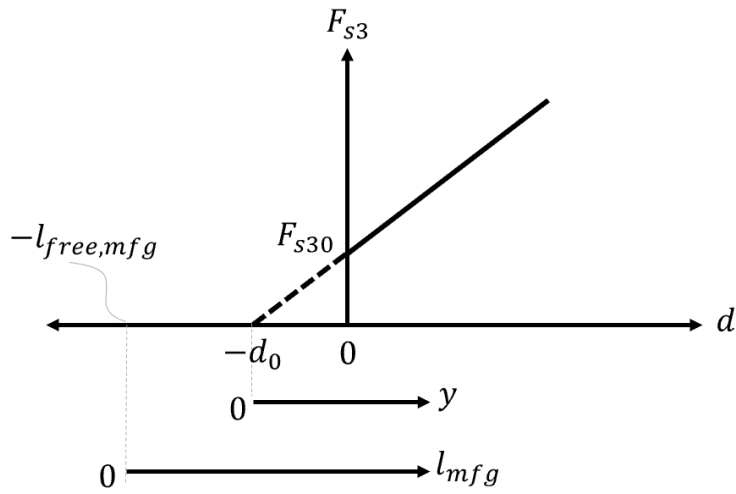


Figure 2.2. Elongation (d), virtual elongation (y) and spring length (l_{mfg}) vs spring force (F_{s3}) graphs for the extension springs with initial tension

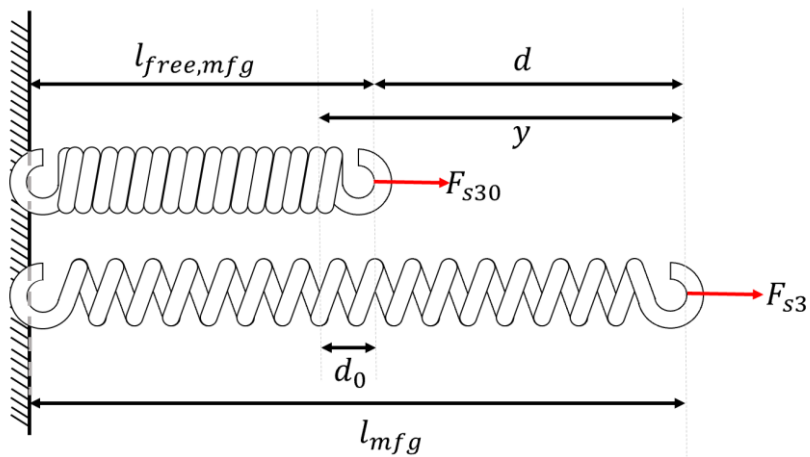


Figure 2.3. Elongation (d), virtual elongation (y), spring length (l_{mfg}) and virtual elongation at free length (d_0)

Once the virtual spring elongation is determined, it can be converted to the spring length by following equation:

$$l_{mfg} = y - d_0 + l_{free,mfg} \quad (2.11)$$

2.3.2. Representation of Roller Angular Speed

Angular speeds of the rollers can be expressed in terms of \dot{s}_2 and \dot{s}_3 . The magnitude of the velocity of the roller center, v_t , is shown in Figure 2.4 with respect to link 3 reference frame. The roller contacting link 3 is shown for demonstration. The results to be found are applicable to all of the rollers. Recall that the sign of the rotational speed does not affect the rotational kinetic energy. Therefore, $\dot{\psi}$ is used for the magnitude of the rotational speed of rollers for the kinetic energy calculation.

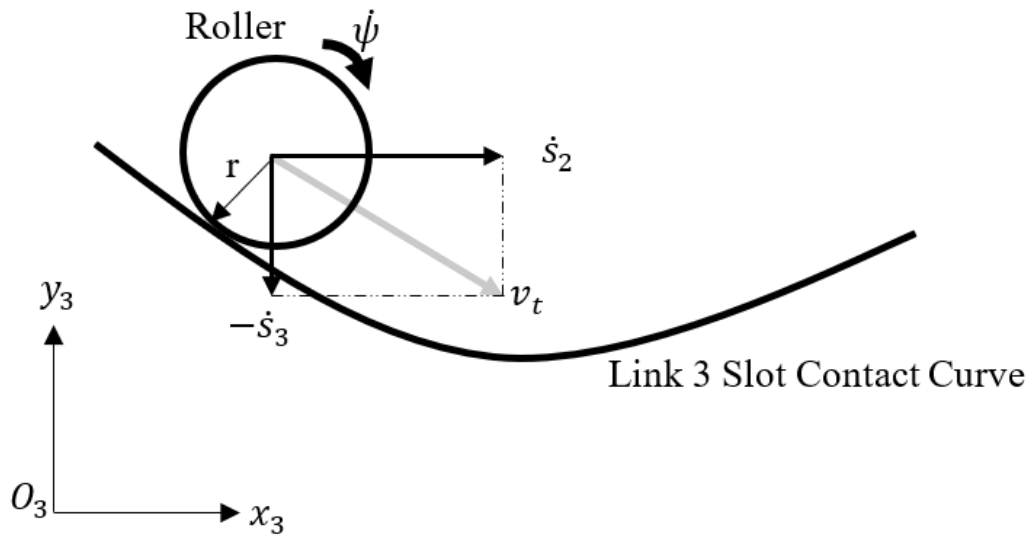


Figure 2.4. Roller centerline relative velocity

The magnitude of the roller center velocity (v_t) relative to link 3 can be expressed as:

$$v_t = \sqrt{\dot{s}_2^2 + \dot{s}_3^2} \quad (2.12)$$

Assuming that there is no slippage between the roller and the contact surface, the magnitude of the angular velocity of the roller ($\dot{\psi}$) is:

$$\dot{\psi} = \frac{1}{r} v_t = \frac{1}{r} \sqrt{\dot{s}_2^2 + \dot{s}_3^2} \quad (2.13)$$

Then, the kinetic energy of each roller can be expressed as:

$$\begin{aligned}
E_{k,roller} = E_{k,6} &= \frac{1}{2}m_6\dot{s}_2^2 + \frac{1}{2}I_6\dot{\psi}^2 \\
&= \frac{1}{2}\left(\frac{I_6}{r^2}\right)(\dot{s}_2^2 + \dot{s}_3^2) + \frac{1}{2}m_6\dot{s}_2^2
\end{aligned} \tag{2.14}$$

Recall that the inertia and the mass of each roller are the same (see Section 1.1). In other words, $m_9 = m_8 = m_7 = m_6$ and $I_9 = I_8 = I_7 = I_6$.

2.3.3. Design Equations Based on Virtual Spring Elongation

In this section, previously defined [4] energy equations are converted into a generic form by representing the MFG work energy equations in terms of virtual spring elongation defined in Section 2.3.1. The generic form simplifies the calculations of MFG design and makes them more comprehensible, such that the effects of design variables are clearer from the equation.

When one uses the symmetry constraints given in Section 1.2, the mechanical energy of the MFG given by equation (2.4) reduces to:

$$E_{mfg}(t) = m_2\dot{s}_2^2 + m_3\dot{s}_3^2 + 4E_{k,roller} + 2E_{spring} \tag{2.15}$$

Substitute equations (2.10) and (2.14) to (2.15) (for the spring energy and the kinetic energy of the rollers), one obtains

$$\begin{aligned}
E_{mfg}(t) &= (m_2 + 2m_6 + 2I_6/r^2)\dot{s}_2^2 + (m_3 + 2I_6/r^2)\dot{s}_3^2 \\
&\quad + k_3y^2 - k_3d_0^2
\end{aligned} \tag{2.16}$$

Link 3 velocity (\dot{s}_3) can be represented by taking the time derivative of the virtual elongation given by

$$y(t) = b_1 - b_3 - l_{free,mfg} + d_0 - s_3(t) \tag{2.17}$$

$$\dot{y}(t) = -\dot{s}_3(t) \tag{2.18}$$

The total mechanical energy of MFG can then be expressed in terms of the virtual elongation (y) and its derivative (\dot{y}) by substituting equation (2.18) into (2.16). Hence, one obtains

$$\begin{aligned} E_{mfg} \\ = (m_2 + 2m_6 + 2I_6/r^2)\dot{s}_2^2 + (m_3 + 2I_6/r^2)\dot{y}^2 + k_3y^2 + k_3d_0^2 \end{aligned} \quad (2.19)$$

By substituting equation (2.19) into the work-energy equation (2.3), and then collecting the y and \dot{y} terms in the left hand side of the equation, one obtains the work-energy equation in terms of $y(t)$ and $\dot{y}(t)$.

$$\begin{aligned} k_3y^2 + \left(m_3 + \frac{2I}{r^2}\right)\dot{y}^2 \\ = E_{mfg0} - W_{mfg} - \left(m_2 + \frac{2I}{r^2} + 2m_6\right)\dot{s}_2^2 + k_3d_0^2 \end{aligned} \quad (2.20)$$

where E_{mfg0} , is the initial mechanical energy of the MFG at t_0 given by:

$$E_{mfg0} = E_{mfg}(t_0) \quad (2.21)$$

Note that when E_{mfg0} is expanded the $k_3d_0^2$ terms cancel each other in equation (2.20). This form is the generic equation of motion for the spring virtual elongation (y) which may be written in the form

$$Ay^2 + B\dot{y}^2 = C(t) \quad (2.22)$$

where A and B are constants and C is time-varying. Definition of A, B and C(t) are given below.

$$\begin{aligned} A &= k_3 \\ B &= m_3 + \frac{2I}{r^2} \\ C(t) &= E_{mfg0} - W_{mfg} - \underbrace{\left(m_2 + \frac{2I}{r^2} + 2m_6\right)}_{B'}\dot{s}_2^2 + k_3d_0^2 \\ B' &= m_2 + \frac{2I}{r^2} + 2m_6 \end{aligned} \quad (2.23)$$

Note that $C(t)$ is time varying because W_{mfg} and \dot{s}_2 are functions of time.

At the initial time t_0 (where $\dot{s}_2(t_0) = 0$), C term in equation (2.23) simplifies to the following:

$$C = k_3 y_0^2 - W_{mfg} - B' \dot{s}_2^2 \quad (2.24)$$

For a t_0 , such that $\dot{s}_2(t_0) = 0$

where $y_0 = y(t_0)$ is defined as preloaded virtual elongation.

Note that due to the kinematic relation between the velocities \dot{s}_2 & \dot{s}_3 , if link 2 velocity is zero so is link 3 velocity, provided that the slope of the tangent of the roller slot profile contact (p) given in equation (1.26) is not infinity.

One can see that the spring elongation y can be either positive or negative, both would satisfy equation (2.22). Therefore, it is possible to design the same MFG with compression or extension springs, but not both on same application. This would not be easy to see if the spring length (l_{mfg}) or the spring elongation (d) was used as the unknown variable in the work-energy equation.

Note that the virtual elongation (y) must be greater than d_0 as given in equation (2.9). Therefore, the left-hand side of equation (2.22) must satisfy the following inequality constraint:

$$Ay^2 + B\dot{y}^2 \geq Ad_0^2 \quad (2.25)$$

The left-hand side of equation (2.22) must satisfy the inequality in equation (2.25) to have a solution. Design parameters to satisfy this inequality are the spring virtual spring elongation when link 2 velocity is zero (y_0), k_3 and B' as can be seen from equation (2.24). Minimum virtual preload equation can be found by combining the inequality constraint in equations (2.25) to (2.24) to yield:

$$k_3 y_0^2 \geq Ad_0^2 + 0 \leq t \leq T (W_{mfg} + B' \dot{s}_2^2) \quad (2.26)$$

It can be seen that as the inertia and mass values inside B' increase, the required virtual spring elongation also increases. It can be concluded that in order to reduce the required preload on the MFG springs, masses of links 2 & 4 and the rollers, and the inertias of the rollers should be as low as possible.

Re-organizing equation (2.26) one obtains

$$y_0 \geq \sqrt{\frac{Ad_0^2 + \max_{0 \leq t \leq T}(W_{mfg} + B'\dot{s}_2^2)}{k_3}} \quad (2.27)$$

Using (2.11), the minimum preloaded spring length ($l_{mfg0,min}$) to have a solution for (2.22) is calculated as given below.

$$l_{mfg0,min} = \sqrt{\frac{k_3 d_0^2 + \max_{0 \leq t \leq T}(W_{mfg} + B'\dot{s}_2^2)}{k_3}} - d_0 + l_{free,mfg} \quad (2.28)$$

It should be expected that if the minimum preload length is selected in the MFG design, the spring length will reduce to its free length at sometime within the period.

It has been shown that the existence of a solution for the design of an MFG (for a given W_{mfg}), can be ensured by adjusting the spring preload length. The link dimensions and the mass parameters can be used to determine the slot shape and size.

2.4. Parameter Design Suggestions

In this study, it is suggested to design the mass and inertia parameters as low as possible depending on the application, and the available space for the MFG. As discussed in the previous section, in equation (2.26), as the mass and inertia of links 2 and 6 increase, the required minimum spring preload length increases. From equations (2.26) and (2.22), it is observed that the initial energy on the spring is transferred to the load and the kinetic energy of the MFG links. If the mass and inertia parameters could be made zero, the equations would become much simpler, and all of the spring energy would be transferred to the load.

The steps of the suggested method are listed below:

1. Design mass, inertia, dimension parameters ($m_2, m_6, I_6, b_1, b_2, b_3, l_{free,mfg}$) and the spring coefficient (k_3) considering the collision possibility between the links of the MFG. Try to set the mass and inertia parameters as low as possible. Collision between links cannot be checked before the shapes of links 3 and 5 and the motion are designed. Therefore, for the initial design of $m_2, m_6, I_6, b_1, b_2,$ and b_3 , the maximum displacement of link 3 may be considered to reduce the possibility of collision. Let the displacement of link 3 be denoted as (Δs_3) given by

$$\Delta s_3 = \max(s_3) - \min(s_3) \quad (2.29)$$

The displacement can be considered as a maximum when the minimum spring preload length is used (provided that the other parameters are fixed). Subtracting the free length from the minimum spring preload length in equation (2.28), one may estimate the maximum displacement to be used in the determination of the dimensions.

$$\Delta s_{3max} \approx \sqrt{\frac{k_3 d_0^2 + \max_{0 \leq t \leq T} (W_{mfg} + B' \dot{s}_2^2)}{k_3}} - d_0 \quad (2.30)$$

Recall that B' is defined in (2.23), d_0 is defined in Section 2.3.1. Equation (2.30) is an approximate value since the masses of links 3 and 5 are not taken into account.

From equation (2.30), it can be observed that by increasing the spring coefficient, one can reduce the size of link 3 displacement.

2. Once the mentioned parameters ($m_2, m_6, I_6, b_1, b_2, b_3, l_{free,mfg},$ and k_3) are designed, determine the variation of spring length with respect to time by the method given in the upcoming Section 2.5,. In the method, use the designed parameters and make a guess for the mass of link 3 and the initial spring preload length.

3. Determine the locus of the center of the rollers and thus the slot walls, by using the method given in Section 2.6.
4. Design the shape of link 3 using the obtained locus in the step 2. Once the shape is designed, the mass of the link can be determined.
5. If collision occurs and/or the calculated mass or size of the slot profile is larger than desired, then repeat step 3 with different initial spring preload lengths. If there is still collision or the parameters (mass or size of the slot profile link) are still larger than desired, then return to step 1 and re-design all of the parameters.

2.5. Iterative Solution Method for Spring Length Profile Calculation

In the previous MFG design study, Erdinç [4] proposed an iterative method to solve the spring lengths and other design parameters in an iterative approach. In the method, using the initial guesses for the design variables (namely, k_3 , m_2 , m_3 , m_6 , I_6 , $l_{free,mfg}$, r_6), the spring length profile with respect to time ($l_{mfg}(t)$) is firstly calculated ignoring the kinetic energies of links 3 & 5 (by using the work-energy equation in (2.3)). Then, the velocities of links 3-9 are calculated by taking the derivative of the spring length to calculate the kinetic energy of the links. Using this kinetic energy in the work-energy equation, the spring length of the next iteration is calculated. Calculation iterations of the spring length and the kinetic energy calculation continues until the root mean square difference of the spring length for two consecutive iterations converges to a value below a specified threshold. If the iterations do not converge, or if a solution does not exist, then the design variables are updated.

The method proposed in [4] is adopted in this study by applying the iterations to the new equation form. Let $y_{@i}(t)$ and $\dot{y}_{@i}(t)$ be the spring virtual elongation and its derivative in i^{th} iteration.

In the algorithm that will be presented below, time is discretized such that $y_{@i}(t)$ and $\dot{y}_{@i}(t)$ are approximated by the n dimensional vectors $[y_{@i}(t_1), y_{@i}(t_2), \dots, y_{@i}(t_n)]$

and $[\dot{y}_{@i}(t_1), \dot{y}_{@i}(t_2), \dots, \dot{y}_{@i}(t_n)]$, respectively. Here, t_i for $i = 1, 2, \dots, n$ are discretized time values such that $t_{i+1} = t_i + \Delta t$ (for $i = 1, 2, \dots, n - 1$) where Δt is a user selected time increment. Furthermore, $t_1 = 0$ and $t_n = T$.

The steps of the proposed algorithm are given below.

1. Assign appropriate guesses or already available data for the design variables $[k_3, m_2, m_3, m_6, I_6, y_0]$ and calculate A, B and C(t) in equation (2.22) accordingly.
2. Calculate spring virtual elongation profile of the i^{th} iteration, $y_{@i}(t)$, by using the derivative of the virtual elongation of the previous step. Assume initial velocity profile ($\dot{y}_{@0}(t)$) is constant and zero.

$$y_{@i}(t) = \sqrt{\frac{C(t) - B[\dot{y}_{@i-1}(t)]^2}{A}} \quad (2.31)$$

where $i \in 1, 2, 3, \dots$

$$\dot{y}_{@0}(t) = 0 \quad (2.32)$$

In this study, positive square root of $y_{@i}(t)$ has been utilized [see equation (2.31)]. Note that if the negative square root is used in equation (2.31), a different solution for $y_{@i}(t)$ would be obtained.

Note also that, one cannot find a physically realizable solution if the radicand in equation (2.31) is negative (for any time value).

3. By taking time derivative of the elongation profile calculated in the current iteration, numerically, calculate the next velocity profile guess ($\dot{y}_{@i}(t)$, $i \in 1, 2, 3, \dots$)
4. Repeat steps 2-3 until the root mean square of the error (ϵ) reduces to less than a specified threshold (ϵ_{max}) value where ϵ is defined via the equation

$$\epsilon = RMS\{A[y_{@i}(t)]^2 + B[\dot{y}_{@i}(t)]^2 - C(t)\} < \epsilon_{max} \quad (2.33)$$

Although this method is simple to implement, one should note that it might not converge to a solution for some cases. One should note the following regarding the convergence of the algorithm.

- Input should be a continuous function. Discontinuities in $C(t)$ would result in large changes in the derivative guesses.
- The stiffness to mass ratio (A/B) should be small. Note that as B goes to zero, the solution will converge to the initial guess given in equation (2.31) when ($i = 1$). As B increases, the kinetic energies of the links will be more dominant.

It is suggested that the design mass and inertia parameters inside the parameter B defined in equation (2.23) should be as small as possible in order to increase the convergence possibility of the solution.

It should be noted that the purpose of the iterative algorithm discussed in this section is to, numerically, solve [for $y(t)$] the first order non-linear differential equation given by equation (2.22). Other methods could also be employed to solve $y(t)$ from the aforementioned differential equation. Note that the initial condition $y(0)$, associated with the differential equation is free variable. Hence, if it is considered to be convenient, one may specify any suitable value for $y(0)$ before solving the differential equation (2.22).

Once the virtual elongation $y(t)$ is obtained, link 3 position (s_3) and MFG spring length (l_{mfg}) may be obtained by using equations (2.17) and (2.11) respectively. Link 3 velocity (\dot{s}_3) is then obtained by substituting $\dot{y}(t)$ into equation (2.18).

2.6. Centerline and Contact Curve Calculation on Slot Profile Links

In order to obtain the centerline vector, $c_y(t)$ (see Section 1.2.1) can be calculated via the equation

$$c_y(t) = b_2 - s_3(t) \quad (2.34)$$

Note that $c_x(t) = s_2(t)$, where $s_2(t)$ is already known (since it is an input).

Note that centerlines of the other rollers can be found by using $c_x(t)$ and $c_y(t)$, via equations (1.15) to (1.20).

In order to determine the position vector of the contact point (between the roller and the slot), an approach which is similar to the one presented in [4] is followed. Firstly, the unit tangent vector $\vec{p}(t)$ [which is tangent to the path of the center of the roller (on link 3)] is obtained via the equation

$$\begin{aligned}\vec{p}(t) &= \cos(\gamma) \vec{u}_1^{(3)} + \sin(\gamma) \vec{u}_2^{(3)} \\ &= \frac{1}{\sqrt{p(t)^2 + 1}} \vec{u}_1^{(3)} + \frac{p(t)}{\sqrt{p(t)^2 + 1}} \vec{u}_2^{(3)}\end{aligned}\quad (2.35)$$

Here, p is the slope of the tangent line (see Section 1.2.2.2) and γ is the angle shown in Figure 2.5. Now, if the contact is on side-1 (see Figure 2.5) of the slot, the position vector of the contact point (with respect to body fixed frame of link 3) will be given by

$$\overrightarrow{O_3 R_{32}} = \vec{c} + \vec{p}_{-90} r_6 \quad (2.36)$$

where the vector \vec{p}_{-90} is given by the equation

$$\vec{p}_{-90} = \frac{p(t)}{\sqrt{p(t)^2 + 1}} \vec{u}_1^{(3)} - \frac{1}{\sqrt{p(t)^2 + 1}} \vec{u}_2^{(3)} \quad (2.37)$$

If the contact is on the side-2, on the other hand, the position vector of the contact point will be given by

$$\overrightarrow{O_3 R_{32}} = \vec{c} + \vec{p}_{+90} r_6 \quad (2.38)$$

where the vector \vec{p}_{+90} is given by the equation

$$\vec{p}_{+90} = -\frac{p(t)}{\sqrt{p(t)^2 + 1}} \vec{u}_1^{(3)} + \frac{1}{\sqrt{p(t)^2 + 1}} \vec{u}_2^{(3)} \quad (2.39)$$

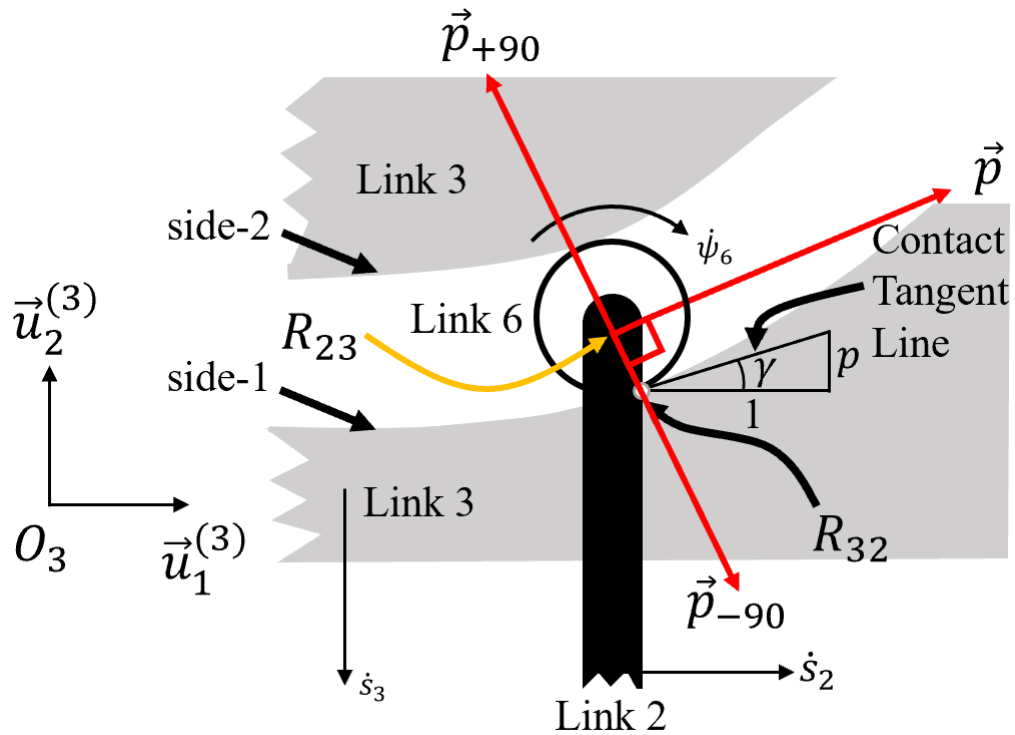


Figure 2.5. Demonstration for calculation of slot profile links contact points

2.7. Dynamic Force Analysis

Dynamic force analysis of MFG is performed in [6] and a simplified analysis is performed in [4]. After performing force analysis, one should check the normal forces at the slot profile – roller contact in order to make sure that the roller stays in contact with the profile.

In [4], the friction forces between the roller - slot profile contact, are included in the dynamic analysis. Furthermore, the conditions for slippage, or no slippage, are also discussed. However, in this study, for the mathematical case study which is to be used in the experiment, frictional forces at the contact point are neglected. Dynamic analysis is used for determining the normal forces on the slot profile when there is no friction. Therefore, it is sufficient to consider the free body diagram of link 3 only. The free-body diagram of link 3 is given in Figure 2.6

In Figure 2.6, the force vectors are defined with two indices i and j where \vec{F}_{ij} is the force applied by link i on the link j .

The normal forces \vec{F}_{63} and \vec{F}_{73} may be expressed, in terms of their components, as follows.

$$\begin{aligned}\vec{F}_{63} &= F_{63x}\vec{u}_1^{(1)} + F_{63y}\vec{u}_2^{(1)} \\ \vec{F}_{73} &= F_{73x}\vec{u}_1^{(1)} + F_{73y}\vec{u}_2^{(1)}\end{aligned}\tag{2.40}$$

Recalling the symmetry constraints discussed in Section 1.2 one has

$$\begin{aligned}F_{63x} &= -F_{73x} \\ F_{63y} &= F_{73y}\end{aligned}\tag{2.41}$$

Using equation (2.41), Newton's second law along the $\vec{u}_2^{(1)}$ direction yields

$$m_3\ddot{s}_3 = F_{s3} + 2F_{63y}\tag{2.42}$$

In equation (2.42), the acceleration of link 3 is denoted as \ddot{s}_3 . Once the MFG design is performed, one may calculate \ddot{s}_3 by taking the time derivative of \dot{s}_3 .

Furthermore, in equation (2.42), \vec{F}_{s3} is the force applied by the upper spring on link 3, which is given by

$$\vec{F}_{s3} = k_3(l_{mfg} - l_{free,mfg} + d_0)\vec{u}_2^{(1)} = F_{s3}\vec{u}_2^{(1)}\tag{2.43}$$

In equation (2.43), d_0 is the parameter used for extension springs with initial tension. d_0 is zero for other types of springs. For spring elongation vs force plot see Figure 2.2.

Using the slope (p) (see Figure 2.5), one obtains

$$F_{63x} = -pF_{63y} = \frac{\dot{s}_3}{\dot{s}_2}F_{63y}\tag{2.44}$$

Note that the slope (p) is infinity when the tangent line is vertical. Thus F_{63x} is zero when the slope is infinite.

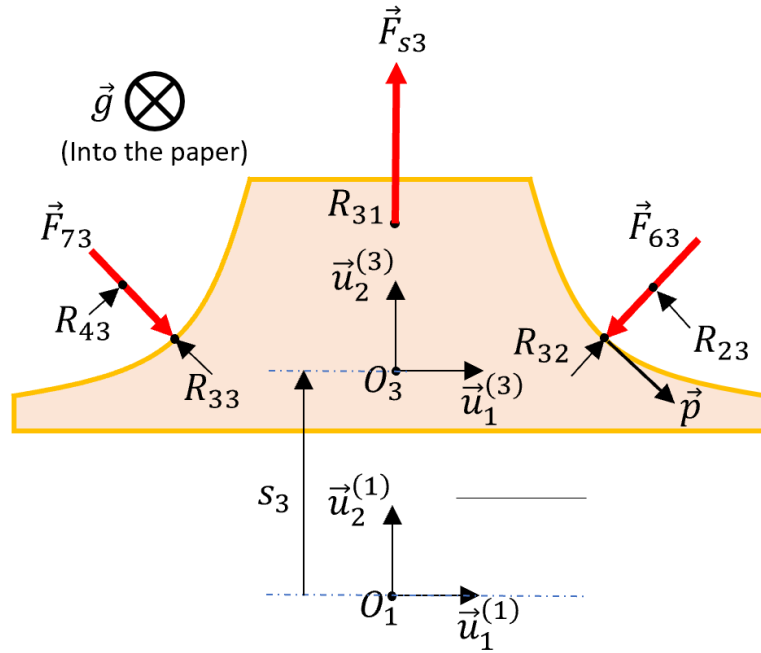


Figure 2.6. Free Body Diagram of link 3

The normal force on the slot contact may be written, by using equation (2.42), as follows.

$$\vec{F}_{63} = -p \frac{m_3 \ddot{s}_3 - F_{s3}}{2} \vec{u}_1^{(1)} + \frac{m_3 \ddot{s}_3 - F_{s3}}{2} \vec{u}_2^{(1)} \quad (2.45)$$

which yields the magnitude of the normal force given by

$$F_{63} = \sqrt{1 + p^2} \left(\frac{m_3 \ddot{s}_3 - F_{s3}}{2} \right) \quad (2.46)$$

2.8. Radius of Curvature Consideration

Once the path that the center of the roller traces on link 3 is obtained, the radius of the path should be calculated for each point on the path. Then, in order to avoid undercutting, the radius of the i^{th} roller, r_i , should be selected smaller than the radius of curvature at any point on the path. One may refer to [4] for more detailed information on this subject.

CHAPTER 3

PERFORMANCE OPTIMIZATION OF MACHINES USING MECHANICAL FORCE GENERATORS

3.1. Introduction

In this chapter, MFG power variation is designed in order to improve the efficiency of the actuator(s) which drives machine(s). The MFG is assumed to be connected either to twin machines or a machine with a merging system such that the forces on the MFG input links (links 2 & 4) are equal in magnitude and opposite in direction, as explained in Section 1.2.4.

As an actuator, only DC motors are considered in this study. However, some aspects of the design may also apply to other types of actuators. In the design, motion of the motor shaft is considered to be an input. Thus, only the torque of the motor is taken to be the design variable in the optimization algorithms.

In this chapter, the power flow from the input of the prime mover (i.e., an electric motor) to the output of the machine, including the mechanical and electrical losses, is considered. Using energy balance equations, three optimization methods to improve the performance of a machine are proposed. The first method minimizes the maximum motor power, the second one minimizes the maximum motor torque, and the last one minimizes the energy losses of motor. The MFG power calculated with the optimization methods satisfies the first constraint on the MFG power given in Section 1.2.5. However, it may not satisfy the second power constraint when the speed of link 2 of MFG is zero.

The second constraint on the MFG power is satisfied by employing spline fit methods which approximates the asymptotic discontinuities of the MFG force (as suggested in [3]). The proposed method is improved by taking the force applied when speed of link

2 is zero into account. This improvement modifies the MFG power variation slightly, such that the power variation does not satisfy the first constraint. A new method is introduced in order to compensate for this deviation, such that both of the MFG constraints are satisfied.

The obtained resultant power variation can lead to MFGs with closed slot profiles (which are harder to implement physically compared to the open profiles as defined in Section 1.3.2.1).

Since open slot profiles are easier to manufacture, a sufficient but not necessary condition that will result in open profiles are obtained. A method to modify certain power variations to obtain an MFG with open slot profile is proposed.

Performances of the optimization methods are evaluated using a simulation scenario discussed in [4]. Expected results have been observed.

3.2. Definition of a Mechanical System to be Optimized

In this section, the mechanical system to be optimized is defined. Energy balance equations are utilized, since determining the power variations of the MFG is the objective. The power loss sources are discussed. The power losses associated with the motor are investigated rigorously.

3.2.1. Power Transmission Equations

In this study, it is assumed that an electric motor transmits power to a machine to perform a known task. Therefore, the motion of the motor shaft, the mechanical energy of the machine and the work done by the machine are considered to be known (with respect to time) prior to the MFG design. The MFG input links are assumed to be connected to either the output links of a machine with two symmetrical force inputs, to a machine - MFG merging system, or to the output links of two twin machines as explained in Section 1.2.4.

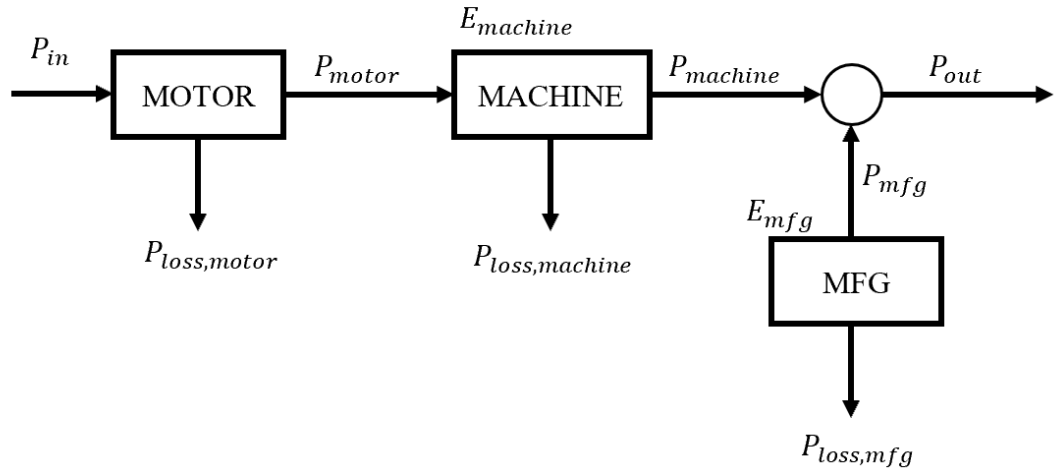


Figure 3.1. Power flow diagram

Power flow diagram is given in Figure 3.1. The power input and the power output of each component is labeled by an arrow. The components are shown with blocks in the figure, and they can be considered as control volumes. The mechanical energy of a block is labeled on the top of the block. There is no mechanical energy label for the motor since, in this study, the inertia of the motor is included in the machine.

In Figure 3.1, the motor and the machine are shown with a single block. If twin machines are used in the design, then the power input (P_{in}), motor power losses ($P_{loss,motor}$) and the motor mechanical output power (P_{motor}) can be considered to be the values for the sum of the two motors. Similarly, the mechanical energy of machine ($E_{machine}$), power loss of the machine ($P_{loss,machine}$) and the power output of the machine ($P_{machine}$) can be regarded as the sum of the values of the two identical machines.

The motor receives electrical power (P_{in}) and converts it to mechanical power (P_{motor}). Losses in the conversion are denoted as $P_{loss,motor}$. The mechanical energy of the motor which is the kinetic energy due to the rotation of the rotor inertia is assumed to be included in the machine. Thus, it is not shown in equation (3.1).

$$P_{in} = P_{motor} + P_{loss,motor} \quad (3.1)$$

The machine in the figure receives mechanical power from the motor and transmits it to the surroundings and/or a load. During the transmission, some of the power is spent against the inertial, gravitational and elastic forces and moments in the machine. Thus, the mechanical energy of the machine ($E_{machine}$) changes. Some of the received power is lost due to friction, denoted as $P_{loss,machine}$. The remaining power is transmitted to the surroundings and/or the load denoted as $P_{machine}$. The energy balance equation for the machine can be written as

$$\dot{E}_{machine} = P_{motor} - P_{loss,machine} - P_{machine} \quad (3.2)$$

where $\dot{E}_{machine}$ is the rate of change of mechanical energy of the machine with respect to time.

When the MFG is not connected, $P_{machine}$ is equal to the output power (P_{out}). The output power is the rate of change of the work done by the machine and MFG on the surroundings or load with respect to time. When the MFG is connected to the machine, the output power can be calculated as

$$P_{out} = P_{machine} + P_{mfg} \quad (3.3)$$

where P_{mfg} corresponds to the power of the work done by MFG on the machine.

The MFG also has its own losses ($P_{loss,mfg}$) and mechanical energy (E_{mfg}). The positive direction of the MFG power is assumed to be from MFG to the machine. Therefore, P_{mfg} appears as negative in equation (3.4).

$$\dot{E}_{mfg} = -P_{mfg} - P_{loss,mfg} \quad (3.4)$$

Work done by the MFG from time equals 0 to time equals any time, $W_{mfg}(t)$, on the machine can be obtained by taking integral of equation (3.4), disregarding the power loss ($P_{loss,mfg}$). Hence,

$$W_{mfg} = \int_0^t P_{mfg} dt \quad (3.5)$$

Optimizations in this study neglect the power losses at the machine. Hence, consider, now, the lossless case for the machine where $P_{loss,machine} = 0$, and define the task power (P_{task}) to be the motor power required to run a task when the MFG is not connected. Hence,

$$P_{task} = \dot{E}_{machine} + P_{out} \quad (3.6)$$

When the MFG is connected, on the other hand, power balance equation becomes

$$P_{out} + \dot{E}_{machine} = P_{motor} + P_{mfg} \quad (3.7)$$

Thus, by inserting equation (3.6) into (3.7), P_{task} can be represented in terms of P_{motor} and P_{mfg} as

$$P_{task} = P_{motor} + P_{mfg} \quad (3.8)$$

In this chapter, P_{motor} is regarded to be the motor mechanical output power when the MFG is connected to the machine. For the motor mechanical output power when MFG is not connected, P_{task} is used.

Now, define the task force, F_{task} , to be a virtual force acting on the output link of the machine, as if the machine is driven from its output link, without the application of an MFG. This variable is used to compare the force applied by MFG, denoted as F_{mfg} , on the machine. For example, if F_{mfg} is equal to F_{task} then no torque output from the motor will be required. Since the losses on the machine are neglected, F_{task} can be calculated by using P_{task} and the velocity of the output link of the machine. Since the MFG is rigidly connected to the output links of the machine, the velocity of the output link will be the velocity of link 2 of the MFG (i.e., \dot{s}_2) can be used. Equation (3.9) may be used to calculate F_{task} . Note that, one may also calculate the force F_{task} from the dynamic force analysis of the machine.

$$F_{task} = P_{task}/\dot{s}_2 \quad (3.9)$$

provided that $\dot{s}_2 \neq 0$. Similarly, define task torque T_{task} as the required motor reaction torque without application of the MFG, disregarding the losses of the machine. T_{task} can be calculated by using P_{task} and the motor shaft speed of ω , given by the equation

$$T_{task} = P_{task}/\omega \quad (3.10)$$

provided that $\omega \neq 0$. Let the MFG force, F_{mfg} , be defined as the force applied by MFG on the machine, which generates the work P_{mfg} in accordance with the equation

$$P_{mfg} = F_{mfg}\dot{s}_2 \quad (3.11)$$

$$F_{mfg} = -2F_2$$

$$F_{mfg} = \frac{P_{mfg}}{\dot{s}_2} \quad (3.12)$$

provided that $\dot{s}_2 \neq 0$. In equation (3.11) the F_2 corresponds to the force applied on link 2 of the MFG in the sense of the unit vector $\vec{u}_1^{(1)}$ as shown in Figure 1.1. Note that F_2 is equal in magnitude and in opposite in direction to the force applied on link 4 of the MFG.

Finally, define the motor torque (T_{motor}) to be the net output torque of the motor when MFG is applied. Clearly,

$$T_{motor} = P_{motor}/\omega \quad (3.13)$$

provided that $\omega \neq 0$.

3.2.2. Motor Based Losses

In order to investigate the power losses associated with at the motor, the mathematical model of DC motors need to be considered. A typical model includes a series connected resistance (R), an inductance (L) and a potential difference caused by the back electromotive force (V_{emf}) as shown in Figure 3.2.

Let the voltage input and the motor current be V_{in} and i_m , respectively, then Kirchhoff's loop law written for the loop in Figure 3.2 yields

$$V_{in} = i_m R + \frac{di_m}{dt} L + V_{emf} \quad (3.14)$$

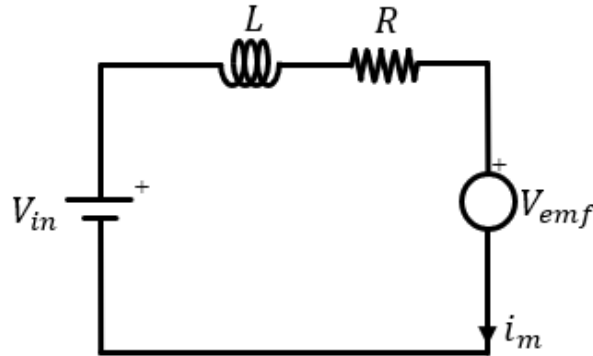


Figure 3.2. DC Motor mathematical model

The motor torque (T_{motor}) and the motor current (i_m) are related via the torque constant (k_T), as given below.

$$k_T i_m = T_{motor} + T_f \quad (3.15)$$

Here, T_{motor} is the torque delivered to the machine and T_f is the friction torque (see equation (3.18) for components of the friction torque). The motor inertia is not included in this equation since it is taken into account in the machine.

The motor shaft speed (ω) and the back emf voltage (V_{emf}) are related via the back emf constant (k_E) such that:

$$V_{emf} = k_E \omega \quad (3.16)$$

It is shown in [7] that when k_T and k_E are defined in SI units, they are equal to each other. In this study, k_T and k_E are both used in SI units.

$$k_T = k_E \quad (3.17)$$

Power losses of DC motors may be divided into torque-sensitive and speed-sensitive losses (see [7]). Permanent magnet DC motor power distribution is given in Figure 3.3 and the losses are investigated in following subsections.

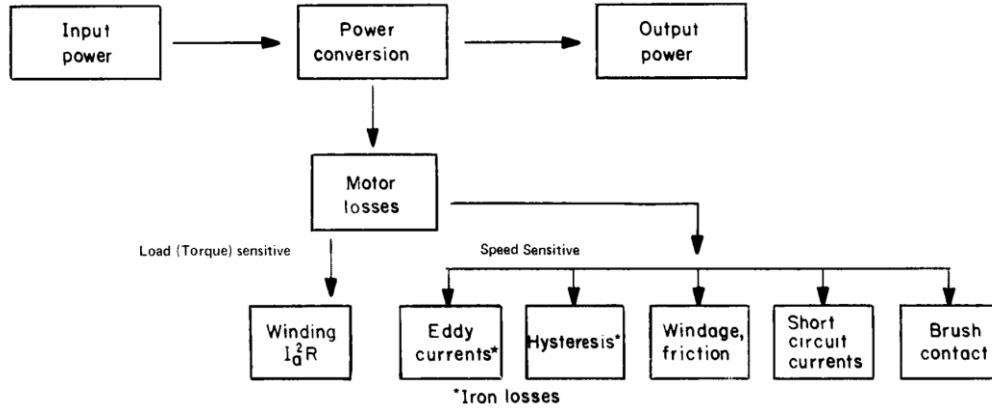


Figure 3.3. Permanent DC motor power losses [7]

3.2.2.1. Copper Losses and Speed Related Losses

The load-sensitive losses are known as winding losses (or, copper) losses which leads to heat generation due to the current passing through the motor coils. Speed-sensitive losses, on the other hand, lead to friction torque (T_f). T_f may be represented as the following equation

$$T_f = c_1 + c_2 \omega \quad (3.18)$$

where c_1 and c_2 are positive constants.

When calculating the power dissipation, equations (3.14) to (3.18) are utilized. Since inductance (L) has very small effect, it is usually neglected [7]. Hence, it is also omitted in this study. Then for the calculation of the power consumption of the motor, equation (3.14) yields

$$V_{in} = i_m R + k_E \omega \quad (3.19)$$

Equations (3.15) and (3.18), on the other hand, lead to

$$i_m = \frac{1}{k_T} (T_{motor} + c_1 + c_2 \omega) \quad (3.20)$$

Then using equations (3.19) and (3.20), the input power is obtained as:

$$\begin{aligned} P_{in} &= i_m V_{in} \\ &= i_m^2 R + \omega (T_{motor} + c_1 + c_2 \omega) \\ &= \omega T_{motor} + i_m^2 R + c_1 \omega + c_2 \omega^2 \end{aligned} \quad (3.21)$$

In equation (3.21), the first term yields the transmitted mechanical power (P_{motor}) to the machine, the second term yields the copper losses ($P_{loss,copper}$) and the remaining terms correspond to the speed sensitive losses, i.e.,

$$P_{motor} = \omega T_{motor} \quad (3.22)$$

$$P_{loss,copper} = i_m^2 R \quad (3.23)$$

3.2.2.2. Motor Brake Related Losses

In addition to the transmission losses explained above, there are also losses due to the braking in the system. Braking is defined to be deceleration of the motor shaft speed. During braking, the mechanical power output of the motor is negative ($P_{motor} < 0$). Thus, motor receives power from the mechanism. If the sum of the received power (P_{motor}) and the motor losses ($P_{loss,motor}$) is negative, then the motor generates power. The sum of the powers is denoted as P in this chapter [see equation (3.24)]. Although the losses are neglected in [3] and [4], they are found to be high in the results of the experiments given in Chapter 6. Thus, they are included in this study.

The types of braking are divided into three in [3][4], which are plugging braking, dynamic braking, and regenerative braking.

In regenerative braking, when the sum of power (P) is negative, some of the power is fed back to the power source, and stored for later use (if the power source supports

regeneration). The quantity of the stored energy depends on the regeneration efficiency denoted with η , where $0 < \eta \leq 1$, for regenerative braking.

In plugging type braking, the motor draws the power P from the power supply equal to the variable P . Thus, $\eta = -1$.

In dynamic braking, there is an additional braking mechanism which applies friction to the motor shaft. Thus, the rotational energy of the motor is converted to heat. Hence, no power is drawn by the motor from the power source. Thus, $\eta = 0$ for dynamic braking.

DC motor power consumption calculation corresponding to the three types of braking method is given as below.

$$P_{in} = \begin{cases} P & , \text{if } P \geq 0 \\ \eta P & , \text{if } P < 0 \end{cases} \quad (3.24)$$

$$P = P_{motor} + P_{loss,motor}$$

The value η depends on the braking type of the motor as explained before, which is shown in Table 3.1 for convenience.

For the plugging type braking, since $\eta = -1$, the following equation can be used to calculate the power input of the motor.

$$P_{in} = |P_{motor} + P_{loss,motor}| \quad (3.25)$$

Table 3.1. η values for different braking types

η	Braking type
(0,1]	Regenerative Brake
0	Dynamic Brake
-1	Plugging type Braking

3.2.2.3. Motor Driving Related Losses

There are also so called the torque ripple losses due to the motor and the driver of the motor. A wide variety of DC motors are driven with pulse width modulation (PWM), in which the voltage input (V_{in}) shown in Figure 3.2 is modulated. The modulation creates current ripple depending on the electrical time constant of the motor ($\tau_e = L/R$), the modulation frequency and the duty ratio. In order to decrease the ripple, there are application notes from the motor producers (see, for instance, [8] and [9]). Losses due to the driver are investigated in [10].

The ripples in the motor current lead to the copper losses defined in Section 3.2.2.1. When there are ripples in the motor current, root mean square (RMS) of current will be greater than the average current. If the motor current is calculated by using the motor torque without ripple and the torque constant, then the calculated current will be the average current within one period of the PWM. Hence, power loss calculations based on the torque output will become less correct as the ratio of RMS to the average current increases.

In order to demonstrate the current ripples, an experiment is conducted with FAULHABER 2342_CR_012 [11] model permanent magnet DC motor with %50 duty cycle and 20 kHz PWM frequency. The motor current is read by inserting a sense resistor with 0.47Ω resistance in series to the DC motor terminals. The voltage drop across the sense resistor is shown in Figure 3.4. In order to calculate the motor current, the voltage drop across the sense resistor is used.

From the figure, note that RMS current is $172 \text{ mV}/0.47 \Omega = 365.96 \text{ mA}$ while mean current is $25.4 \text{ mV}/0.47 \Omega = 54.04 \text{ mA}$. This indicates that the copper losses estimated by the average torque is $(25.4/172)^2 = 0.02$ times of the actual power loss.

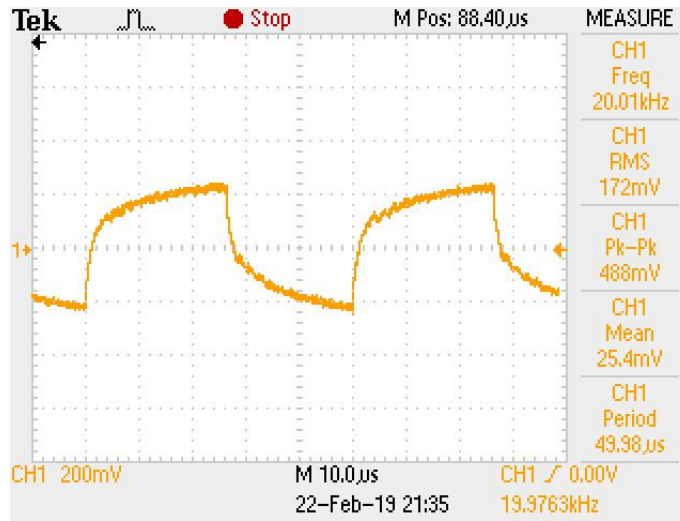


Figure 3.4. DC Motor current ripple experiment with %50 Duty cycle and 20 kHz PWM frequency

3.2.3. Machine and MFG Losses

The losses corresponding to the machine can be modeled as mechanical losses i.e., the losses due to the Coulomb friction and viscous friction between the machine links. The friction models and solution methods for different types of joints have been investigated deeply in [3]. Since the power losses of the machine are not used in optimization, they are not further presented in study.

3.3. MFG Power Flow Design

In this chapter, the MFG power variation for improving a specific performance of a machine is determined. The energy balance equations defined in Section 3.2.1 are used. The motion of the motor output shaft (ω) is known and considered to be an input in the optimizations. Therefore, the design variable is either the motor torque (T_{motor}), or the power output of the motor (P_{motor}).

There are two constraints for the optimization which are the MFG power constraints defined in Section 1.2.5. The first constraint states that the MFG should apply conservative forces (see equation (1.41)). The second constraint is that the MFG

cannot provide any power output when velocity of its input links (Links 2 & 4 of the MFG) is zero ,i.e., $\dot{s}_2 = 0$, (see equation (1.42)).

The performance indices corresponding to the three optimization methods are defined in the following subsections.

3.3.1. Performance Optimization Guideline

In order to calculate the MFG power variation, the following algorithm is proposed.

1. Obtain the variables ($F_{task}, P_{task}, T_{task}$) of the original machine, when the MFG is not applied. These variables (which are function of time) can be obtained by modeling the machine and the external load applied on the machine.
2. Find the optimum variables ($P_{motor}^*, T_{motor}^*, F_{mfg}^*, P_{mfg}^*$) that satisfies the MFG constraint defined by equation (1.41) using the performance optimization methods given in Section 3.3.3. The starred quantities are the optimal variations which are the outputs of the section.
3. Take corrective action on the optimum variables thus obtained in order to satisfy the second constraint of the MFG power defined by (1.42). Use the spline interpolation method given in 3.3.4 to obtain temporary variables which are named as ($P'_{motor}, T'_{motor}, F'_{mfg}, P'_{mfg}$).
4. Compensate for the negative effect of the 3rd step on equation (1.41) by taking the final correcting action. Hence, both constraint equations (1.41) and (1.42) will be satisfied. Use the method given in 3.3.5. The output variables of this step are named as $P_{motor}, P_{mfg}, T_{motor}, F_{mfg}$.
5. Determine the performance measure corresponding to the optimization method (defined in Section 3.3.3) by using the output variables obtained in step 4.

3.3.2. Performance Measures of the Optimization

Three performance measurement indices have been used in this study. Performance indices are normalized so that the improvement can be compared with the performance of the original mechanism where MFG is not applied. The indices vary between zero

and one if there is an improvement in the performance; and are greater than one if the MFG made the performance of the machine even worse. The performance indices are defined for one period (T) of task.

The first optimization measure, J_P , is related to the minimization of the maximum power output of the motor. J_P is defined via equation

$$J_P = \frac{\max(P_{motor})}{\max(P_{task})} \quad (3.26)$$

The second optimization measure, J_T , is related to the minimization of the maximum torque which is the output torque of the motor. J_T is defined via equation

$$J_T = \frac{\max(T_{motor})}{\max(T_{task})} \quad (3.27)$$

The last measure, J_E , is related to the minimization of the total energy loss of the motor in one period. In this study, only the copper losses are considered. Neglecting the speed-sensitive losses in equation (3.20) and by substituting equation (3.20) into (3.23), one obtains

$$P_{loss,copper} = \left(\frac{T_{motor}}{k_T} \right)^2 R \quad (3.28)$$

Then, the optimization measure J_E is calculated by dividing the copper losses when MFG is applied to the loss when the original machine is used, i.e.,

$$J_E = \frac{\int_0^T T_{motor}^2 dt}{\int_0^T T_{task}^2 dt} \quad (3.29)$$

Recall that T_{task} is defined as the motor torque when MFG is not applied. The minimization of the energy losses is valid for all types of braking methods mentioned in Section 3.2.2.2 such that $P_{loss,motor}$ is minimized in equation (3.24).

3.3.3. Performance Optimization with MFG's

The optimization methods use analytic techniques to produce optimum design variables that satisfy the first constraint related to MFG (see (1.41)).

3.3.3.1. Minimizing the Maximum Power Requirement

The objective of this optimization algorithm is to find $P_{mfg}^*(t)$ which minimizes the maximum power requirement of the motor, $\max(P_{motor})$, while satisfying equation (1.41); and without changing the speed of the motor shaft $\omega(t)$ and the output power of the machine $P_{out}(t)$. Recalling that the losses on the machine and the MFG are neglected in the design, the total work done by the motor in one period (T) can be calculated, i.e.,

$$\begin{aligned} E_{motor} &= \int_0^T P_{motor} dt \\ &= \int_0^T P_{out} + \dot{E}_{machine} - P_{mfg} dt \\ &= \int_0^T P_{out} dt + \int_0^T \dot{E}_{machine} dt + \int_0^T P_{mfg} dt \end{aligned} \quad (3.30)$$

where P_{motor} is obtained from equation (3.7). Note that, the last term is zero due to the MFG power constraint given by equation (1.41). The second term in equation (3.30) is also zero since the machine returns to its initial state after one period. Therefore, the net change in mechanical energy of the machine in one period is zero, i.e.,

$$\int_0^T \dot{E}_{machine} dt = \Delta E_{machine}|_0^T = 0 \quad (3.31)$$

Thus, equation (3.30) yields

$$E_{motor} = \int_0^T P_{out} dt = E_{out} \quad (3.32)$$

Since the total work done by the motor on the mechanism at each period is known, in order to minimize the maximum motor power, P_{motor} should be equal to the average

power as it is done in [3]. Clearly, if the motor power is less than the average power output at some point in time, in order to satisfy equation (3.32), at some other points in time the motor power will be seen as larger than the average. Thus, the optimum solution (denoted by an asterisk in superscript) is the average power given by

$$P_{motor}^* = \frac{E_{out}}{T} \quad (3.33)$$

Note that P_{motor}^* in equation (3.33) is always positive value. Therefore, the motor would never need to brake. Thus, by applying this method, the requirement for using dynamic and regenerative braking vanishes.

Note that if the machine does conservative work on the load, then P_{motor}^* is zero. This implies that conservative forces can be fully compensated by the MFG.

Once the optimum motor power is calculated using equation (3.33), one can solve the optimum MFG power (P_{mfg}^*) from equation (3.6) and (3.8) to obtain

$$P_{mfg}^* = P_{task} - P_{motor}^* \quad (3.34)$$

The optimum MFG force (F_{mfg}^*) and the optimum motor torque (T_{motor}^*) can then be found by using equations (3.33) and (3.34) in (3.11)(3.13) and (3.11), respectively.

3.3.3.2. Minimizing the Maximum Torque

The maximum motor torque can be minimized similar to the minimization of the maximum power. In this optimization, however, the magnitude of the optimum torque is assumed to be constant. The sign of the torque depends on the sign of motor shaft speed (ω) to obtain positive motor power (P_{motor}) all times such that

$$sign(\omega)T_{motor}^* = constant > 0 \quad (3.35)$$

and

$$\omega = sign(\omega)|\omega| \quad (3.36)$$

The energy output equation in (3.32) may also be written in terms of the motor torque (T_{motor}^*) and motor shaft angular velocity (ω), yielding

$$E_{out} = \int_0^T P_{motor}^* dt = \int_0^T T_{motor}^* \omega dt \quad (3.37)$$

By substituting equations (3.35) and (3.36) into (3.37), one obtains

$$E_{out} = \int_0^T T_{motor}^* \text{sign}(\omega) |\omega| dt = \text{sign}(\omega) T_{motor}^* \int_0^T |\omega| dt \quad (3.38)$$

which, upon solving for T_{motor}^* yields

$$T_{motor}^* = \frac{\text{sign}(\omega) E_{out}}{\int_0^T |\omega| dt} \quad (3.39)$$

Since $P_{motor}^* = T_{motor}^* \omega$, equation (3.39) yields

$$P_{motor}^* = \frac{\text{sign}(\omega) E_{out}}{\int_0^T |\omega| dt} \omega \quad (3.40)$$

Substituting equation (3.36) into (3.40) one obtains

$$P_{motor}^* = \frac{|\omega| E_{out}}{\int_0^T |\omega| dt} \quad (3.41)$$

Note that P_{motor}^* in equation (3.41) is always positive value. Therefore, the motor would never need to brake. Thus, by applying this method, the requirement for dynamic and regenerative braking vanishes.

Equation (3.39) indicates that, if the output load is a conservative force (i.e., $E_{out} = 0$), then the optimum motor torque is zero. This shows that conservative loads on the machine can be fully compensated by an MFG.

One can easily observe from equation (3.41) that if the angular velocity of the motor shaft (ω) is constant, then the power output of the motor will also be constant as well. Then, this solution is also solution to minimizing the maximum power.

Optimum motor power and the motor torque for ω is constant are calculated using the following expressions:

$$\int_0^T |\omega| dt = |\omega|T, \quad \text{if } \omega \text{ is constant} \quad (3.42)$$

Note that equation (3.42) can also be expressed as:

$$|\omega|T = \omega \text{ sign}(\omega)T \quad (3.43)$$

Using equation (3.43) in (3.39) one obtains the optimum torque output of the motor when the motor shaft velocity is constant:

$$T_{motor}^* = \frac{E_{out}}{\omega T}, \quad \text{if } \omega \text{ is constant} \quad (3.44)$$

Using equation (3.42) in (3.41) one obtains the optimum power output of the motor when the motor shaft velocity is constant:

$$P_{motor}^* = \frac{E_{out}}{T}, \quad \text{if } \omega \text{ is constant} \quad (3.45)$$

Note that the expression for the optimum motor power in equation (3.45) is the same as the expression in (3.33). Therefore, the solution is optimum for both of the optimization methods when ω is constant.

Optimum MFG power (P_{mfg}^*) can be found by substituting P_{motor}^* in equation (3.34). The optimum MFG force (F_{mfg}^*) can be found by using equation (3.41) in (3.11).

3.3.3.3. Minimizing the Copper Losses on the Motor

This optimization also uses the fact that the total energy output required to accomplish a specific task is fixed. The copper losses resulting from only the motor torque was given in (3.28) is repeated here for convenience:

$$P_{loss,copper} = Ri^2 = \frac{R}{k_T^2} T_{motor}^2 \quad (3.46)$$

The coefficient of T_{motor}^2 in equation (3.46) is the “ K ” mentioned in [4] (in which the gear reduction ratio between the motor shaft and the machine input shaft is also included in K). Hence, equation (3.46) may be expressed as

$$P_{loss,copper} = KT_{motor}^2 \quad (3.47)$$

It follows from equation (3.47) that, minimization of the copper loss requires T_{motor}^2 term. However, since the work done by the motor is known from equation (3.32), there is a constraint on the motor torque so that,

$$E_{out} = \int_0^T T_{motor} \omega dt \quad (3.48)$$

is be satisfied.

Constrained minimization of functionals (see, for instance, [12]) has been utilized to solve this optimization problem. In the aforementioned problem, there is an integral constraint, which is also known as an isoperimetric constraint.

In order to solve the problem, the functionals (H) and augmented functions (H^*) defined in [12] are used. The functional (H) to be extremized is

$$H = \int_0^T T_{motor}^2 dt \quad (3.49)$$

The integral constraint to be applied, on the other hand, is

$$\int_0^T T_{motor} \omega dt = E_{out} \quad (3.50)$$

where, E_{out} is constant and known. Firstly, define the state variables $x_1(t)$ and $x_2(t)$ via the equations

$$\begin{aligned} x_1(t) &= \int_0^t T_{motor} \omega dt \\ x_2(t) &= T_{motor} \omega \end{aligned} \quad (3.51)$$

$$\text{where } \dot{x}_1 - x_2 = 0$$

subject to the boundary conditions $x_1(0) = 0$ and $x_1(T) = E_{out}$

Now, form the augmented function (H^*) using the Lagrange multiplier (λ) and equations (3.49), (3.51) as

$$H^* = \frac{1}{\omega^2} x_2^2 + \lambda(\dot{x}_1 - x_2) \quad (3.52)$$

The Euler equation for the problem is

$$\frac{\delta H^*}{\delta x} - \frac{d}{dt} \left(\frac{\delta H^*}{\delta \dot{x}} \right) = 0 \quad (3.53)$$

Application of equation (3.53) to the first state (x_1) yields

$$\frac{\delta H^*}{\delta x_1} = 0, \quad \frac{\delta H^*}{\delta \dot{x}_1} = \lambda \quad \rightarrow \quad \dot{\lambda} = 0 \rightarrow \lambda = \text{constant} \quad (3.54)$$

Application of equation (3.53) to second state (x_2) yields

$$\frac{\delta H^*}{\delta x_2} = \frac{2}{\omega^2} x_2 - \lambda, \quad \frac{\delta H^*}{\delta \dot{x}_2} = 0 \quad \rightarrow \quad x_2 = \lambda \omega^2 / 2 \quad (3.55)$$

Integrating $x_2(t)$, one may obtain $x_1(t)$ as follows.

$$x_1(t) = \frac{\lambda}{2} \int_0^t \omega^2 dt \quad (3.56)$$

Lagrange multiplier λ may be found by using equation (3.56) and the boundary condition $x_1(T) = E_{out}$ as follows.

$$x_1(T) = \frac{\lambda}{2} \int_0^T \omega^2 dt = E_{out} \quad (3.57)$$

$$\lambda = \frac{2E_{out}}{\int_0^T \omega^2 dt}$$

Substituting λ from equation (3.57) into equation (3.55); and then substituting the result in equation (3.51) and solving for T_{motor} , one obtains the optimum motor torque, T_{motor}^* , given by equation (3.58).

$$T_{motor}^* = \frac{E_{out} \omega}{\int_0^T \omega^2 dt} \quad (3.58)$$

which leads to

$$P_{motor}^* = \frac{E_{out}\omega^2}{\int_0^T \omega^2 dt} \quad (3.59)$$

Optimum MFG power (P_{mfg}^*) can then be found by substituting P_{motor}^* into equation (3.34). The optimum MFG force (F_{mfg}^*) can be found by substituting the P_{mfg}^* in (3.12) (3.11).

Note that P_{motor}^* obtained via equation (3.59) is always positive. Therefore, the motor would never need to brake. Thus, by applying this method, the requirement of the dynamic and regenerative braking vanishes.

Similar to the previous optimization methods equations (3.58) and (3.59) indicate that any conservative load force can be compensated fully by the MFG (since the optimum motor output power is zero).

If ω is constant, then $\int_0^T \omega^2 dt = \omega^2 T$. Hence equation (3.59) yields:

If ω is constant:

$$P_{motor}^* = \frac{E_{out}}{T} \quad (3.60)$$

Note that when the motor speed ω is constant, the P_{motor}^* expressions for all of the optimization methods are the same, as can be seen from equations (3.33), (3.45) and (3.60).

3.3.4. Zero-Speed Crossing Compensation

Since the performance optimization methods which are proposed previously do not take the second limitation of MFG given in (1.42) into account, they might require non-zero power from the motor at its zero speed ($\omega = 0$), or require non-zero power from MFG when its power transmitting links (links 2 & 4) have zero speed ($\dot{s}_2 = 0$).

Denote t_{cri} to be the i^{th} critical time where \dot{s}_2 and/or ω is equal to zero. When $P_{mfg}^*(t_{cri}) \neq 0$, an asymptotic discontinuity occurs in the F_{mfg}^* versus t plot at the i^{th} critical time (see equation (3.12)).

This problem has been observed in [3] and has been overcome by approximating the asymptotic discontinuities with interpolating a polynomial spline. The suggested spline starts at a specified time (t_{sp}) before the i^{th} critical time (t_{cri}) (being tangent to the F_{mfg}^* curve) and ends at the time ($t_{cri} + t_{sp}$), again, being tangent to the F_{mfg}^* curve. The approximation utilized in [3] is demonstrated in Figure 3.5. In the figure, the dashed line refers to F_{mfg}^* , and the continuous line refers to F_{mfg}' . Note that, outside the approximation intervals, both curves coincide. Note also that, $F_{mfg}'(t_{cr})$ is not specified. The curve obtained after the approximation is denoted as F_{mfg}' .

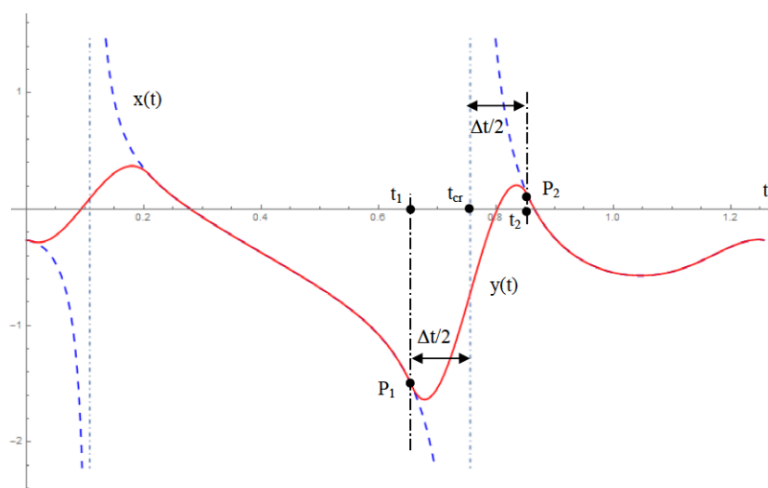


Figure 3.5. Approximation method proposed in [3]

In this study, two splines are utilized to approximate the task force at and around the critical time. Recall that task force is the force to drive mechanism when MFG is not applied. Therefore, as the MFG force gets closer to the task force, the motor torque will decrease. This improves the performance of the spline fitting algorithm. Similar to the previous method, the approximated curve starts at time ($t_{cri} - t_{sp}$) and ends at

the time t_{cri} . The slope at the starting points of the first approximated curve is equal to the slope of $F_{mfg}^*(t_{cri} - t_{sp})$. However, the end of the first approximated curve is tangent to $F_{task}(t_{cri}^-)$. The starting point of the second approximated curve is tangent to $F_{task}(t_{cri}^+)$ and the endpoint is tangent to the $F_{mfg}^*(t_{cri} + t_{sp})$. For generation of splines one may refer to [13]. The approximation method used in this study is shown in Figure 3.6. In the example, F_{task} is given discontinuous at the critical time ($t_{cr1} = 0.5$ seconds) and the specified time is selected as $t_{sp} = 0.0075$ seconds.

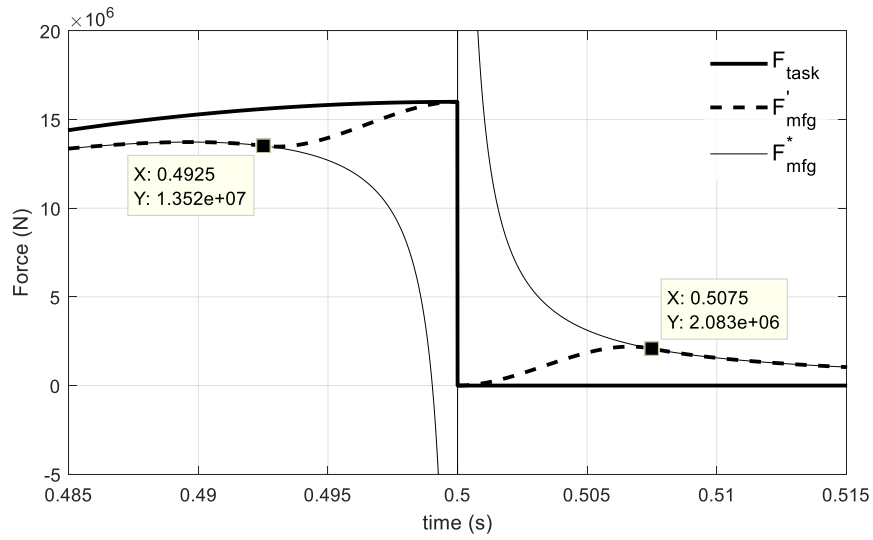


Figure 3.6. Approximation method used in this study

Note that the force at the critical time can be selected freely since the power will be zero anyway (Noting that $\dot{s}(t_{cr}) = 0$).

Once the approximated curve F'_{mfg} is obtained, one may calculate the temporary variables P'_{mfg} , P'_{motor} and T'_{motor} by using equations (3.11), (3.8) and (3.13) respectively. Note that F^*_{mfg} did satisfy the MFG power constraint equation (1.41). Due to the approximation, this constraint is violated. This is corrected in the algorithm given in the next section.

3.3.5. Energy Drift Compensation

Once the temporary variables (P'_{motor} , T'_{motor} , F'_{mfg} , P'_{mfg}) are calculated in the previous section, one may adjust the motor power to make MFG power satisfy the power constraint equation (1.41). This can be done by the following equation:

$$P_{motor} = P'_{motor} \frac{E_{out}}{\int_0^T P'_{motor} dt} \quad (3.61)$$

Note that in equation (3.61), the motor power P'_{motor} , which is a function of time, is multiplied with a positive constant value to obtain P_{motor} . Therefore, the sign of the motor power P'_{motor} does not change. In equations (3.33), (3.41) and (3.59), it has been shown that P'_{motor} always takes positive values. Since this method does not change the sign of the motor power, it can be concluded that in all of the optimization methods and the following corrective methods, braking is not required when the MFG is applied. If the original machine required a motor with dynamic or regenerative braking, the machine with MFG does not require such braking types. Hence, the cost of the actuator decreases.

3.4. MFG Design with Open Slot Profile

Since open slot profiles are easier to implement physically, it is desirable to improve the machine performance by using them rather than closed slot profiles. Recall that open and closed profile types are discussed in Section 1.3.2.1.

In this section, a method, which requires the machine output link position and velocity (s_2 & \dot{s}_2) and the work done by the MFG (W_{mfg}) as inputs; and which predicts whether the resulting MFG design is open or closed profile is introduced. Recall that W_{mfg} , which is a function of time, is the integral of the MFG power i.e.,

$$W_{mfg} = \int_0^t P_{mfg} dt \quad (3.62)$$

If the resulting MFG design has closed slot profile links, a method (to update given W_{mfg}) to obtain an MFG with an open slot profile is proposed.

3.4.1. Open Slot Profile Determination

In this section, a sufficient but not necessary condition which ensures MFGs with open slot profiles is introduced. The condition for guaranteeing an open slot profile is related to the variables s_2 , \dot{s}_2 and W_{mfg} . The first two variables are the inputs to the MFG power design. In order to obtain W_{mfg} , on the other hand, one may use the methods proposed in Section 3.3.

The governing equation (2.22) for the MFG design is repeated below for convenience.

$$\begin{aligned} Ay^2 + B\dot{y}^2 &= E_{mfg0} - W_{mfg} - \left(m_2 + \frac{2I}{r^2} + 2m_6\right)\dot{s}_2^2 + k_3d_0^2 \\ &= C(t) \end{aligned} \quad (3.63)$$

Here, y is the elongation of the MFG spring from its virtual free length and d_0 is the virtual elongation at the free length defined in Section 2.3.1. Recall that these variables are used to generalize the methods such that springs with initial tension are also included. For other types of springs (compression springs and the extension springs without initial tension) the variable y is equal to the elongation of the spring from its free length, and $d_0 = 0$. The constant coefficients A and B are defined in equation (2.23). The E_{mfg0} is the initial energy of the MFG at time $t = t_0$.

Since the variable s_2 is periodic within the period T , each arbitrary position s_2 must exist $2n$ times within the period T , where $2n$ corresponds to the number of occurrences of an arbitrary value of s_2 in the period. Note that the number of occurrences of two arbitrary values of s_2 might be different. In Figure 3.7, the number of occurrences of an arbitrarily selected value of an arbitrary s_2 function with period T is shown. As can be seen from the figure, number of occurrences of the selected point is four.

The time corresponding to consecutive occurrences of a selected arbitrary value of s_2 are named as pass and return times. Note that n corresponds the number of passes, or

returns. Note also that the velocities at the pass times have the same sign. Similarly, the velocities at the return times also have the same sign. The signs for the pass and the return times, on the other hand, must be different.

In Figure 3.7 t^* denotes a time value which corresponds to a local extremum of s_2 , i.e., $\dot{s}_2(t^*) = 0$. The variable t^* will be used later in this section to determine the condition to obtain open slot profile.

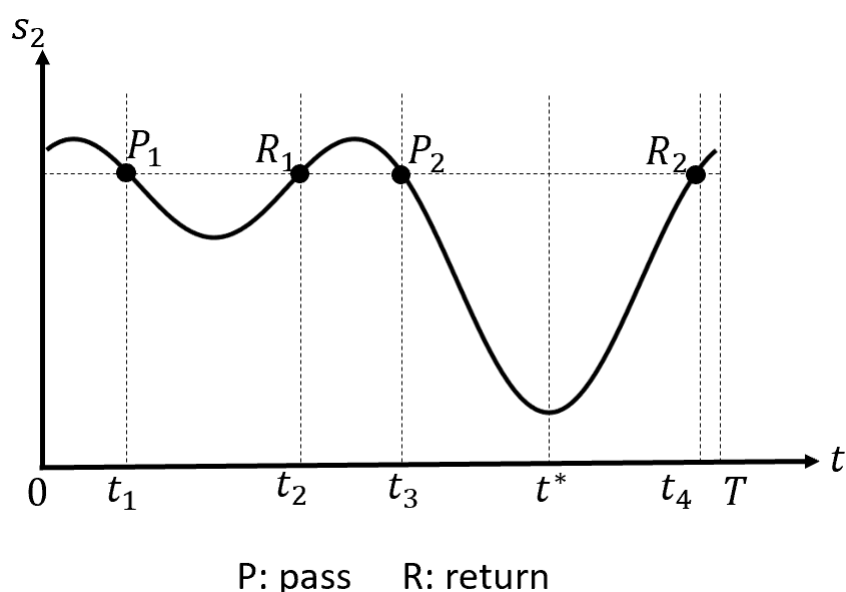


Figure 3.7. The pass and return times for arbitrary periodic s_2 variable

Note that for an arbitrary s_2 value within one period, the following relation can be obtained

$$s_2(t_1) = s_2(t_2) = \dots = s_2(t_{2n}) \tag{3.64}$$

$$t_i \in [0, T], i \in 1, 2, \dots, 2n$$

where n is the number of passes corresponding to the arbitrary point.

Recall from the definition of the open slot profile that s_3 is a single valued function of s_2 . Hence, it follows that

$$\begin{aligned} s_3(t_1) = s_3(t_2) = \dots = s_3(t_{2n}) \\ t_i \in [0, T], i \in 1, 2, \dots, 2n \end{aligned} \quad (3.65)$$

Since the relation between s_3 and y is linear (see equation (2.17)), it also follows that

$$\begin{aligned} y(t_1) = y(t_2) = \dots = y(t_{2n}) \\ t_i \in [0, T], i \in 1, 2, \dots, 2n \end{aligned} \quad (3.66)$$

The kinematic relation between velocity \dot{s}_2 and y can be obtained by inserting (2.18) into (1.26) to get

$$\dot{y} = p\dot{s}_2 \quad (3.67)$$

where p is defined as the slope of the roller slot profile contact point shown in Figure 1.2. It is clear that, for open slot profiles, p is also single valued function of s_2 . Hence,

$$\begin{aligned} p(t_1) = p(t_2) = \dots = p(t_{2n}) \\ t_i \in [0, T], i \in 1, 2, \dots, 2n \end{aligned} \quad (3.68)$$

Now, for two arbitrary time of occurrences (t_i and t_j) of an arbitrary s_2 value that are satisfying the equality of

$$\begin{aligned} s_2(t_i) = s_2(t_j) \\ t_i, t_j \in [0, T], i, j \in 1, 2, \dots, 2n \end{aligned} \quad (3.69)$$

Substitute \dot{y} in equation (3.67) into (3.63) for $t = t_i$ to get

$$\begin{aligned} Ay(t_i)^2 + B \left\{ Bp(t_i)^2 + m_2 + \frac{2I}{r^2} + 2m_6 \right\} \dot{s}_2(t_i)^2 \\ = E_{mfg0} - W_{mfg}(t_i) + k_3 d_0^2 \\ t_i \in [0, T], i \in 1, 2, \dots, 2n \end{aligned} \quad (3.70)$$

By subtracting equation (3.70) for $t = t_i$ and $t = t_j$ the following equation is obtained.

$$\begin{aligned}
& -W_{mfg}(t_i) + W_{mfg}(t_j) \\
& = \left\{ Bp(t_i)^2 + m_2 + \frac{2I}{r^2} + 2m_6 \right\} \left\{ \dot{s}_2(t_i)^2 - \dot{s}_2(t_j)^2 \right\} \quad (3.71) \\
& t_i, t_j \in [0, T], i, j \in 1, 2, \dots, 2n
\end{aligned}$$

If equation (3.71) holds for all t_i and t_j occurrences of all s_2 values in a period, then one obtains open an slot profile. This equation holds for all open slot profiles. Therefore, equation (3.71) is a necessary and sufficient condition to obtain MFGs with open slot profile. However, one needs to obtain all times of occurrences of every s_2 value within the period. Obtaining these time values may be difficult depending on the variation of s_2 with respect to time. However, one can see that if the magnitudes of the velocity \dot{s}_2 at the time t_i and t_j are the same, i.e.,

$$|\dot{s}(t_i)| = |\dot{s}(t_j)| \quad (3.72)$$

then, the right-hand side of equation (3.71) becomes zero for open slot profiles. Hence, left-hand side of equation (3.71) must also be zero, i.e.,

$$W_{mfg}(t_i) - W_{mfg}(t_j) = 0 \quad (3.73)$$

for all values of t_i and t_j . Equation (3.73) holds for all open slot profiles satisfying equation (3.72). If equation (3.73) does not hold, no conclusions can be made about the slot profile type. Recalling the condition given in equation (3.69), if $|\dot{s}_2|$ is a single valued function of s_2 , then equation (3.72) holds for all time occurrences of every s_2 value. Hence, obtaining only two occurrences of each s_2 value is sufficient for checking equation (3.73) (to determine if slot profile type is open). In order to obtain these times, one may use the time of any extremum point of the variable s_2 . See Figure 3.7 for a t^* .

If equations (3.64) and (3.72) hold, then one must have

$$\dot{s}_2(t^* - t) = -\dot{s}_2(t^* + t) \quad (3.74)$$

i.e., \dot{s}_2 must be symmetrical with respect to the vertical line passing through $t = t^*$. Therefore, by integrating \dot{s}_2 to the right and to the left from the reference time t^* , one obtains the same position, i.e.,

$$\int_{t^*}^{t^*-t} \dot{s}_2 dt = \int_{t^*}^{t^*+t} \dot{s}_2 dt \quad (3.75)$$

leading to

$$s_2(t^* - t) = s_2(t^* + t) \quad (3.76)$$

Hence, the two variables t_i and t_j , that satisfy equation (3.69) is obtained as a function of time. Now, define t_- and t_+ via the equations

$$\begin{aligned} t_- &= (t^* - t) \text{ mod } T \\ t_+ &= (t^* + t) \text{ mod } T \end{aligned} \quad (3.77)$$

Since these values are defined within the period, the modulo operator is used in equation (3.77).

Hence, by inserting t_- and t_+ in equation (3.77) into equation (3.73), the condition for W_{mfg} to have an MFG with open slot profile is obtained as follows

$$W_{mfg}(t_-) - W_{mfg}(t_+) = 0 \quad (3.78)$$

Equation (3.78) implies that W_{mfg} is required to be symmetric about the reference time t^* , such that $W_{mfg}(t^* + t)$ is an even function [14].

To sum it up, there are two conditions to determine if the MFG design will have an open slot profile. The first condition is that the magnitude of link 2 velocity ($|\dot{s}_2|$) should be a single-valued function of link 2 position (s_2). This can be determined by observing the plot $|\dot{s}_2|$ vs s_2 . The second condition is that equation (3.78) holds for all time values $0 \leq t < T$. If one has discrete values of the W_{mfg} , then one can plot the difference and observe that the result is zero.

If (3.78) is not satisfied but $|\dot{s}_2|$ vs s_2 plot is single-valued, then, a method to modify the given W_{mfg} to obtain an open slot profile is introduced in next section.

3.4.2. Conversion to Open Profiles

This method symmetrizes an arbitrary W_{mfg} variation around t^* such that the symmetry condition given by equation (3.78) is satisfied. The guideline for this modification is described in the next subsection.

3.4.2.1. Design Guideline

The steps of the algorithm, which modifies a given MFG energy profile, W_{mfg} , such that one obtains an open slot profile, is given below.

1. Confirm that $|\dot{s}_2|$ vs s_2 plot is single-valued for all values of s_2 within the period T . If it is not single-valued, then quit the algorithm. One may design the MFG by using the methods given in Chapter 2, and see if the result is an open slot profile.
2. Check if (3.78) holds by plotting the $W_{mfg}(t_-) - W_{mfg}(t_+)$ versus time plot and see that the plot is identically zero for all time values. If it is, then the profile will already lead to an open slot profile. If it is not, continue with step 3 to modify W_{mfg} to obtain open slot profile.
3. Confirm that the motion is one-pass-one-return type as will be explained in 3.4.2.2. If this condition is not satisfied, then stop the iteration. Design MFG physically to see if it leads to an open slot profile.
4. Obtain W_{mfg} (disregarding its resultant slot shape) by using the guideline in Section 3.3.1
5. Calculate $W_{mfg,even}$ using the method given in 3.4.2.3.
6. Apply the correction algorithms given in Sections 3.3.4 and 3.3.5 if there are asymptotic discontinuities related to F_{mfg} that is calculated by using $W_{mfg,even}$.

7. Calculate the open slot type performance measures using Section 3.3.2.

3.4.2.2. One-Pass-One-Return Condition for Link 2 Motion

By observing the s_2 versus time plot, one can confirm the one pass-one return condition. In order for this condition to hold, any arbitrary position should exist only twice in one period, such that there is one pass and one return time for all s_2 values in the period. This is demonstrated in Figure 3.8 with three arbitrary s_2 values. Note that the s_2 vs t plot given in Figure 3.7 is not one pass one return type.

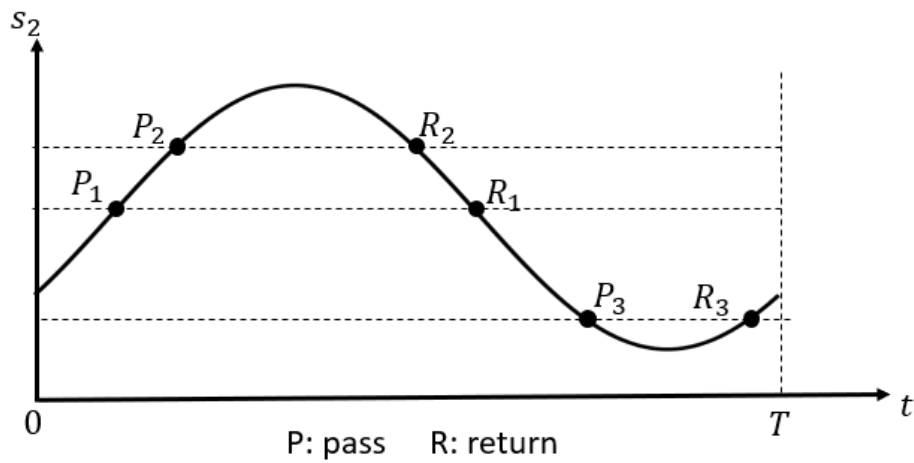


Figure 3.8. Demonstration of one pass one return type motion

3.4.2.3. Symmetrizing the Energy Profile

Symmetrization is done analogous to dividing signals to even and odd parts [14]. Let $f(t)$ be a function of t , the even ($f_e(t)$) and odd ($f_o(t)$) parts of the signal can be found by the following formula.

$$f(t) = f_e(t) + f_o(t) \quad (3.79)$$

$$f_e(t) = \frac{1}{2}(f(t) + f(-t)) \quad (3.80)$$

$$f_o(t) = \frac{1}{2}(f(t) - f(-t)) \quad (3.81)$$

In this case, it is desired to symmetrize W_{mfg} around the time t^* where $\dot{s}_2(t^*) = 0$. Therefore, one can use the following equations to get the even and odd parts of the work done by the MFG.

$$W_{mfg,even}(t^* + t) = \frac{1}{2}(W_{mfg}(t^* + t) + W_{mfg}(t^* - t)) \quad (3.82)$$

$$W_{mfg,odd}(t^* + t) = \frac{1}{2}(W_{mfg}(t^* + t) - W_{mfg}(t^* - t)) \quad (3.83)$$

$W_{mfg,even}(t^* + t)$, is the even part of $W_{mfg}(t + t^*)$ and $W_{mfg,odd}(t^* + t)$ is the odd part such that their sum is equal to $W_{mfg}(t^* + t)$. After obtaining the even part in equation (3.82), time-shift it by the amount t^* to obtain $W_{mfg,even}(t)$.

Since only the even part satisfies the condition by equation (3.78), the odd part cannot be used in the open profile design. Open profile is obtained by using $W_{mfg,even}(t)$ as the work done by the MFG, i.e., $W_{mfg}(t)$ is approximated by $W_{mfg,even}(t)$. However, the MFG force output obtained by using $W_{mfg,even}(t)$ is not optimum, and it is not guaranteed to improve the performance of mechanism. Therefore, the performance improvement by using $W_{mfg,even}(t)$ should be obtained by calculating the performance indices given in Section 3.3.2.

The symmetrization may cause zero-crossing problems again. Therefore, one might need to use zero speed crossing compensation and energy drift compensation methods after the symmetrization.

It should be noted that it is also possible to determine an even W_{mfg} variation which approximates the given non-even variation in an optimal manner such that the difference of the performances between the non-even W_{mfg} profile and the even W_{mfg} profile is minimum.

3.5. Application of the Methods

In this section, the optimization algorithms and modification algorithm proposed for W_{mfg} are demonstrated. The slider-crank example (Task-A) in [4] is used, to compare the performance improvement with the previous studies.

The reasons for selecting Task-A are listed below.

- Inertial forces are negligibly small compared to the load forces
- The task-A is convertible to the open slot profile with the method given in the Section 3.4.2

3.5.1. Description of the Machine and the Load Force

In Task-A, the slider-crank is used as a servo press. The external force acting on the slider is shown in Figure 3.9.

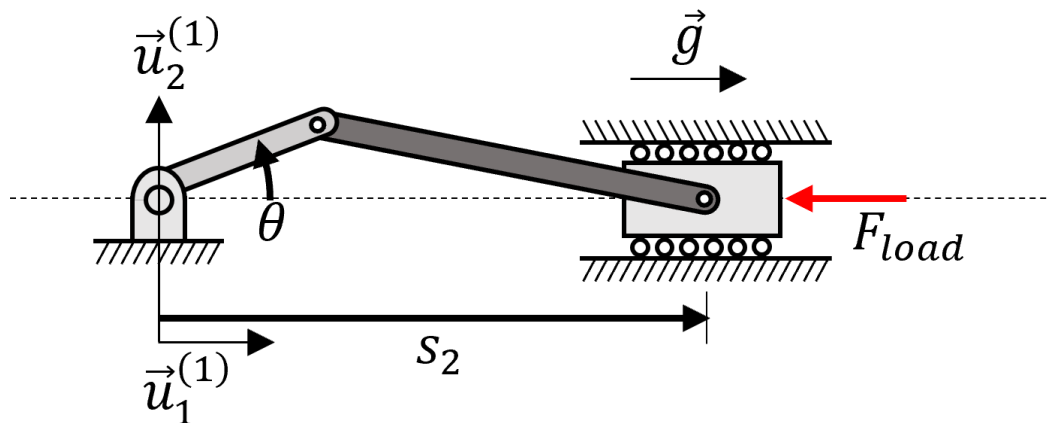


Figure 3.9. Sketch of the slider-crank mechanism

As shown in the figure, F_{load} is the external force applied on the mechanism, which is parallel to the unit vector $-\vec{u}_1^{(1)}$.

The specifications of the machine are given in Table 3.2.

Table 3.2. Specifications of the machine in [4]

Specification	Value	Symbol
Crank length	: 128.5 mm	l_{crank}
Coupler length	: 771 mm	$l_{coupler}$
Forging stroke	: 34.5 mm	s_f
Crank angular speed	: 60 rpm (Constant)	ω
Initial crank angle	: 180 degrees	θ

The maximum stroke (s_{2max}) is defined via the equation below.

$$s_{2max} = l_{crank} + l_{coupler} \quad (3.84)$$

The compression distance (s_c) is defined via the equation below.

$$s_c = s_f - (s_{2max} - s_2) \quad (3.85)$$

The machine starts pressing the object when the compression distance is positive. The pressing task is complete when the slider reaches to the maximum stroke. During the return, no force is applied on the machine.

The loading force vs time is given in [4] (with respect to the compression distance (s_c)) is given in equation (3.86).

$$F_{load} = \begin{cases} 2.8 \cdot 10^6 \frac{s_c}{29} & \text{if } 0 \leq s_c < 29\text{mm}, \text{ and } \dot{s} \geq 0 \\ \left(2.8 + 13.2 \frac{s_c - 29}{5.5}\right) \cdot 10^6 & \text{if } 29\text{mm} < s_c < 34.5\text{mm}, \text{ and } \dot{s} \geq 0 \\ 0 & \text{otherwise} \end{cases} \quad (3.86)$$

The load force vs compression distance plot is given in Figure 3.10.

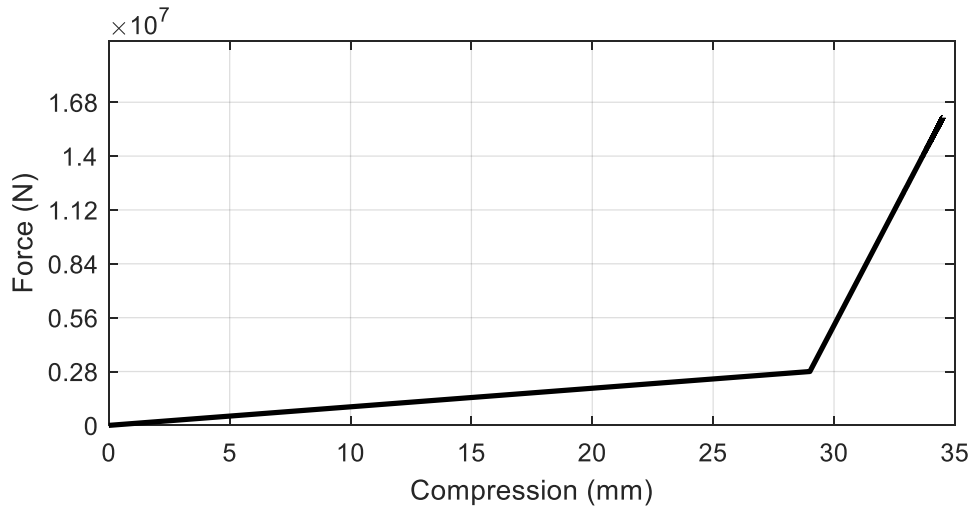


Figure 3.10. Force vs compression distance plot

Since mass and inertia of the links are not available in [4], the mechanical energy of the machine is neglected. Recall that the task force (F_{task}) was defined to be the force which drives the machine from its output link. Hence, neglecting the inertial and gravitational forces, one obtains

$$F_{task} = -F_{load} \quad (3.87)$$

Using dynamic analysis, the required motor torque (T_{task}) is found. One may refer to the [4] for the kinematic and dynamic analysis.

Torque (T_{task}) vs time plot is given in Figure 3.11. For convenience, the task force, the slider velocity and the task power when the MFG is not connected is given in Figure 3.12. Recall that the task power was defined as the power that the motor would spend if the MFG is not connected.

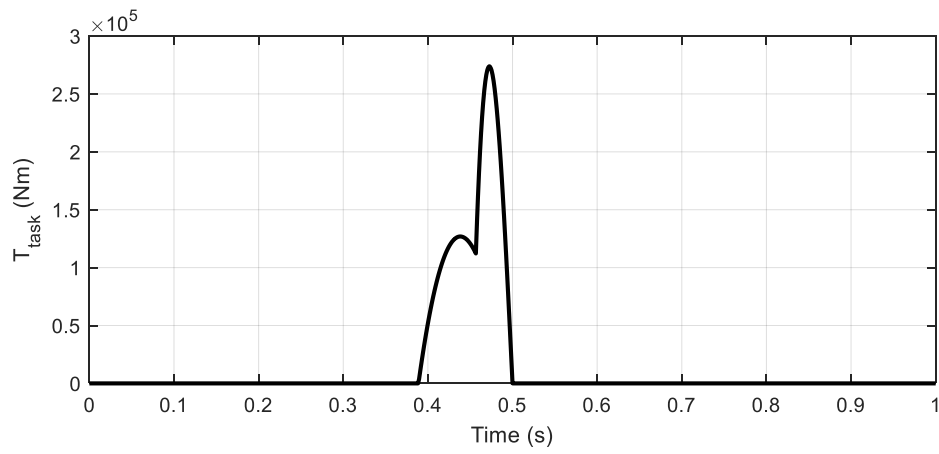


Figure 3.11. Motor torque vs time plot

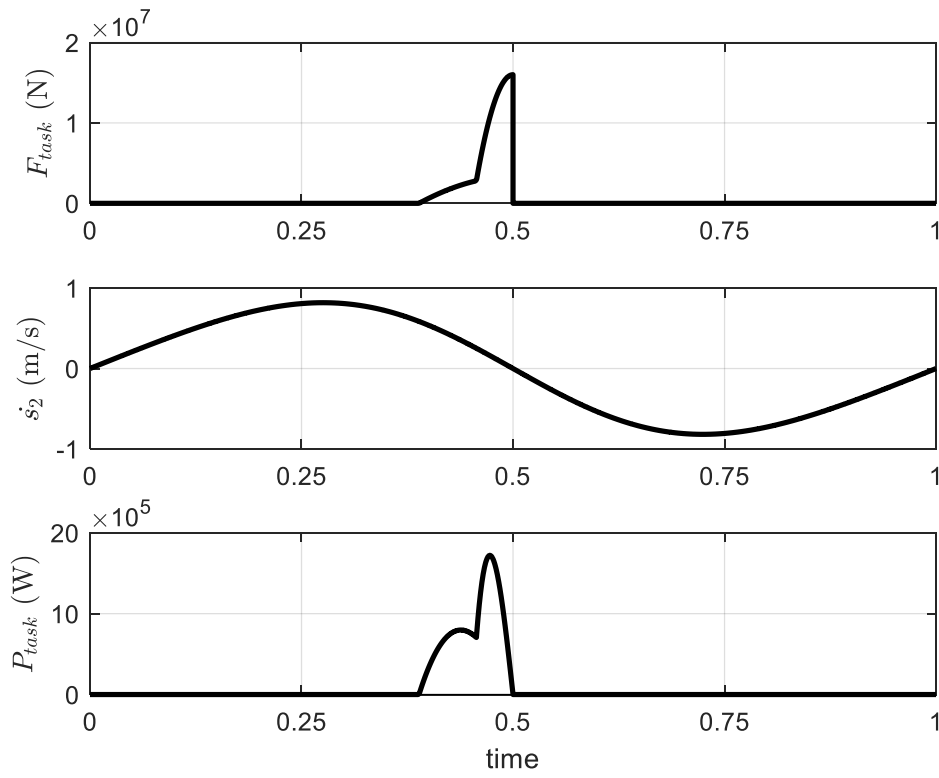


Figure 3.12. Task force, slider velocity and task power vs time plot

3.5.2. MFG Power Design for the Machine

In this section, in order to obtain the MFG power variation, the methods proposed in the previous sections are applied. W_{mfg} is modified such that, an open slot profile is obtained.

3.5.2.1. Application of the Optimization Methods

Note that, the crank angular speed is constant. Thus, for all of the three optimization methods given in Section 3.3.3, the optimum motor power (P_{motor}^*) turns out to be the same expression (see equations (3.33), (3.45) and (3.60)).

P_{motor}^* is obtained from equation (3.33). The optimum MFG power (P_{mfg}^*) is obtained from equation (3.34).

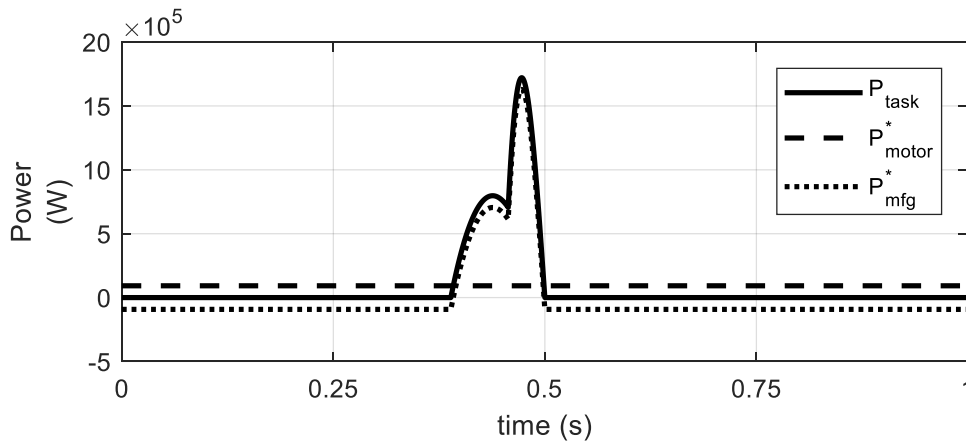


Figure 3.13. Task, optimum motor, and optimum MFG powers vs time plot

P_{mfg}^* and P_{motor}^* plots are given in Figure 3.13 and compared with P_{task} which is the power output of the motor when the MFG is not applied. The variable P_{task} is calculated by using equations (3.9) and (3.87). Note that the optimum motor power is set to the average power. Note also that the maximum power is reduced to a great

extent. The minimum values of the performance measures corresponding to the minimization algorithms defined in Section 3.3.2 are given in Table 3.3.

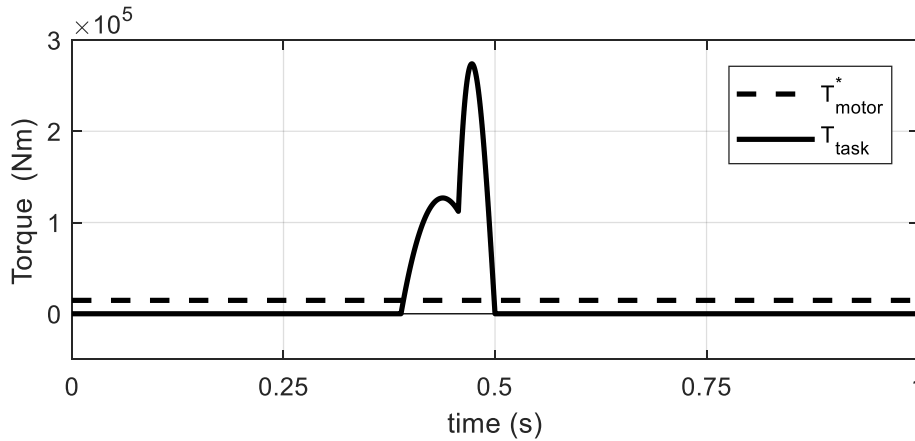


Figure 3.14. Optimum motor torque and the task torque vs time plot

The optimum motor torque after the optimization is given in Figure 3.14 and compared to the task torque which is the motor torque when MFG is not connected.

Recall that the optimization algorithms do not take into account the MFG power constraint given by equation (1.42). Therefore, asymptotic discontinuities occur when $\dot{s}_2 = 0$. The optimum MFG force and the task force is given in. As expected, asymptotic discontinuities are observed. Note that the critical times in the figure are, $t_{cr1} = 0$ s, $t_{cr2} = 0.5$ s and $t_{cr3} = 1$ s. The discontinuities are approximated in the next section in order to obtain a physically feasible MFG.

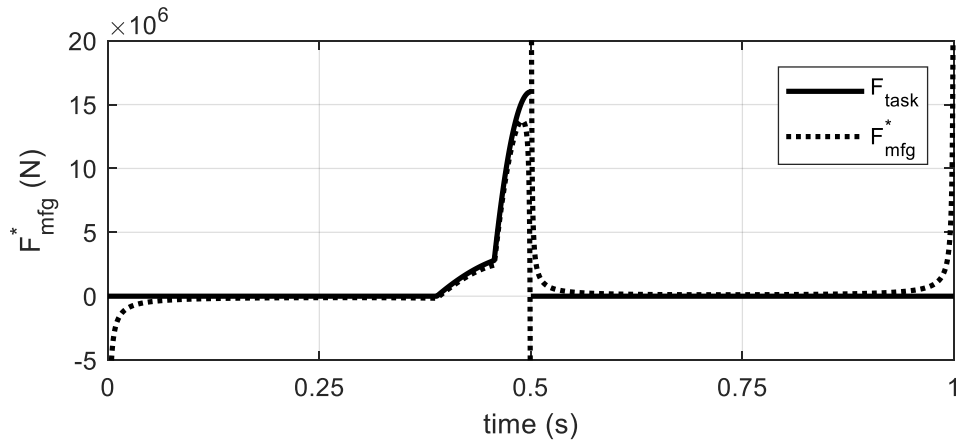


Figure 3.15. Asymptotic discontinuities of the optimum MFG force

The optimization algorithms take the first constraint of the MFG power, given by equation (1.41), into account such that work done by the optimum MFG power is conservative. This is demonstrated in Figure 3.16. In the figure, work done by the original mechanism when the MFG is not applied (W_{task}), work done by the optimum motor torque (W_{motor}^*) are also given. The variables W_{task} and W_{motor}^* are obtained by integrating the power variables P_{task} and the P_{motor}^* .

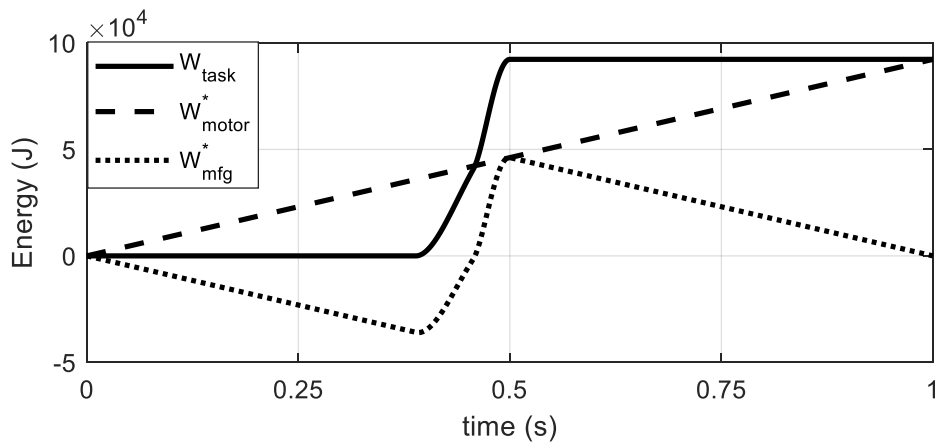


Figure 3.16. Work done by the original mechanism (W_{task}), work done by the optimum motor torque and work done by the optimum MFG force (W_{mfg}^*) vs time plot

Table 3.3. Minimum values of the performance measures for the optimization algorithms

Minimize max power: J_P	Minimize max torque: J_T	Minimize total energy: J_E
0.053629	0.053629	0.085438

3.5.2.2. Application of the Zero Crossing Compensation Method

The asymptotic discontinuities shown in Figure 3.15 will now be approximated by using the method discussed in Section 3.3.4. Recall that the critical times where $\dot{s}_2 = 0$ are $t_{cr1} = 0$ s, $t_{cr2} = 0.5$ s and $t_{cr3} = 1$ s. The specified time is selected as $t_{sp} = 0.025$ s. The approximated curves for t_{cr1} and t_{cr2} are given in Figure 3.17. The approximation curve for t_{cr1} is given on the left. The curve for t_{cr3} is not given since it is symmetric with the curve corresponding to the critical time t_{cr1} . Note the approximated curve is labelled as F'_{mfg} .

It has been stated that this approximation deviates the MFG force slightly. Therefore, the work done by the approximated MFG force at the end of the period is not zero. The deviation is shown in Figure 3.18. The approximated motor power (P'_{motor}) and motor torque (T'_{motor}) are compared with P_{motor} and T_{motor} after the application of the drift compensation algorithm in the next section.

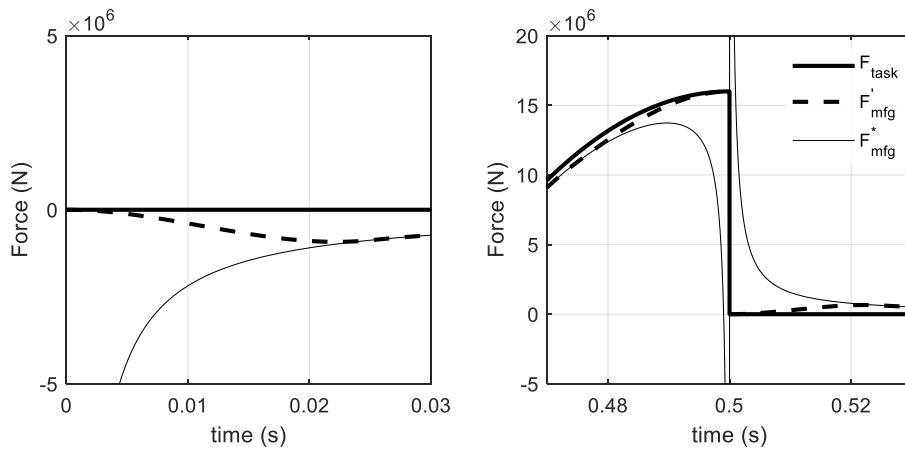


Figure 3.17. Approximation of the asymptotic discontinuities for the critical times t_{cr1} and t_{cr2}

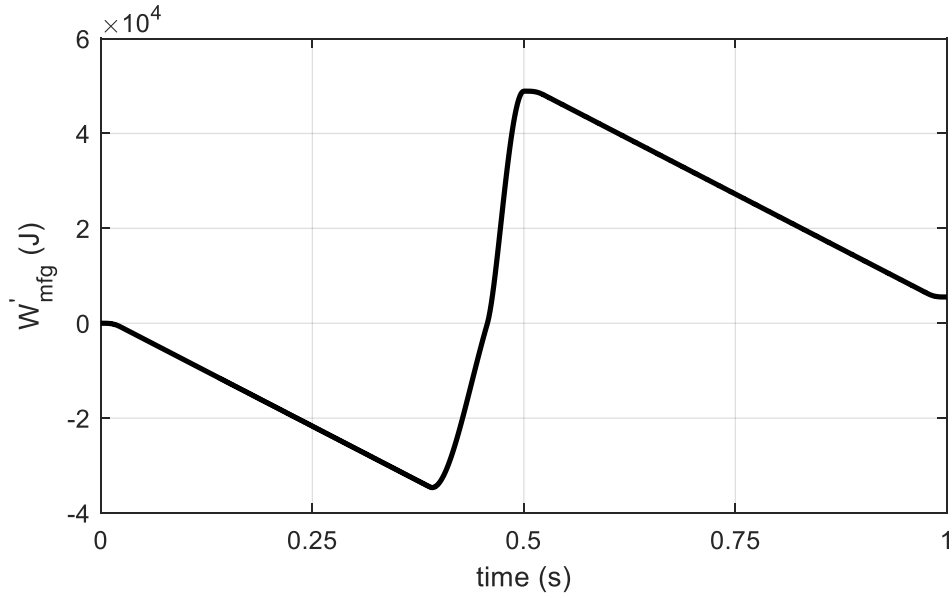


Figure 3.18. The deviation from the conservative work

3.5.2.3. Application of the Energy Drift Compensation

Recall that by multiplying P'_{motor} with a constant, the work done by the MFG during one period is made zero in Section 3.3.5. Noting that F'_{mfg} and \dot{s}_2 are available, the variables P'_{mfg} , P'_{motor} and T'_{motor} are calculated by using equations (3.11), (3.8) and (3.13) respectively.

Using equation (3.61), P_{motor} is obtained. Motor power and motor torque obtained from the zero-crossing and energy drift compensation algorithms are given in Figure 3.19. Since the plots are close to each other, on the right, the plots are zoomed around $t = 0.5s$. Note that the values approach to zero at the critical point $t_{cr2} = 0.5s$.

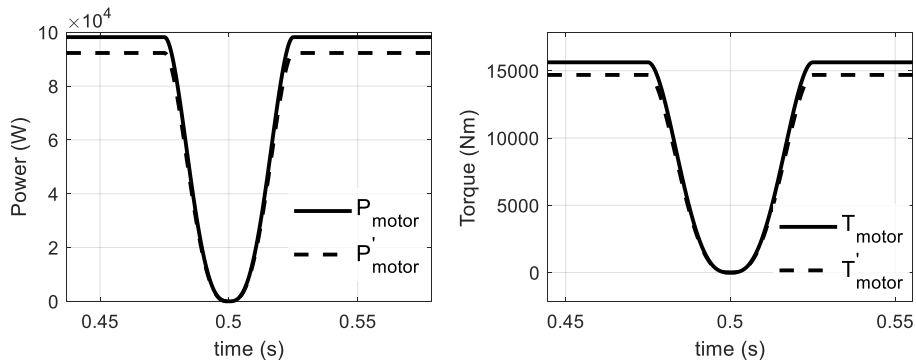


Figure 3.19. The energy drift compensation at t_{cr2}

The plot of the output variables (T_{motor} , F_{mfg} , P_{motor} , W_{mfg}) of the MFG Power design are given in Figure 3.20.

3.5.2.4. Performance Comparison with the Previous Method

The performance measures of the MFG power design are given in Table 3.4. Note that the reduction in the performance caused by the application of the compensation algorithms is small as can be seen from the table.

Table 3.4. Performance measures of the MFG power design

	Minimize max power: J_P	Minimize max torque: J_T	Minimize copper loss: J_E
Optimum:	0.053629	0.053629	0.085438
After Compensation Algorithms:	0.057054	0.057054	0.0898
Reduction in performance:	0.0034	0.0034	0.0044

In [4], the minimum values of the performance measures for minimizing maximum power and minimizing total energy consumption are given. The measure for minimizing the maximum power used in [4] is the same with the measure value used in this study.

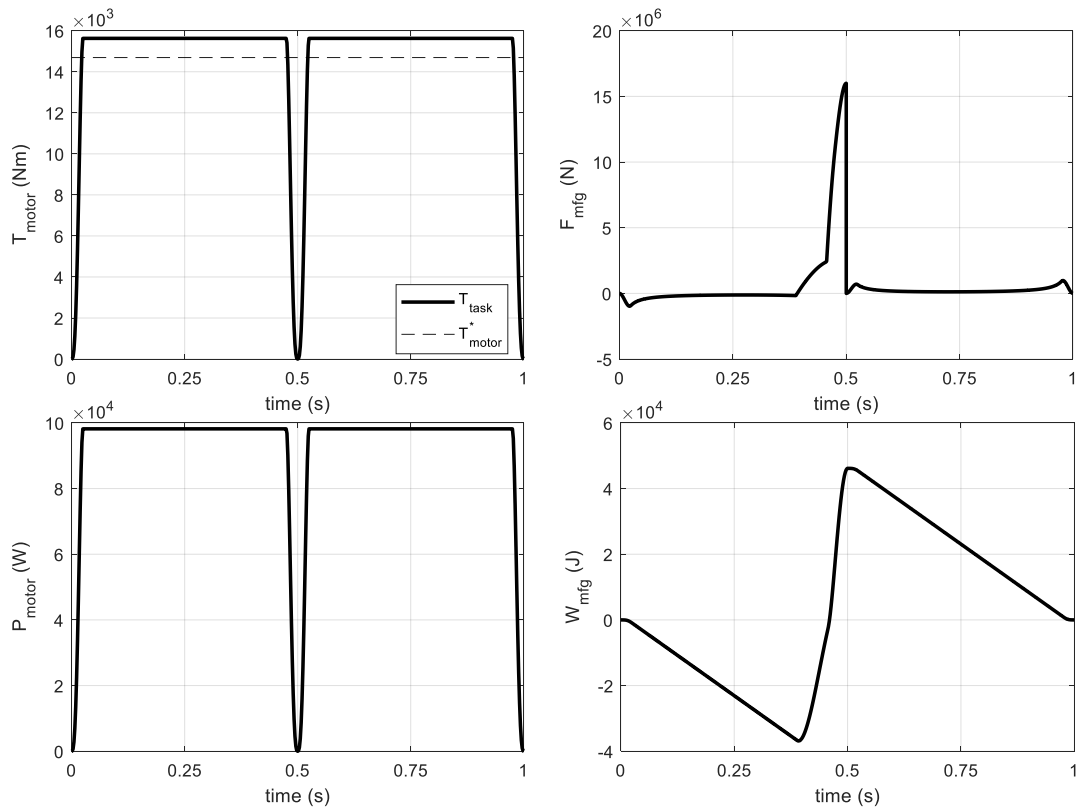


Figure 3.20. Output variables of the MFG power design (T_{motor} , F_{mfg} , P_{motor} , W_{mfg})

The best J_P obtained in [4] is $J_P = 0.3989$. This value is obtained by using a 7th order Fourier series to approximate F_{mfg} in order to minimize the maximum power. The results of both studies are given in Table 3.5.

Table 3.5. Minimum values of J_P

J_P in this study	J_P in [4]
0.057054	0.3989

It should be noted that while using the method proposed in [4], if the order of the Fourier series (used to express F_{mfg}) is increased, one will obtain better results (i.e., the minimum of J_P will decrease). It should be also noted that the method proposed in

[4] does not, ever, lead to vertical asymptotes in F_{mfg} . Hence, the F_{mfg} obtained via the method proposed in [4] will not involve sudden changes.

The performance measure used for minimizing the energy consumption in [4], in terms of the notation used in this study, is given by ξ_E where it is calculated by the following equation.

$$\xi_E = \frac{\int_0^T (P_{motor} + K^* T_{motor}^2) dt}{\int_0^T (P_{task} + K^* T_{task}^2) dt} \quad (3.88)$$

where the value of K^* used for the 1.61 MW motor in [4] is given by

$$K^* = 1.0299 \cdot 10^{-6} \frac{A^2 \cdot \Omega}{Nm^2} \quad (3.89)$$

In [4], the efficiencies for different types of braking methods, discussed in Section 3.2.2.2, are compared. Note that P_{motor} is always positive in this study. Thus, the performance is not affected by the braking type. The minimum values of the performance measures for minimizing the total energy consumption are compared in Table 3.6. The results of a regenerative motor with 90% efficiency and 7th order Fourier series approximation in [4] is given in the table.

Table 3.6. Minimum values of ξ_E which minimizes the total energy consumption

ξ_E in this study	ξ_E in [4]
0.97506	0.9894

3.5.2.5. Slot Profile of the Design

The plot of spring length, y , vs link 2 position, s_2 , is given in Figure 3.21. If one neglects the inertia forces, the slot profile will be similar to the curve given in the figure. To obtain the figure, the spring coefficient is taken as 1000 N/mm and equation

(2.31) is used. The spring is assumed to be an extension spring without initial tension. Therefore, y is equal to the deformation of the spring from its free length.

3.5.3. Conversion of the Design to Open Slot Profile

In this section, the guideline in Section 3.4.2.1 is applied to convert the closed profile to an open profile. In the first step, the $|\dot{s}_2|$ vs s_2 plot is obtained to determine if $|\dot{s}_2|$ is a single valued function of s_2 . The result is given in the left plot of Figure 3.22. As can be seen from the figure, $|\dot{s}_2|$ is single valued.

In the second step, the symmetricity of W_{mfg} is checked by plotting the time function non the left-hand side of equation (3.78) and (see the plot on the right of Figure 3.22). Since the time function is not equal to zero for all time values in one period, one proceeds with the third step.

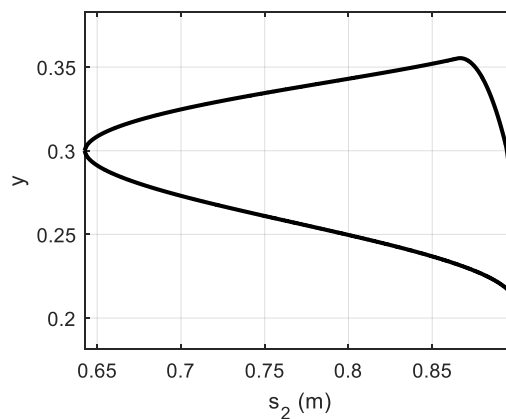


Figure 3.21. Spring elongation vs slider position

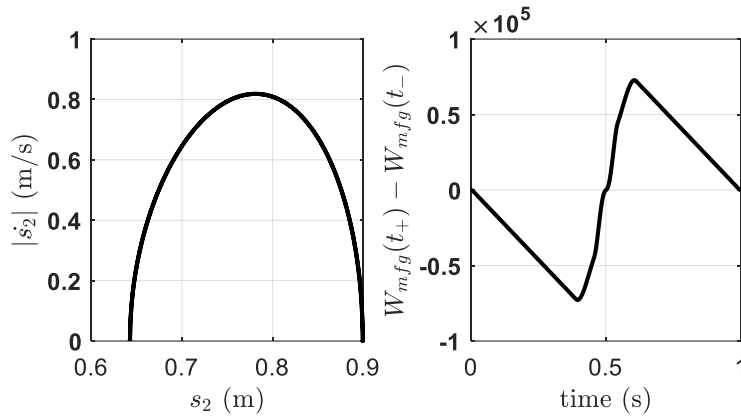


Figure 3.22. Open slot profile check results

In the third step, W_{mfg} is symmetrized by using equation (3.82). The even and odd parts of W_{mfg} are shown in Figure 3.23. Note that since $\dot{s}_2 = 0$ at $t = 0$, as can be seen from Figure 3.12, $t^* = 0$.

By taking time derivative of $W_{mfgEven}(t)$, the power output of the MFG (P_{mfg}) is obtained. P_{motor} can then be obtained by inserting P_{mfg} into equation (3.8). F_{mfg} and T_{motor} are then found by using equations (3.12) and (3.13) respectively. The results are given in Figure 3.24. Note that in the figure MFG applies half of the force required during the compression and retrieves the power back from the motor after the compression is finished.

The performance measures for the open slot profile MFG are given in Table 3.7. Note that all performance measures are 0.5. The results agree with the observations from Figure 3.24. It can also be seen that the performance of the MFG is reduced, as expected, when an open slot profile is utilized.

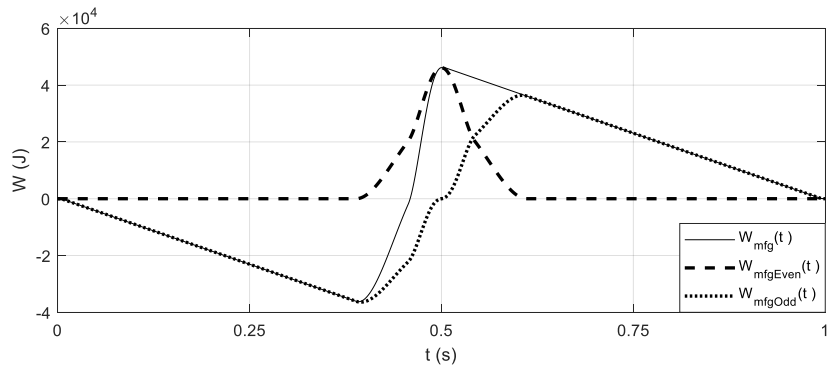


Figure 3.23. Even and odd functions of the W_{mfg}

Table 3.7. Performance measures for open slot profile MFG design

Minimize max power: J_P	Minimize max torque: J_T	Minimize copper loss: J_E
0.5	0.5	0.5

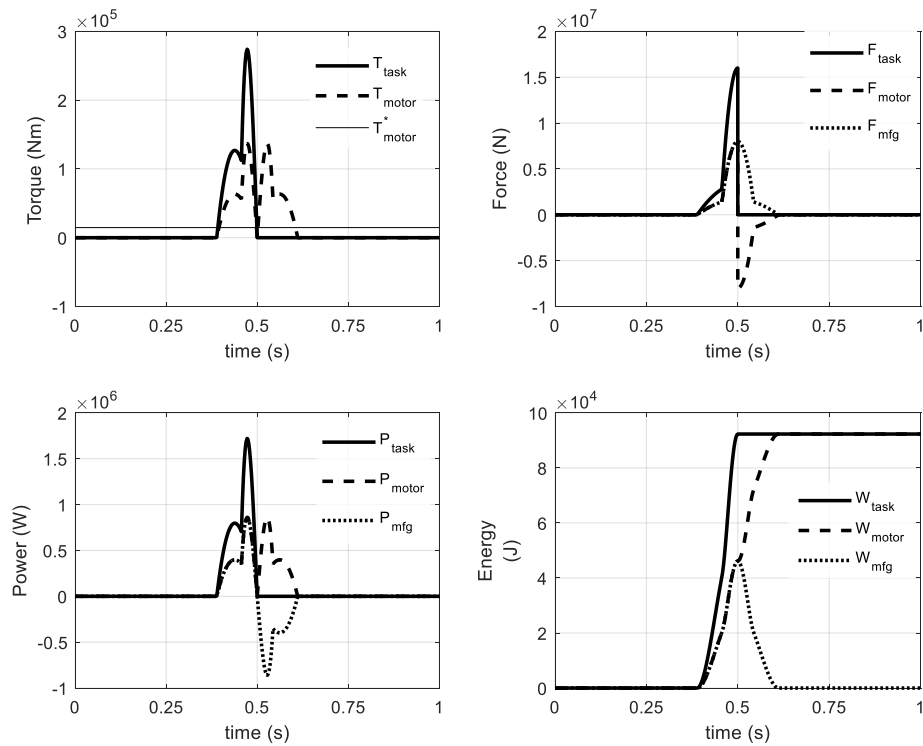


Figure 3.24. Results of open slot profile conversion

3.5.3.1. Slot Profile of the Design

In the design, the same spring in Section 3.5.2.5 is used. The spring elongation, y , vs link 2 position, s_2 , plot is given in Figure 3.25. Note that the curve shown in the figure is similar to the path that the center of the roller follows on link 3 (since y and s_3 are linearly related).

3.6. Discussion of Results

The optimum MFG power variations have been designed in this chapter for three different performance measures. It has been found that if the motor angular velocity is constant, the optimum MFG power variation is identical for all cases.

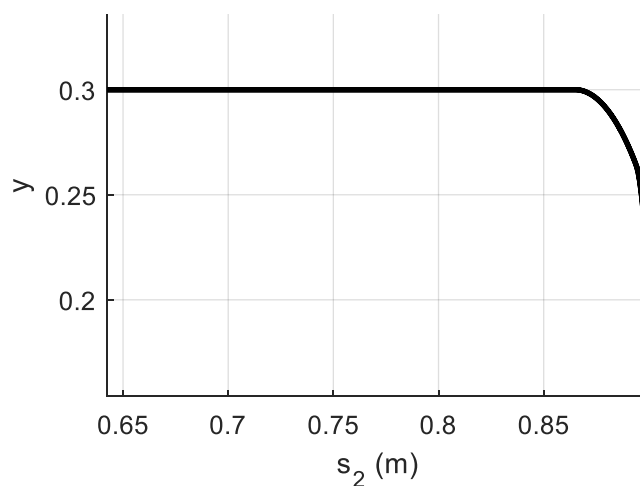


Figure 3.25. Spring elongation vs slider position (similar to the path that the center of the roller follows on link 3)

For this case study, it has been observed that the motor power is always positive for all three performance measures. Thus, the motor never needs to brake. Therefore, it is

not necessary to use dynamic or regenerative braking. Hence, one can use cheaper motors.

In addition, it has been shown that the maximum power and energy required for the task can be reduced extensively. Thus, the energy cost for an application may be greatly reduced. Also, by minimizing the maximum torque required, smaller, thus cheaper, motors can be used for the same application.

In the case study considered, it has been observed that the difference between the performance measures for optimum and corrected cases is low. Thus, the corrected performance measures are close to the best possible performance.

The approach proposed in this study has been compared with the approach proposed in [4]. Although, in the previously proposed method [4], one may use higher degree Fourier series to obtain better results, the cost of the computation increases. However, the method proposed in this study is computationally light. One drawback of the method proposed in this study is that the optimization of different measures is not possible without modifying the algorithms. For example, one may not minimize the normal forces acting on the machine links without modifying the algorithms. Minimizing a combination of different performance measures is also not possible without further modifications.

CHAPTER 4

MATHEMATICAL CASE STUDY

4.1. Introduction

In this chapter, mathematical analysis of a machine (for performance improvement) by using an MFG is realized. In the first part, the mathematical model of the machine and the loads on the machine are discussed. A symmetrical slider-crank is used as the machine. A spring is placed between two sliders of the machine in order to simulate a load with conservative force. The inertial forces and the frictional forces on the slider links (Links 2 & 4) are modeled.

The results of this mathematical study will be compared with the results of an actual experimental case study. Since already available components are used from the previous experiments realized in [3], some of the design parameters are already set (i.e., they cannot be changed).

Using the optimum MFG power profile, slot profile links are designed using the methods discussed in Chapter 2. In order to demonstrate the effect of the preloads, two cases, with different preloads, are compared. In the first case, the minimum preloaded spring length is selected according to equation (2.28). In the second case, the spring length to be used in the experiment is selected. Normal forces acting on the roller/slot profile contacts and the mass of the slot profiles for these two cases are compared.

4.2. Description of the Machine

The sketch of the symmetrical slider-crank mechanism is shown in Figure 4.1.

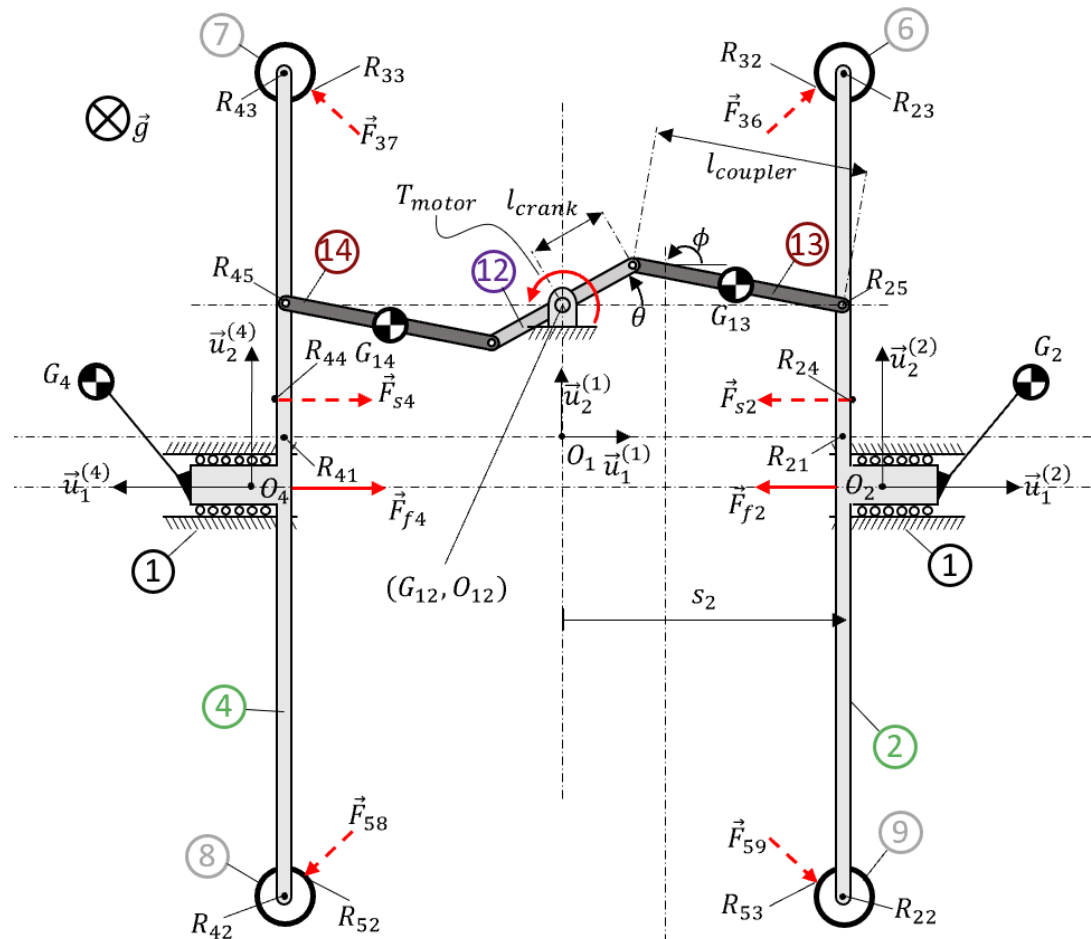


Figure 4.1. Sketch of the symmetrical slider-crank mechanism, with link numbers, external forces applied on the mechanism (optional force vectors are given with dashed arrows), reference points and reference frames

A schematic of the machine is given in Figure 4.1. The link numbers of the machine are shown with the balloon annotation in the figure. Link numbers 3, 5, 10 and 11 (see figure A.1) are reserved for the MFG links and are not shown in Figure 4.1. The links, the direction and point of application of the forces in the sketch are drawn as close as possible to the physically implemented mechanism.

4.2.1. Description of Shared Links of the Machine with MFG

Links 2 and 4 are the original links used in the experimental setup built [3]. These links were used as the MFG input links (links 2&4) and coupled to slider links of two identical slider-crank mechanisms. In this study, these links also act as the slider link of the machine. Since they are shared by the MFG and the mechanism, the frictional and inertial forces acting on these links are considered. Therefore, in the MFG design, masses of these links are taken as zero.

Links 6 to 9 in Figure 4.1 are the rollers used in the previous study [3]. When MFG is not connected to the machine, they may be considered to be rigidly connected to links 2 and 4. Therefore, their masses are included in the mechanism. The rollers rotate when they are connected to the MFG. Thus, their inertias are included in the MFG design. Centers of rollers 6 to 9 are labelled as R_{23} , R_{43} , R_{42} and R_{22} respectively.

The forces applied by links 3 & 5 of MFG on links 6 to 9 of the machine (i.e., \vec{F}_{36} , \vec{F}_{37} , \vec{F}_{58} and \vec{F}_{59} ,) are shown in Figure 4.1 with dashed arrows. The forces are applied at the contact points (between links 3 & 5 and the rollers (Links 6 to 9)), which are denoted as R_{32} , R_{33} , R_{52} , and R_{53} , respectively (see the figure). If the MFG is not connected, these forces will be zero.

It should be noted that MFG (without the machine) will consist of links 1, 2, 3, 4, 5, 6, 7, 8 and 9 [see Figure 1.1 and Figure A.1 (when links 3 and 10 are rigidly connected to form link 3; and link 5 and link 11 are rigidly connected to form link 5)]. Referring to the Figure 4.1, the resultant force acting on link 2 will be equal to the vector sum of the forces \vec{F}_{f2} , \vec{F}_{s2} and $\vec{F}_{13,2}$ where $\vec{F}_{13,2}$ is the force applied by link 13 on link 2

(due to the revolute joint connecting these two links). The force system consisting of the external forces, \vec{F}_{f2} , \vec{F}_{s2} and $\vec{F}_{13,2}$ (see Figure 4.1) and the force system consisting of the single external force \vec{F}_2 shown in Figure 1.1 are, clearly, not statically equivalent. Note that, \vec{F}_2 is parallel to the $\vec{u}_1^{(1)}$ axis and the line of action of \vec{F}_2 is coincident with the x-axis of \mathcal{F}_1 .

Similarly, referring to the Figure 4.1, the resultant external force acting on link 4 will be equal to the vector sum of these forces \vec{F}_{f4} , \vec{F}_{s4} and $\vec{F}_{14,4}$ where $\vec{F}_{14,4}$ is the force applied by link 14 on link 4 (due to the revolute joint connecting these links at the point R_{45}). The force system consisting of the external forces \vec{F}_{f4} , \vec{F}_{s4} and $\vec{F}_{14,4}$ (see Figure 4.1) and the force system consisting of the single external force \vec{F}_4 shown in Figure 1.1 are, clearly, not statically equivalent. Hence the external loading on the MFG is not “balanced” as shown in Figure 1.1. Therefore, MFG will not be as dynamically favorable as in the ideal case (where the external loading is balanced as in Figure 1.1 and \vec{F}_2 and \vec{F}_4 satisfy equation (1.37)).

Note also that the center of masses G_2 and G_4 (see Figure 4.1) are not located on the line connecting the points R_{41} and R_{21} (as should be the case as implied by equation (1.31)). Hence, MFG will not be as dynamically favorable as in the ideal case where the mass centers G_2 and G_4 are located in accordance with equation (1.31).

4.2.2. Description of Reference Frames

Body fixed reference frames of links 1,2 and 4 are as shown in Figure 4.1. Origins are denoted with O_i , axes of the references are shown with the unit vectors $\vec{u}_j^{(i)}$ where “i” belongs to the link number, j belongs to the axis number (1 for the horizontal axis, 2 for the vertical axis, see Figure 4.1). Since the previous experimental setup [3] for the MFG is used as the machine, note that the reference frames and the reference points are similar to the MFG model given in Figure 1.1.

4.2.3. Crank & Coupler Links

Crank is the link numbered as 12 in Figure 4.1. It is connected to the ground (at the middle of the link) with revolute joint as can be seen from the figure. Center of mass of the crank, G_{12} , is on the axis of rotation of link 2. The crank is connected to two identical couplers (namely, links 13 & 14) with revolute joints. The distances from these revolute joints to the rotation axis of the crank are denoted as l_{crank} . The crank angle θ is measured in counter clockwise direction, around the axis $\vec{u}_3^{(1)}$.

The identical couplers have two ball bearings inserted inside them as the two revolute joints. The distances between the revolute joints on the couplers are denoted as $l_{coupler}$. Center of mass of the couplers G_{13} & G_{14} are located in the middle of the couplers. The coupler angle ϕ is measured as shown in the figure. The coupler links 13 & 14 are connected to the sliders such that the centers of the bearings are at the reference points R_{25} and R_{45} .

4.2.4. Slider

The prismatic joints between the slider links 2 & 4 and the ground are provided with a linear motion system consisting of ball bearings, which recirculate in a cart on a rail. Origins of the reference frame of the slider links are selected to be in the middle of the contact lines of the recirculating ball bearings with rail (see section 5.2.1.8. for detail).

4.2.4.1. Friction Forces

Friction between the sliders and the ground link can be assumed to be constant if the load on the slider is small enough according to a technical information note of a linear motion system company [15]. The load capacity of the sliders and applicability of this assumption is discussed in section 5.2.1.8. For the simulations in this study, friction between the sliders and the ground are assumed to be constant and determined experimentally. The application point of the friction forces \vec{F}_{f2} and \vec{F}_{f4} (on links 2 & 4) are the origins O_2 and O_4 respectively. The line of action of the friction forces is on the line O_2O_4 .

The positions of the sliders (s_2 & s_4) are measured from the origin O_1 to the reference points R_{21} and R_{41} , respectively, i.e.,

$$\begin{aligned} s_2 &= \vec{u}_1^{(1)} \cdot \overrightarrow{O_1 R_{21}} \\ s_4 &= -\vec{u}_1^{(1)} \cdot \overrightarrow{O_1 R_{41}} \\ s_2 &= s_4 \end{aligned} \quad (4.1)$$

The magnitude of friction force is denoted as f_{14} which is assumed to be same for the frictions of both sliders, given by the equation

$$\vec{F}_{f2} = -\vec{F}_{f4} = -f_{14} \text{sign}(\dot{s}_2) \vec{u}_1^{(1)} \quad (4.2)$$

where \dot{s}_2 is defined via the equation

$$\dot{s}_2 = \frac{d}{dt} s_2 \quad (4.3)$$

Note that $R_{25}R_{45}$ line is parallel to the O_2O_4 line, i.e.,

$$R_{25}R_{45} \parallel O_2O_4 \quad (4.4)$$

In Figure 4.1, the friction force vectors have been shown with red arrows. Note that the friction forces are assumed to be constant regardless of whether the MFG and/or the spring load is connected to the mechanism or not.

4.2.4.2. Load Forces

Recall that the load spring is located between the sliders 2 and 4. The endpoints of the spring are at the reference points R_{24} and R_{44} (see Figure 4.1). Therefore, the spring length (l_s) can be obtained as

$$l_s = |R_{24}R_{44}| = 2s_2 + \overrightarrow{R_{21}R_{24}} \cdot \vec{u}_1^{(2)} + \overrightarrow{R_{41}R_{44}} \cdot \vec{u}_1^{(4)} \quad (4.5)$$

Now, denote the second and the third terms in equation (4.5) as the spring offset of the slider-crank mechanism ($l_{o,sc}$) and let these terms be equal to each other, i.e.,

$$l_{o,sc} = \overrightarrow{R_{21}R_{24}} \cdot \vec{u}_1^{(2)} = \overrightarrow{R_{41}R_{44}} \cdot \vec{u}_1^{(4)} \quad (4.6)$$

Here, it should be noted that R_{21} and R_{24} do not lie on a vertical line. Similarly, R_{41} and R_{44} do not lie on a vertical line as well (see Figure 4.1).

In order to calculate the spring force (F_{s2}), denote the free length of the spring as ($l_{free,sc}$), the initial tension (see 2.3.1 for definition) of the extension spring as F_{s20} and the spring stiffness as k_{sc} . Then the spring force can be obtained as shown below.

$$\begin{aligned} \vec{F}_{s2} &= -\vec{F}_{s4} = -F_{s2} \vec{u}_1^{(1)} \\ F_{s2} &= -k_{sc} l_{sc} - F_{s20} \end{aligned} \quad (4.7)$$

where, l_{sc} is the deformation of spring defined by the equation

$$l_{sc} = 2s_2 + 2l_{o,sc} - l_{free,sc} \quad (4.8)$$

In Figure 4.1, the spring load force vectors have been shown with red dashed arrows. When the spring is not connected, these forces are taken as zero in the dynamic analysis.

4.2.5. Dynamic Analysis of the Machine

Using the parameter sets given in Table 4.1 and the rotation of crank angle with respect to time, the velocities and the accelerations of the machine links are (where they are required for dynamic analysis and MFG design). Link masses, inertias, spring parameters are used for the dynamic analysis. The objective of dynamic analysis is to determine the motor torque required to overcome the external, inertial and friction forces and moments. For the dynamic analysis of the machine, the following assumptions are made

1. All links are assumed to be rigid, thus deformations of the links are neglected.
2. Frictional losses due to reaction forces and moments at the joints are neglected.
3. Constant friction is assumed on the slider links due to the recirculation of the balls and the preload (see 4.2.4.1 and 5.2.1.8 for details).
4. Inertial forces and torques are included.

5. External forces are applied as shown in Figure 4.1, such that forces applied on link 2 and 4 are equal in magnitude and opposite in direction as given in equations (4.2) and (4.7).

Due to the second assumption, dynamic analysis boils down to linear equation solving. Since the kinematic analysis of the slider-crank mechanism is trivial, the details are not provided in this study. One may refer to the previous works [4] or [16] for the kinematic and force analysis of mechanisms.

4.3. Simulation Conditions and Parameter Sets

Simulation conditions and the parameters for the machine and the MFG are provided in this section.

4.3.1. Simulation Conditions and Parameter Set for the Machine

For the crank and the coupler links, center of masses are at the geometric centers of the links. The mass, inertia and the length parameters are calculated by using CAD software, except for the mass of slider which is measured using an electronic scale with $\pm 15\text{g}$ sensitivity. The inertia of the DC motor's rotor (obtained from its datasheet) is added to the crank inertia (obtained by CAD). Materials of the links are given in 5.2.1. Spring parameters are calculated experimentally (see section 5.2.1.7 for details). The constant friction is measured roughly with an electronic scale (see 5.2.1.8) and then modified slightly by comparing the simulation and the experimental results of motor power calculations. The table consisting of aforementioned parameters for the symmetrical slider-crank mechanism are given in Table 4.1. Some additional are shown in Figure B.1.

In order to obtain a high torque output, the speed of the motor output shaft (or equivalently the crank rotational speed), denoted as ω , is selected as slow as possible. The spring load is determined experimentally by trying different springs. The MFG is designed for the constant crank angular speed given by

$$\omega = 0.1(2\pi) \text{ rad/s} \quad (4.9)$$

Table 4.1. Parameters and initial conditions used in simulations (for the machine)

Parameter	Value	Definition
l_{crank}	40 mm	Crank link length
$l_{coupler}$	100 mm	Coupler link length
m_{12}	0.092 kg	Mass of the crank
m_{13}	0.012 kg	Mass of the couplers ($m_{13} = m_{14}$)
m_2	1.365 kg	Mass of the slider links ($m_4 = m_2$)
I_{12}	71e-6 kg·m ²	Inertia of crank, DC motor's rotor and the gearbox about the rotation axis (same as center of mass)
I_{13}	3.52e-6 kg·m ²	Inertia of couplers about center of mass ($I_{13} = I_{14}$)
k_{sc}	61.31 N/m	Stiffness coefficient of the spring between the sliders
$l_{free,sc}$	58 mm	Free length of the spring
$l_{o,sc}$	15 mm	Spring hook connection offset to slider motion s_2
F_{s20}	1.8482 N	Initial tension on the extension spring
f_{14}	3N	The magnitude of constant friction on the slider bearings due to preload and recirculation of balls
$\theta(0)$	π (rad)	Initial Crank angle
$\phi(0)$	π (rad)	Initial Coupler angle
$s_2(0)$	0.060 (m)	Initial slider position

4.3.2. Parameter Set for MFG design

In this study, some design parameters of the MFG are already known since the MFG frame of the previous study [3] has been used. The springs are selected from the available items in the previous study as well. The known data and the data to be designed are given in Table 4.2. The inertia values of the rollers are obtained from CAD software and the remaining parameters are measured values. For the definition of the length parameters b_1 , b_2 and b_3 , see Figure 2.1.

Table 4.2. Available parameters and design parameters for the MFG

Parameter symbol	Value	Description
m_2	0*	Mass of link 2 and link 4
m_3	T.B.D.**	Mass of link 3 and link 5
I	2e-7 kg·m ²	Inertia of the rollers (Links 6, 7, 8 and 9)
r	11 mm	Radius of the rollers
b_1	306 mm	Length between link 2 center line and spring ground connection point
b_2	127.5 mm	Length between the reference points R ₂₁ & R ₂₃ in Figure 4.1
b_3	-10 mm***	Link 3 or 5 reference frame origin to spring connection point on the same link in the direction of $\vec{u}_2^{(3)}$ or $\vec{u}_2^{(5)}$, respectively
$y(s_2)$	T.B.D.**	Spring elongation profile with respect to link 2 position
y_0	T.B.D.**	Initial spring elongation when link speeds are zero
k_3	2×64.0847 N/m	Spring stiffness connected to link 3 or link 5 (2 Springs are connected to each of link 3 and link 5)
$l_{free,mfg}$	95 mm	Free length of the spring connected to link 3
F_{s30}	0.98057 N	Initial tension of one spring connected to link 3 (see section 2.3.1 for definition)
d_0	30.14 mm	Spring virtual elongation in free length (see section 2.3.1 for definition)

* : Since there is only one rail in the experimental setup, the sliders have to be shared between machine and MFG, therefore mass is included in slider mass of the symmetrical slider crank mechanism (see Figure 4.1 and 4.2.1 for shared links)

T.B.D.** : To be designed in this section

*** : Determined in implementation of the design See 5.2.2.5

4.4. Performance of the Machine without MFG

Using kinematic analysis, the position (s_2) and the velocity (\dot{s}_2) of link 2 is determined by using the motor shaft velocity (ω) [see equation (4.9)]. Plots of s_2 and \dot{s}_2 vs time are given in Figure 4.2. Note that the period of motion (T) is 10 seconds. The sliders start with minimum length (i.e., $s_2(0) = 0.06$ m), reach to the maximum position at $T=5$ s and the return to the initial position at the end of the period.

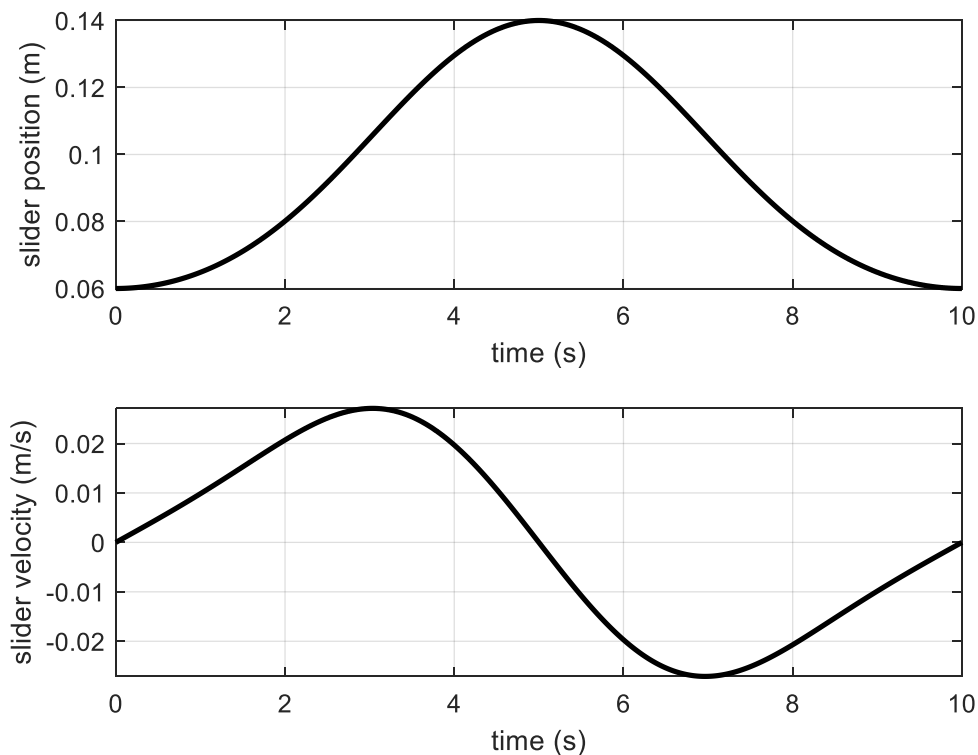


Figure 4.2. Slider position (s_2) and velocity (\dot{s}_2) with respect to time for the symmetrical slider-crank mechanism

The spring forces and the friction forces on the sliders are calculated using equations (4.2) & (4.7) (see Figure 4.3). The spring force and the friction force in the figure are given in the sense of the unit vector $\vec{u}_1^{(1)}$. Recall that $\vec{u}_2^{(1)}$ and $\vec{u}_3^{(1)}$ components of these

force vectors are zero. The direction of the friction force in the figure changes due to the change in sign of the speed of link 2.

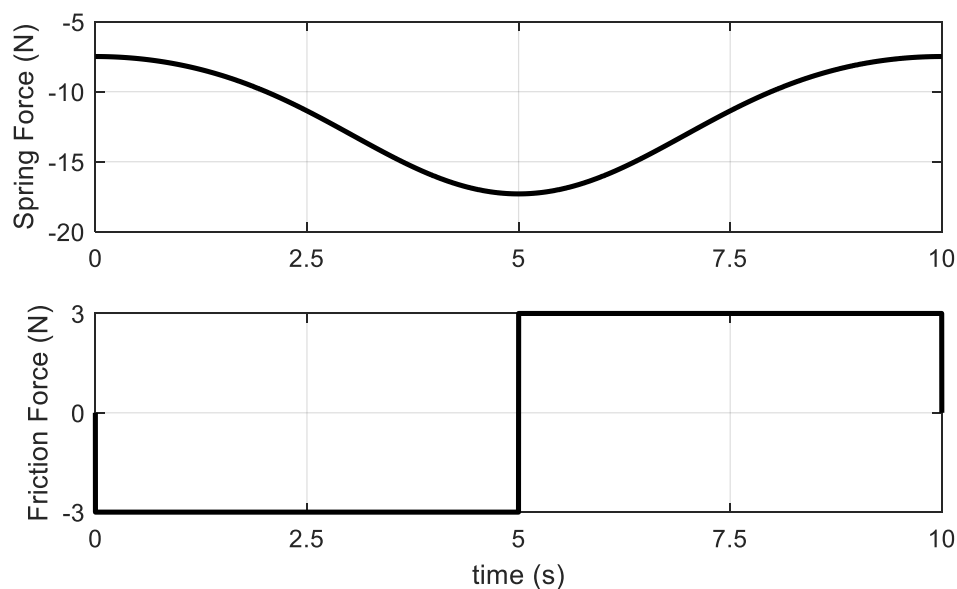


Figure 4.3. $\vec{u}_1^{(1)}$ components of symmetric slider crank spring load and friction force vectors on link 2

By performing dynamic analysis, the required motor torque is obtained (see Figure 4.4). See section 4.2.5 for the assumptions used in the dynamic analysis and Table 4.1 for the parameters and the initial conditions used in the simulation. Note that the crank angular speed is constant. Therefore, the motor power is a constant multiple of the motor torque.

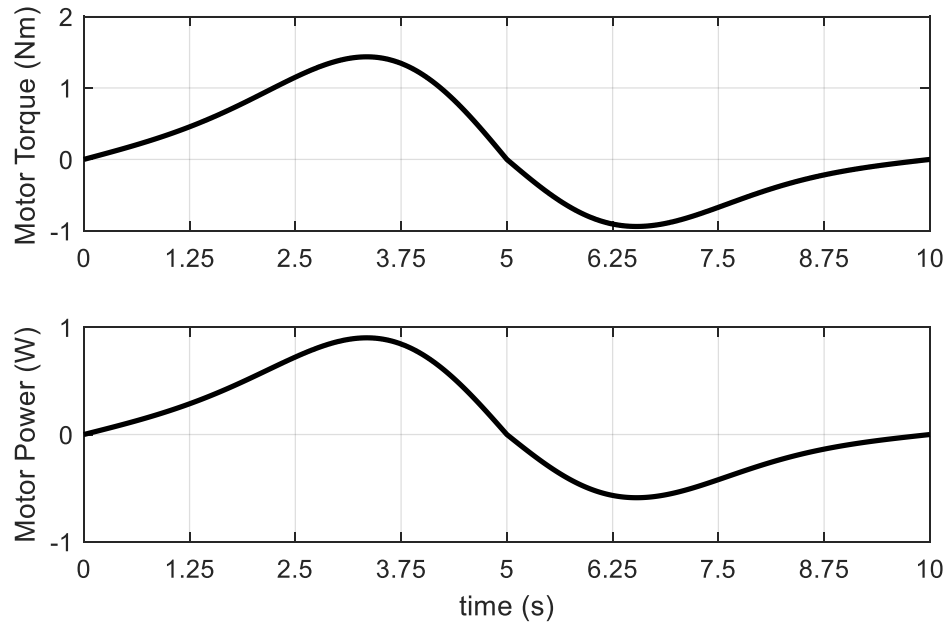


Figure 4.4. Torque (T_{motor}) and power requirement from motor (P_{motor}) without MFG

4.5. MFG Power Variation Design

In order to improve the performance of the machine, in this section, the power output of MFG (P_{mfg}) is calculated. Recall that the external load applied on the mechanism is due to the spring between links 2 & 4. Since the motion of the sliders is periodic, the load does conservative work on the mechanism. Therefore, the work done by the machine, for the load, in one period (E_{out}) is zero, i.e.,

$$E_{out} = 0 \quad (4.10)$$

Recall that when the angular speed of the motor shaft (ω) is constant, the optimum motor power (P_{motor}^*) is the same for all of the optimization methods (namely, the minimizing maximum motor power in 3.3.3.1, the minimizing maximum torque in 3.3.3.2 and the minimizing the copper losses 3.3.3.3) as shown in equations (3.33), (3.45) and (3.60). By substituting equation (4.10) into equation (3.33), one obtains

$$P_{motor}^* = \frac{E_{out}}{T} = 0 \quad (4.11)$$

Therefore, the optimum motor torque for the MFG design is also zero, i.e.,

$$T_{motor}^* = 0 \quad (4.12)$$

Equation (4.11) implies that the motor will require no power to drive the load. Hence, all of the required power will be supplied by the MFG.

In the MFG design the power losses shown in Figure 3.1 and the mechanical energy change of the machine ($\dot{E}_{machine}$) are neglected. Therefore, the task power (P_{task}), becomes equal to output power (P_{out}) using equation (3.6), i.e.,

$$P_{task} = P_{out} \quad (4.13)$$

Recall that P_{task} was defined to be the mechanical output power of the motor without the aid of MFG, and P_{out} was defined to be the total power required to drive the load in Section 3.2.1.

In the MFG design, the output power is calculated by using the spring forces (F_{s2}) to be the external force (F_2) on the MFG (see equation (4.7) for F_{s2}). By using the spring forces and the slider velocity, the output power of the machine (to drive the spring load) can be calculated using equation (3.11) to yield

$$P_{out} = -2F_{s2}\dot{s}_2 \quad (4.14)$$

By substituting the optimum motor power (P_{motor}^*) given by equation (4.11) into (3.8), one can determine the optimum MFG power (P_{mfg}^*) as:

$$P_{mfg}^* = P_{out} \quad (4.15)$$

Since the output power is derived using equation (4.14), the output power is equal to zero when the slider velocity is zero. Therefore, the second limitation defined in equation (1.42) is already satisfied. As a result of this, the compensation algorithms discussed in sections 3.3.4 and 3.3.5 are not required. Hence, the MFG power is equal to the optimum MFG power, i.e.,

$$P_{mfg} = P_{mfg}^* \quad (4.16)$$

The power, torque, force, and work done by the motor, by the MFG and the task are given in Figure 4.5. Note that, the motor force (F_{motor}), is calculated by using the equation

$$F_{motor} = F_{task} - F_{mfg}, \quad (4.17)$$

It is observed that F_{motor} is constant, and highly similar to the friction force given in Figure 4.3. This implies that the inertial forces are very small compared to frictional.

Recall that spring load is completely cancelled by the MFG according to the design. Therefore, for the calculation of work done by the MFG, change in the elastic energy of the spring is used such that:

$$W_{mfg}(t) = \int_0^t (F_{s2}(t)\dot{s}_2(t)) dt \quad (4.18)$$

where l_{sc} is given in equation (4.8), F_{s2} is given by equation (4.7).

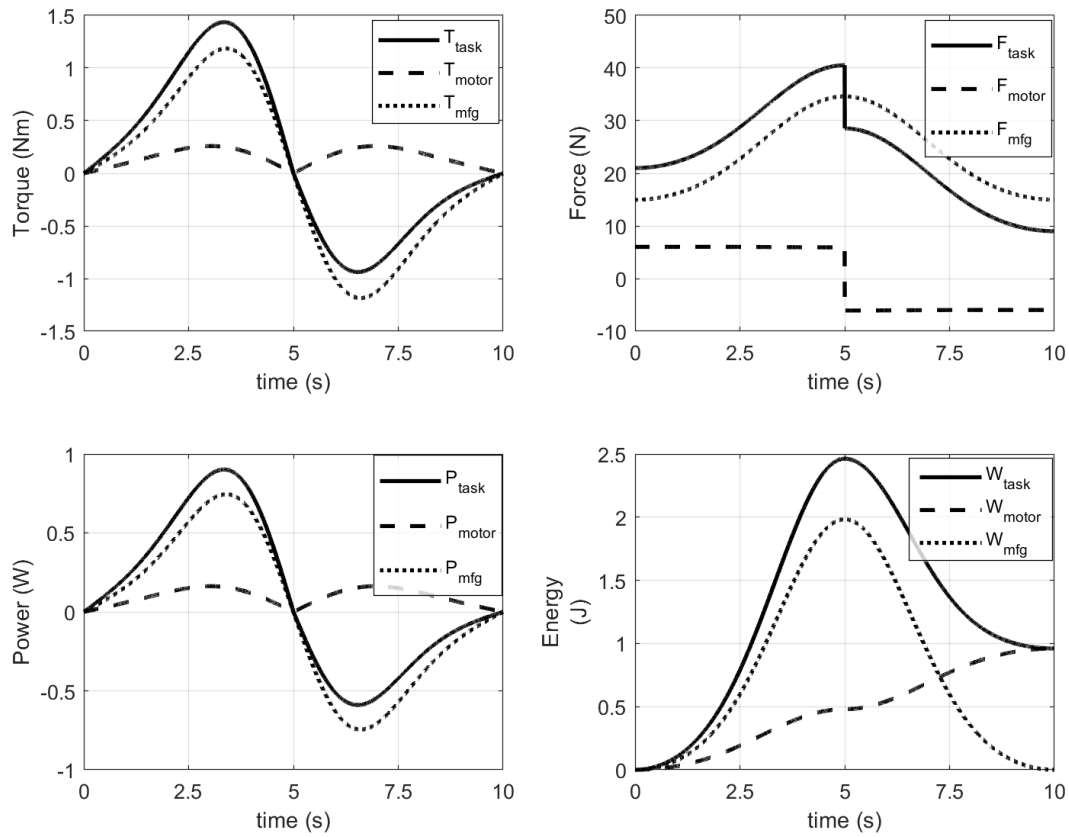


Figure 4.5. Torque, Force Power and Energy distribution between the MFG and the Motor (for all performance optimization methods in Section 3.3.3)

Minimum values of the performance measures after the optimization (see section 3.3.2 for definitions of the performance measures) are given in Table 4.3.

Table 4.3. Minimum values of the performance measures

Minimize max power: J_P	Minimize max torque: J_T	Minimize copper losses: J_E
0.18031	0.18031	0.051694

In order to design an MFG with an open slot profile, one should check if the work done by the MFG (W_{mfg}) and the position of link 2 (s_2) allow for an open slot design. In other words, the conditions mentioned in 3.4.2.1 need to be checked to see if the resulting slot profile is open. The plots mentioned in the first two methods are given in Figure 4.6, it can be observed that the plot on the left is single-valued and the plot on the right is approximately zero for all times in a period. Thus, the profile is determined to be an open slot. The small deviations from zero in the right plot is due to the numerical errors of the computation.

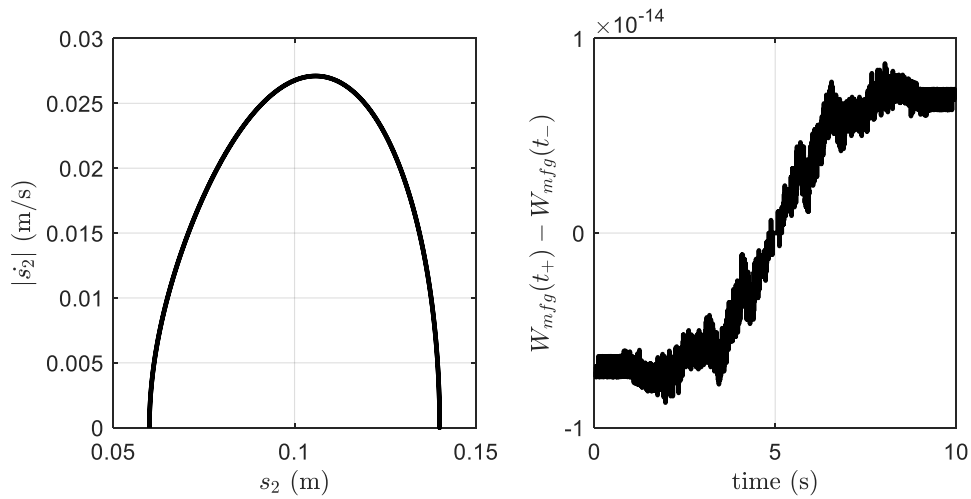


Figure 4.6. Open slot profile feasibility test (First two steps in section 3.4.2.1)

4.6. MFG Design

Once the power variation is calculated one can start designing the MFG using the dimensions and spring parameters given in Table 4.2.

4.6.1. Design with Different Spring Preload Values

Two MFGs are designed with different spring preload values. The designs are given in the following subsections.

4.6.1.1. Design Using Minimum Spring Preload Length

The steps in Section 2.4 are followed to determine the parameters. For the first step of the method given in Section 2.4, most of the parameters are already known since the MFG components from the previous study [3] are used. There were several types of springs available from the previous study and appropriate ones are selected intuitively. The parameters needed for the first step are given in Table 4.2. In the design, since links 3 and 5 are not on the same plane, possibility of collision is very low (see Appendix B for the dimensions of the machine from its CAD model).

The minimum spring preload length is calculated by equation (2.28), yielding

$$\begin{aligned} l_{mfg0} &= \sqrt{\frac{\max(W_{mfg} + B'\dot{s}_2^2) + k_3 d_0^2}{k_3}} - d_0 + l_{free,mfg} \\ &= 0.1956m \end{aligned} \quad (4.19)$$

(for the definition of B' see equation (2.23)). The maximum displacement of link 3 is estimated by equation (2.30), yielding

$$\Delta s_{3max} \approx 0.1006m \quad (4.20)$$

In the second step of the method given in section 2.4, the spring length variation ($l_{mfg}(t)$), is calculated assuming zero mass for link 3. The results are given with respect to link 2 position (s_2), in Figure 4.7. Observe that the initial spring length starts with the length calculated in equation (4.19). The final spring length, on the other hand, is the free length of the spring. Thus, the maximum displacement of link 3 is given by equation (4.20). The monotonical decrease in the spring length is due to the positive work done by the MFG from $t = 0$ s to $t = 5$ s, (see the work done plot in Figure 4.5). The energy of the MFG decreases during this time period.

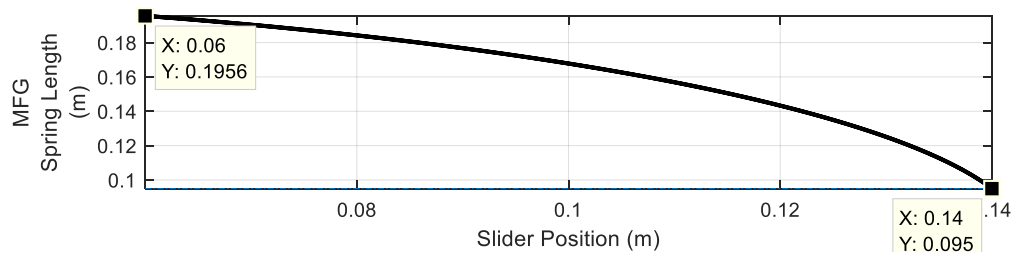


Figure 4.7. MFG Spring length vs link 2 position plot for minimum preload

In the third step, the path that the center of the roller 6 traces on link 3 reference frame is obtained. In the fourth step, this path is used to obtain a possible shape for link 3 by connecting the endpoints of the contact curves as shown in Figure 4.8. The path traced by the center of rollers are given with red dots on the figure.

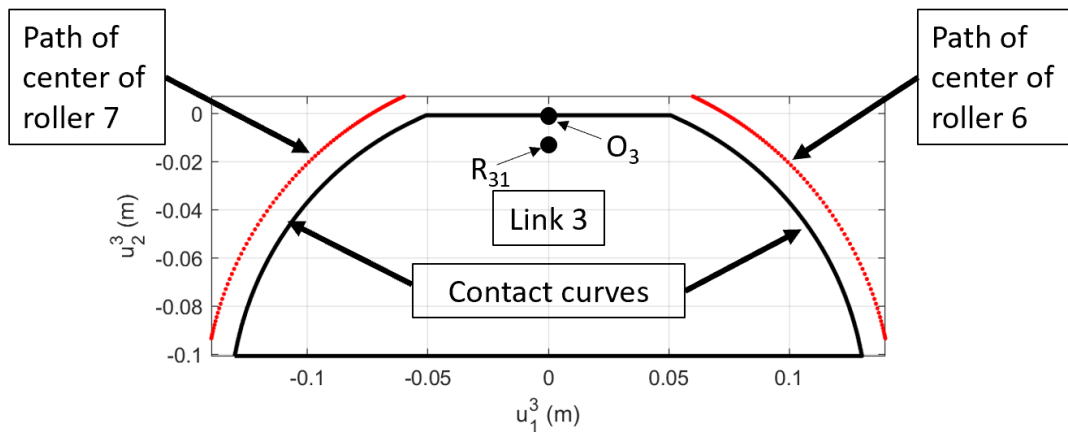


Figure 4.8. A possible shape for link 3 (to scale)

The thickness of the slot profile is selected as 12 mm and as the material, cast polyamide (1.15g/cm^3 density) is selected. The mass of link 3 is then calculated as 287.5 g by using a CAD software. A view from the CAD program is given in Figure 4.9. The mass of link 3 is considered to be high. Hence, in the next section, by using higher preload, a lighter link 3 will be designed.

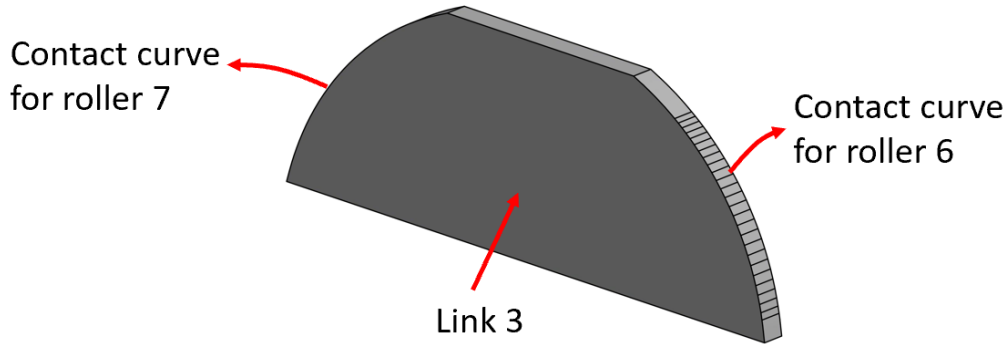


Figure 4.9. A CAD view of the shape of link 3 (designed with minimum preloaded spring length)

The normal forces vs link 2 position (s_2) plot is given in Figure 4.10. Referring to Figure 4.8, it is clear that the normal forces should be in third quadrant, i.e., both x and y components should be negative, in order to have continuous contact between roller 6 and the slot shape all times. Figure 4.10 indicates that this is true and there is always contact between roller 6 and link 3. See section 2.7 for the definition of the force variables.

4.6.1.2. Re-design by Adjusting Spring Preload Length

By adjusting the spring preload length (l_{mfg0}), a slot profile with less mass and smaller size is obtained. The initial preload length is selected as 225 mm, i.e.,

$$l_{mfg0} = 225 \text{ mm} \quad (4.21)$$

In the second step of the method given in section 2.4, the spring length variation ($l_{mfg}(t)$), is calculated by assuming zero mass for link 3 and the by using adjusted initial preload length (given in equation (4.21)). The spring length variation thus obtained is given in Figure 4.11. By comparing Figure 4.7 and Figure 4.11, it can be observed that by increasing the spring preload, one can reduce the range of spring length. In the figure difference between the maximum and the minimum spring length

is reduced to around 60 mm. From the figure, it can also be observed that the minimum spring length is higher than the free length, as expected.

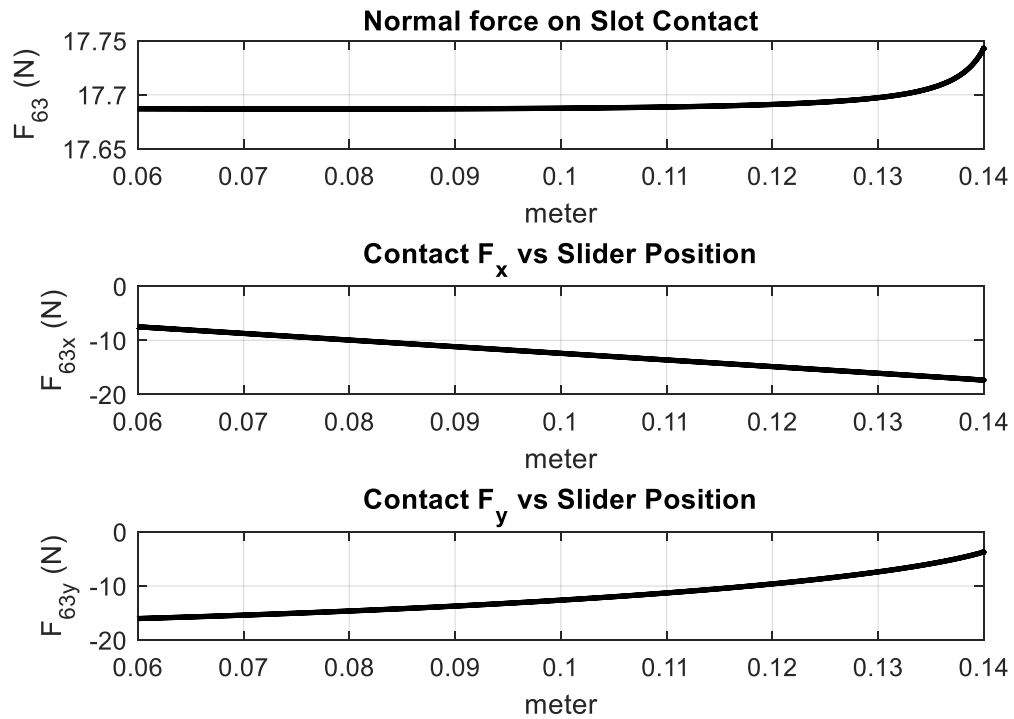


Figure 4.10. Slot profile contact surface normal forces, horizontal and vertical components vs s_2

In the third step of the method discussed in Section 2.4, the slot profile shape is generated. The resulting shape of link 3 is shown in Figure 4.12. The red dots in the figure are the traces of the roller centers. Note that the origin O_3 and the spring connection reference point R_{31} are closer to the mass center of the slot profile (which is more useful than previous design for practical reasons).

Since a higher spring preload length is used in this design, the forces developed within the MFG springs increase. Therefore the $\vec{u}_2^{(1)}$ component of the normal force applied

by link 6 on link 3 (\vec{F}_{63}) in equation (2.45) increases. Moreover, since the objective of the minimum spring preload length and adjusted preload length designs are the same, $\vec{u}_1^{(1)}$ components of the normal forces are equal in both designs. Higher normal forces are observed in Figure 4.13 compared to Figure 4.10. Referring to Figure 4.13, it can be observed that both x and y components of the forces are negative, similar to previous design. Thus, contact is maintained throughout the motion.

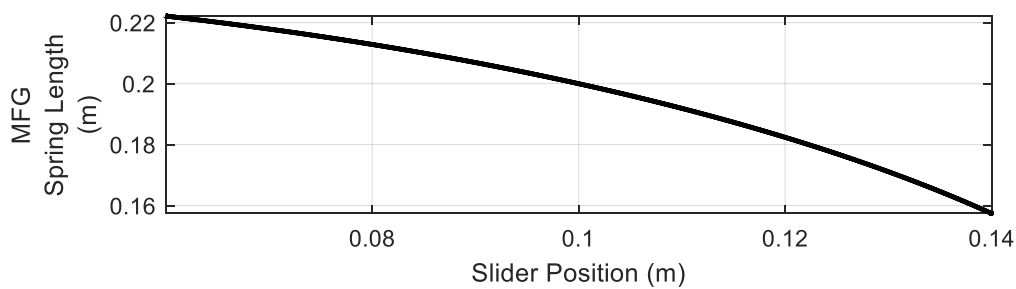


Figure 4.11. MFG Spring length vs link 2 position plot for adjusted preload

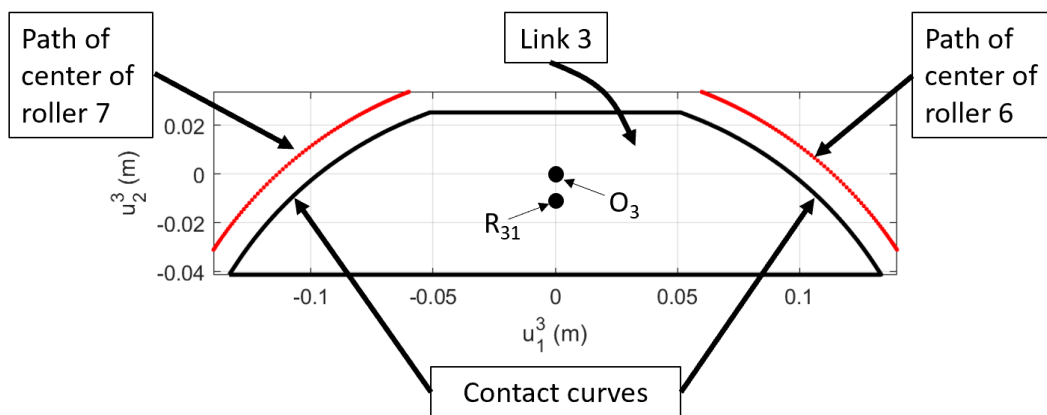


Figure 4.12. To scale shape of link 3 to be used in the experiment

In the fourth step of the method given in Section 2.4, shape of link 3 is generated. Some parts of link 3 are extracted in order to reduce the mass even further. The slot

profile with 12 mm depth and cast polyamide material is shown in Figure 4.14. The mass of the slot profile is calculated as 110 g. Hence, it can be concluded that mass of link 3 can be reduced greatly by adjusting the spring preload length.

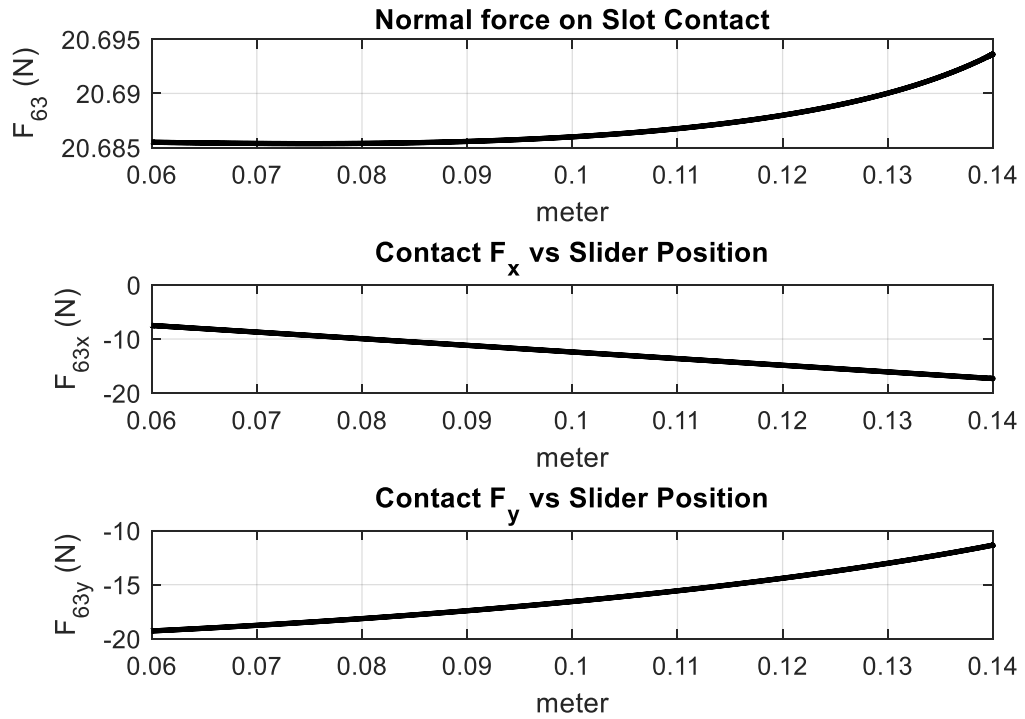


Figure 4.13. Slot profile contact surface normal forces, horizontal and vertical components

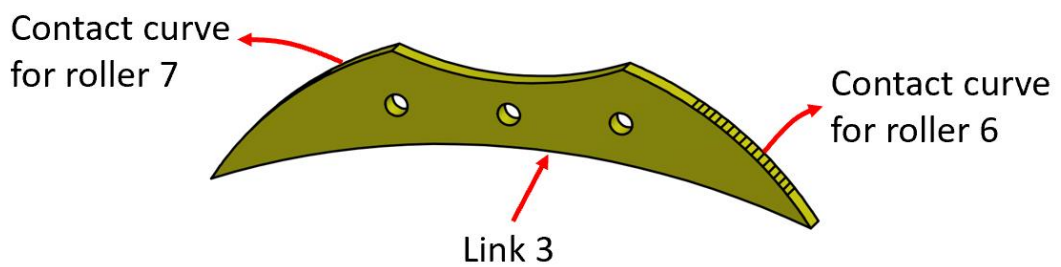


Figure 4.14. CAD design of the shape of link 3

In the first iteration of the iterative method, discussed in Section 2.5, the RMS error (ϵ) is found to be

$$\epsilon = 1.8477e - 05 \quad (4.22)$$

Since ϵ is very low, the spring length calculated in the first iteration is used in MFG design.

The radius of curvature of the slot profile is presented in Figure 4.15. Note that the radius of curvature is higher than the roller diameter, which is 0.022m, at all times. Therefore, undercutting does not occur.

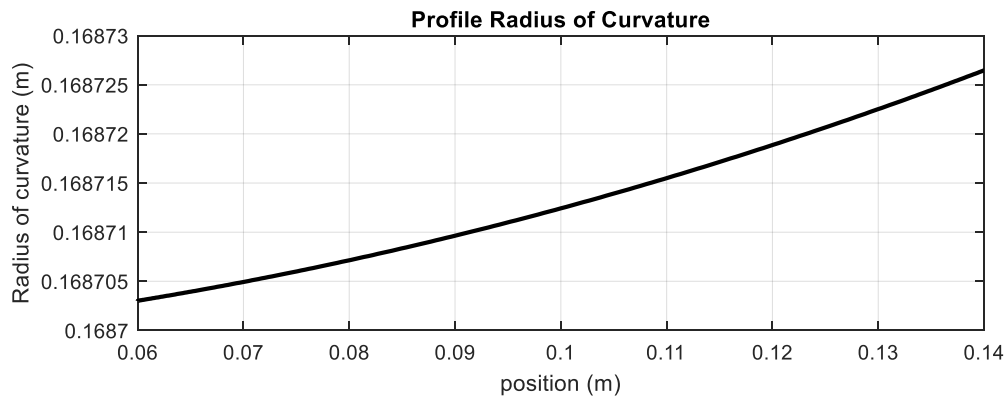


Figure 4.15. The radius of curvature of the slot centerline

CHAPTER 5

EXPERIMENTAL SETUP DESIGN

5.1. Introduction

In this chapter, the experimental setup which has been used to test MFG performance improvement is described. Firstly, the mechanical design of the components is presented. The components which have been changed with respect to the previously designed experimental setup in [3] are the symmetrical slider-crank mechanism, slot profile – ground link joints and the DC motor bracket for actuation of the mechanism. Strong and weak sides of the improved design are discussed. Assembly of the components is also described.

In order to actuate the mechanism, problems regarding the electronic components are mentioned. The electronic components and the DC motor used in the experiment are described.

Finally, the software algorithms are given. Problems regarding the algorithms are stated. Management of these algorithms is explained. DC motor control and speed measurement algorithms are also presented in this chapter.

5.2. Mechanical Design

The mechanical design of the experiment setup developed in [3] had to be improved in order to conduct successful experiments for the validation of the MFG concepts. Main difficulties related to the experiments conducted in [3] are listed below.

- Problems related to synchronous actuation of the two identical slider-crank mechanisms.
- The perfect alignment requirement of the prismatic joints of the slider link of the slider-crank mechanisms.

- Deviations from the designed inertial and kinematic parameters while manufacturing.

All of the above-mentioned difficulties are attempted to be addressed in this study. Details of the methods used in order to overcome these difficulties are given in the subsections.

5.2.1. Symmetrical Slider Crank Design

In this section, the design of the machine to be used in the experiment is discussed. Firstly, the problems faced in the previous experiments are addressed. Then, they are attempted to be solved in the new design. Properties, advantages, and weaknesses of the new design are also discussed.

5.2.1.1. Problem Statement

The alignment problem encountered in the two identical slider-crank pair is shown in Figure 5.1. Due to error in the parallelism of the slider rails, extensive reaction forces might occur at the slider-rail contact. As a consequence, the motor torque increases. This may degrade the performance of the experiment, as improvement of the motor performance is one of the goals. If the parallelism error is excessive, then the motor may not supply the required torque and the experiment cannot be conducted.

Another difficulty in conducting the experiment is due to the synchronized control of the two independent actuators. When the perfect synchronization is not achieved, actuators might oppose each other. This complicates the conduction of the experiment severely. Recall that the external forces applied on the MFG should be equal and in reverse direction as given by equation (1.37). In order to achieve accurate control, precise measurements of torque and position are necessary. However, such motion control systems are expensive.

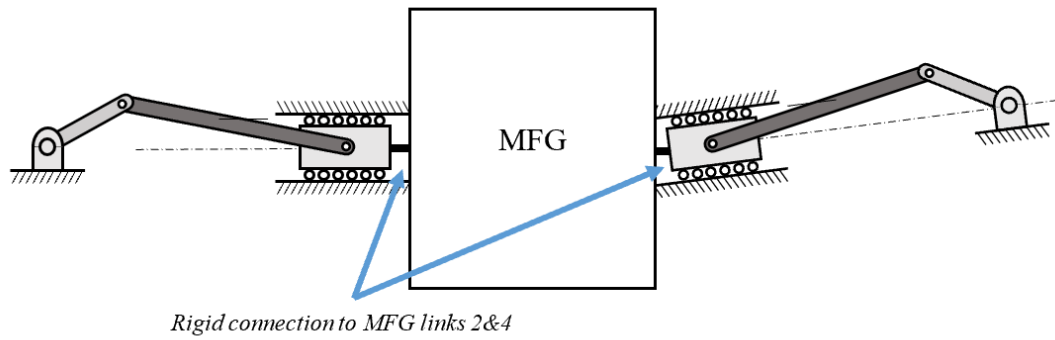


Figure 5.1. Alignment problem in the identical slider-crank mechanisms

In this study, a simpler approach is proposed by utilizing a symmetrical slider-crank mechanism driven by a single actuator. The mechanism is depicted in Figure 5.2. The alignment of the prismatic joints is achieved by using the same rail for both of the sliders.

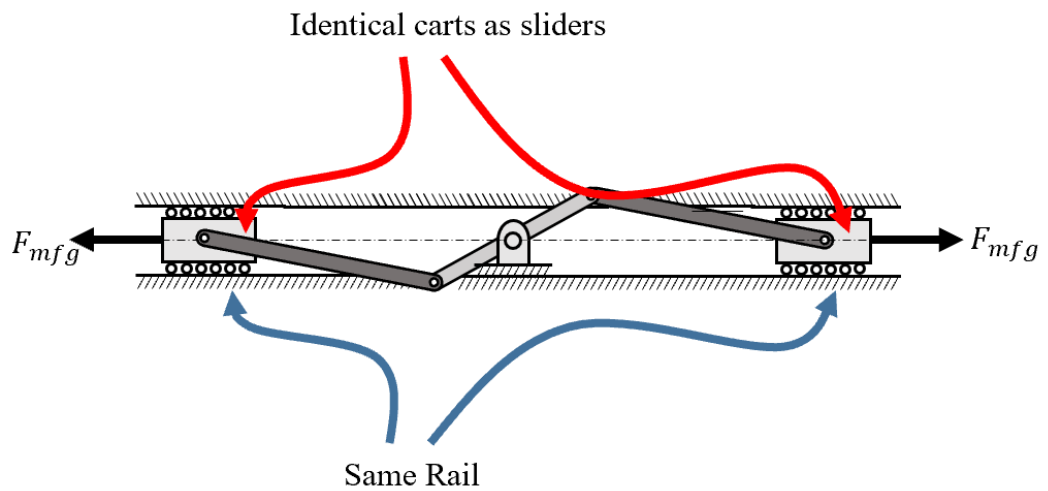


Figure 5.2. Symmetrical slider-crank mechanism schematics (solution to alignment of slider-ground prismatic joints)

In order to decrease the design and manufacturing costs, the frame used in the previous study is selected as the baseline for sizing decisions. This frame is labelled as the ground link, which consists of the gray bars in Figure 5.3.

There is very little space inside the frame to mount the symmetrical slider-crank mechanism. Furthermore, the position of the crankshaft is constrained to be in the middle of the MFG slot profile sliding rails (see Figure 5.3). In order to avoid collision with the slider links' (links 2 and 4) rails, the crankshaft has to be connected further away from the rails as the crank length increases. However, in order to decrease the reaction moments, the crank should be as close as possible to the rail.

The coupler links are constrained to be connected to the black bars on the sliders (see Figure 5.3). The available space for placing the symmetrical slider-crank mechanism is depicted using a CAD model in Figure 5.4.

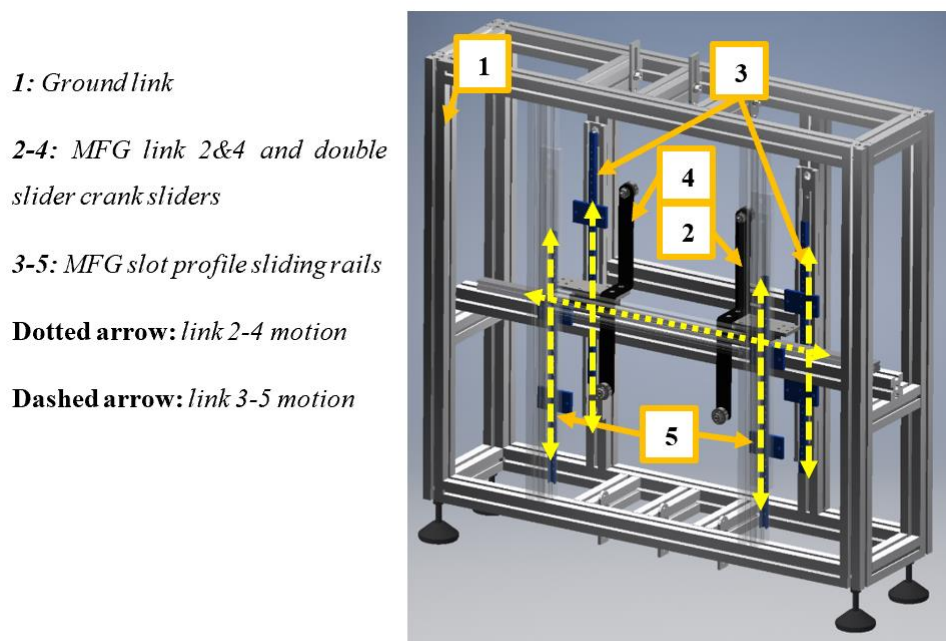


Figure 5.3. Frame used in the experiment of the previous study [3]

The last, but not the least, difficulty is minimizing the out of plane moments. In order to minimize the out of plane moments, all of the designed components should be as close as possible to the vertical plane passing through the geometric center of the frame (view in the bottom of Figure 5.4). See Appendix B for the important dimensions of the MFG from the CAD model.

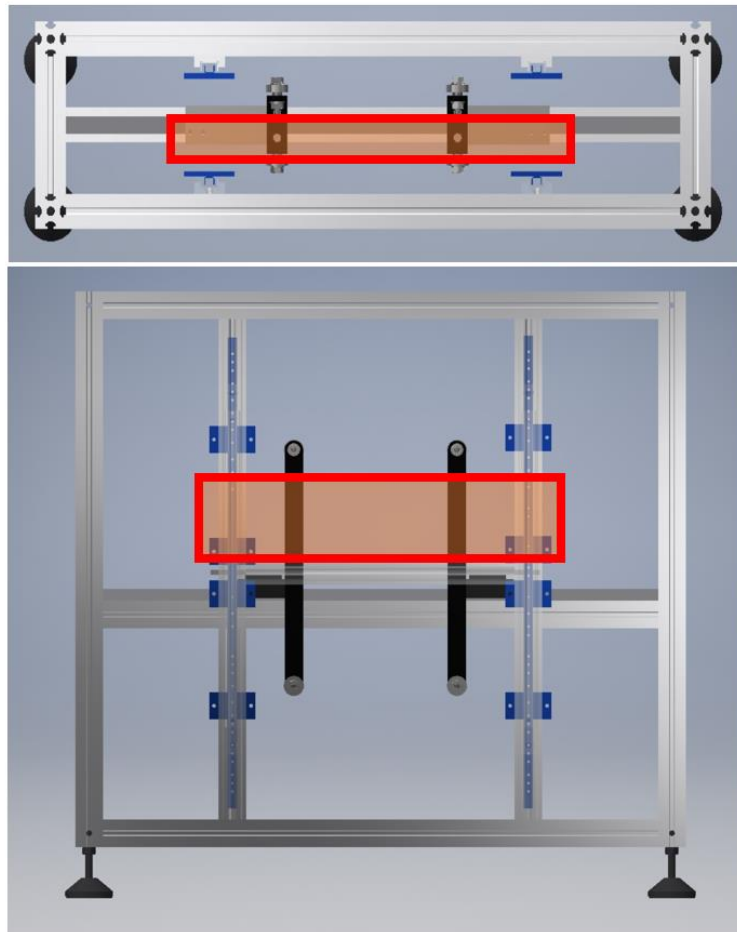


Figure 5.4. The estimated available region for symmetrical slider-crank mechanism (shown with the top and front view of the experimental setup CAD model)

5.2.1.2. Crank Design

The design should allow continuous rotation of the crank, which implies that the links must not collide during the whole range of crank angles. As for the continuous rotation, crank link must be smaller than the coupler link. Recall also that in the slider-crank mechanisms without eccentricity, stroke is two times the crank length, i.e.,

$$stroke = 2 \cdot crank_length \quad (5.1)$$

In order to use greater part of the rail, a long stroke length is desirable. However, as explained in the previous section, if increased stroke is desired, one must increase the distance of crankshaft to the sliders' rail in order to prevent collision.

In the design of the crank link, the crank of a two-cylinder internal combustion engine has been imitated. In this extent, one end of the crank is connected to the DC motor shaft and the other end has to remain free because there is no space to place a shaft support component. This means that reaction forces and moments will be applied on the motor shaft, reducing life and performance of the motor. However, since the loads are expected to be low, this is neglected in the scope of the study.

The crank assembly is given in Figure 5.5. The cranks are manufactured by using a steel strip with 2mm x 20mm size cross-section. Between the two strips, there are two coupling components (to insert the bearing for the crank-coupler joint and to allow some free distance to prevent collision). These coupling components are fixed to the strips by applying adhesive epoxy (BISON 2 component epoxy). The bearing and the coupler link are mounted into outer component (blue component in Figure 5.5). Then, it is fixed by the threaded inner component (red component in Figure 5.5) and a bolt. Note that the heads of the bolts are at the outer side of the crank mechanism in order to prevent collision. Motor shaft coupling (teal-colored cylinder in Figure 5.5) is also fixed into the strip by using the same adhesive epoxy.

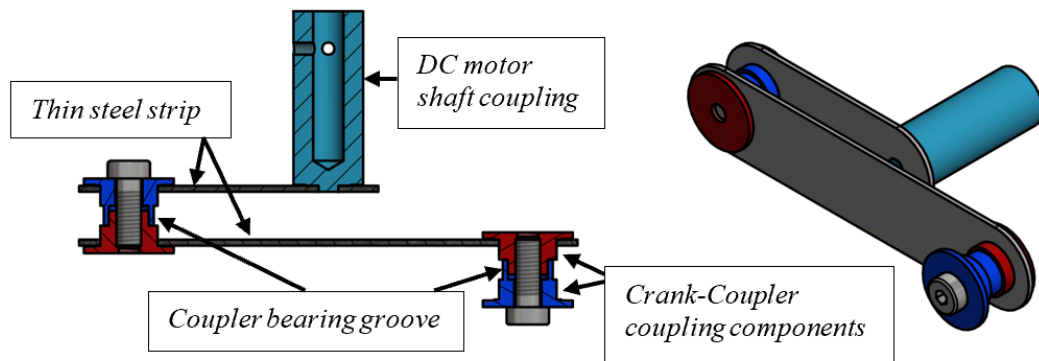


Figure 5.5. Cross-section and isometric view of the crank assembly

5.2.1.3. Coupler Design

Coupler length is dependent on the crank length. For the symmetrical slider-crank mechanism, in order to prevent collision, coupler length must be greater than two times of the crank length, i.e.,

$$l_{coupler} > 2l_{crank} \quad (5.2)$$

The CAD model of the designed coupler is given in Figure 5.6. Note the grooves to insert the bearings. There is also a smaller diameter hole at the end in order to ensure that the bearing can be mounted from only one direction.

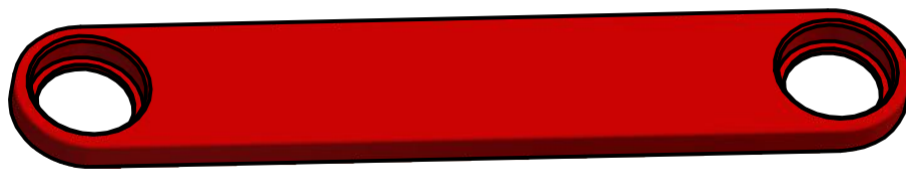


Figure 5.6. Coupler CAD model, grooves at the endpoints are designed to insert bearings

The coupler is manufactured using 3D printers and ABS material is used in the production. One drawback of using printers is that the hole diameters do not exactly match the designed diameter due to thermal expansion/contraction while the printer filament cools down. In order to overcome this problem, the design diameter has been increased experimentally to accomplish the fit with the desired tightness. After three iterations, it is decided that the dimensions are close enough. The final product allows some play (backlash) in out of plane directions (perpendicular to the direction of rotation). This play tolerance is shown in Figure 5.7. Referring to the figure, play is defined as the rotation of the coupler links in clockwise or counter-clockwise direction from their connection points. Observe that if the bottom coupler link (the bottom red link in the figure) rotates clockwise from its joint, it will collide with a part of the crank link. Hence it has no play tolerance in that direction. However, it has more tolerance to rotate in the counter-clockwise direction. The play tolerances are shown in the figure.

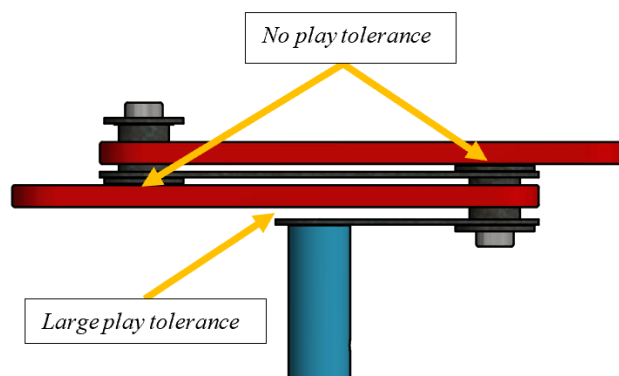


Figure 5.7. Coupler and Crank CAD model, design with zero play tolerance at two zones which are vulnerable to collision

Additional precaution is taken on the slider-coupler connection side by using the play of the connection in the next step.

5.2.1.4. Slider-Coupler Connection Design

The slider-coupler connection is obtained by connecting additional components to the already available slider component from the previous study [3]. The CAD model of the slider mount is given in Figure 5.8. Firstly, the slider mount is inserted into the slider link. Then, the bearing of the coupler link is connected to the long shaft in the figure.

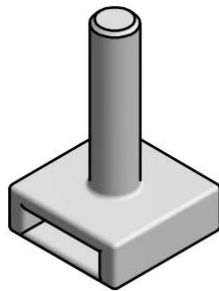


Figure 5.8. Slider Mount CAD model

The long shaft of the slider mount allows adjusting the crank coupler position manually. After the coupler link is inserted into the slider mount shaft, if the bearing of the coupler moves along the shaft during the motion, it is prevented by applying hot silicon near the edge of the bearing. The hot glue is also used to temporarily fix the slider mount into the slider. The hot glue has proved to be strong enough to withstand the reaction forces in the experiments. Note that, if required to the glue may be removed without giving harm to any component. The disadvantage of this method is that the flexibility of the system increases, thus response of the system is not rigid as assumed. This component is also produced by using ABS filament in a few attempts. After a few attempts, excess shaft diameter is removed by a turning machine. If the play tolerance mentioned in the previous section is very small (or none), then one may adjust position of the bearing on the shaft of the slider mount to prevent

collision (see Figure 5.9). By adjusting the bearing position, the angle between the couplers and the crank is slightly tilted away from the parallel configuration and, thus, the possibility of collision is reduced.

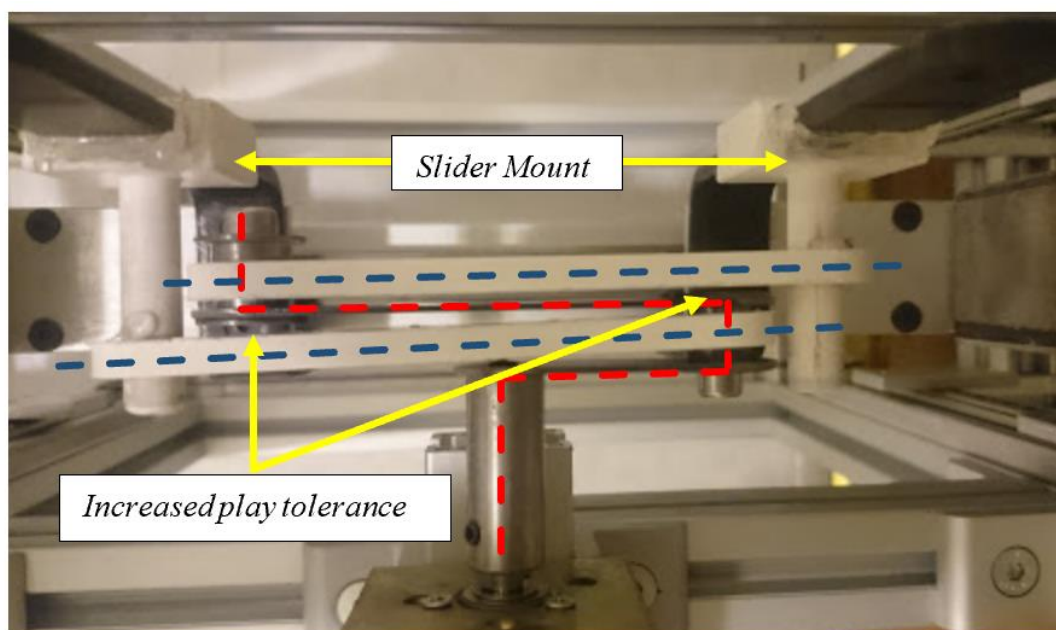


Figure 5.9. Increased play tolerance by fixing bearing at the slider mount such that crank and coupler is slightly tilted.

5.2.1.5. Motor Bracket

In order to fix DC motor to the frame (ground link), a short aluminum sigma profile is connected to the L shaped sheet metal. Then, the motor is fixed to the L bracket. All of the connections are made using bolts. The motor fixture can be seen in Figure 5.10.

5.2.1.6. Extra Mass Option on the Sliders

In order to simulate the inertial forces on the machine, an extra mass option is added to the symmetrical slider-crank mechanism. The masses have threaded holes and can be connected to the aluminum block of the slider via bolts. However, firstly, one needs

to disassemble the components in the slider link. Hence, whole slider-crank system should be disassembled. Thus, adding or removing different masses would be infeasible with this design. The aluminum block used to connect the mass is the component used in the previous study.

The inertial forces are dependent on the crank speed and the extra masses on the slider block. If the rated motor speed is low, then the inertial forces will be low as well. This is the case in this study; however, one may use faster motors to have large enough inertial forces.

During the experiments the extra masses were mounted on the system as demonstrated in Figure 5.10.

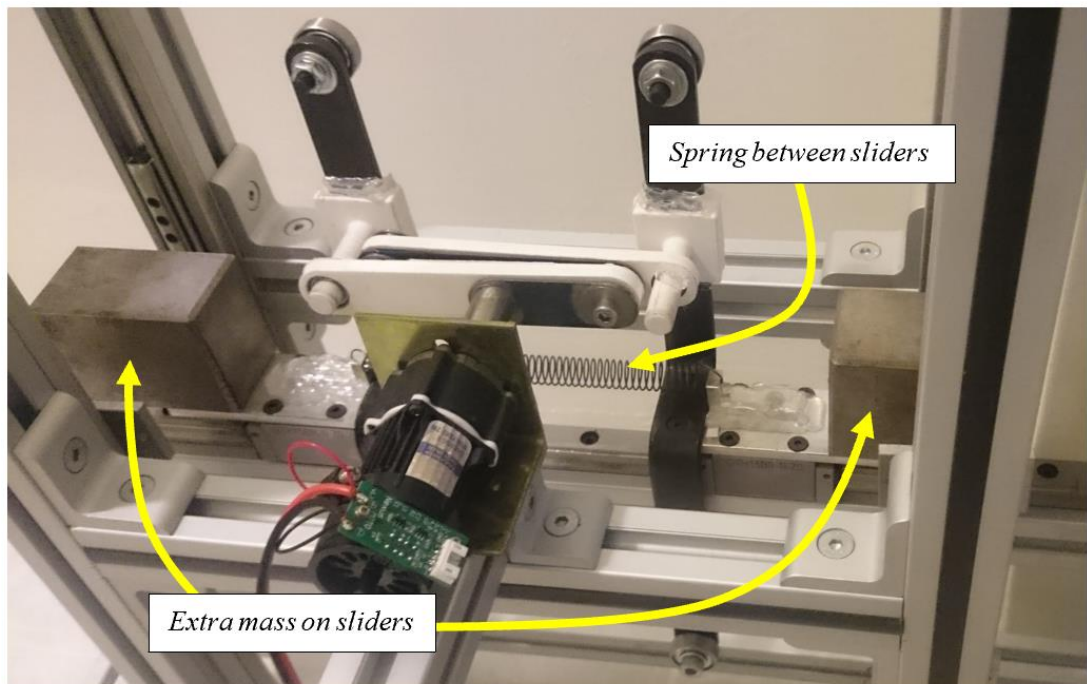


Figure 5.10. The symmetrical slider crank system used in experiment

5.2.1.7. Spring Option between Sliders

In order to simulate a conservative load, one spring is added between the sliders. The spring is connected to the L brackets available from the previous study [3]. The brackets are fixed to the slider by means of hot glue. The symmetrical slider-crank mechanism, with the spring between the sliders, is demonstrated in Figure 5.10. If the spring stays loaded when the MFG is not in operation, it should be removed from the brackets in order to not wear out the glue adhesive.

In order to obtain the initial tension of the spring used in the experiment, some measurements have been performed and the coefficients have been obtained by line fitting. The displacement from the free length vs spring tension force plot is given in Figure 5.11. Note that at zero displacement, there is a non-zero force. This indicates that the spring is an extension spring with initial tension.

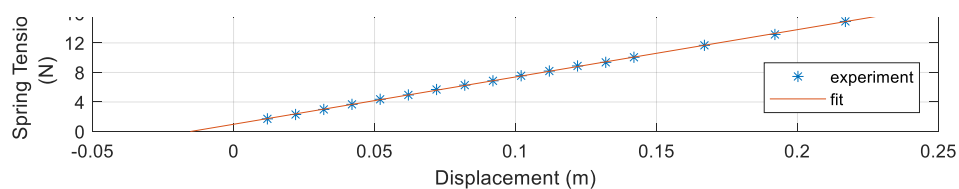


Figure 5.11. Spring coefficient measurement

5.2.1.8. Rail Cart System

The cart and rail are as used in the previous study. Recall that, only the friction on the cart rail system is taken into account in this study. The GTH-15-BN model cart of GTEN company is used. The rated dynamic load of the cart is 1152 kg and the static load is 1719 kg [17]. Although technical information for the linear motion system could not be found, the cart systems of another linear motion system company, HIWIN

[15], have been considered to be similar to the existing cart system. When the load on the cart is less than 10 % of the rated static load range, friction is mainly due to the friction resistance of the balls and the grease viscosity [15]. The friction resistance is mainly due to the recirculation of the balls. The recirculation is demonstrated in Figure 5.12.

Similar carts of HIWIN company have friction resistance ranging from 1-5 Newtons. Since experimental system loads are far below the 10% of the static load rating, constant friction has been assumed in the dynamical analysis of symmetrical slider-crank mechanism. The frictional resistance on the experimental setup sliders is measured roughly with a force sensor with different weights on the slider. Thus, the frictional resistance has been obtained to be approximately 3 Newtons.

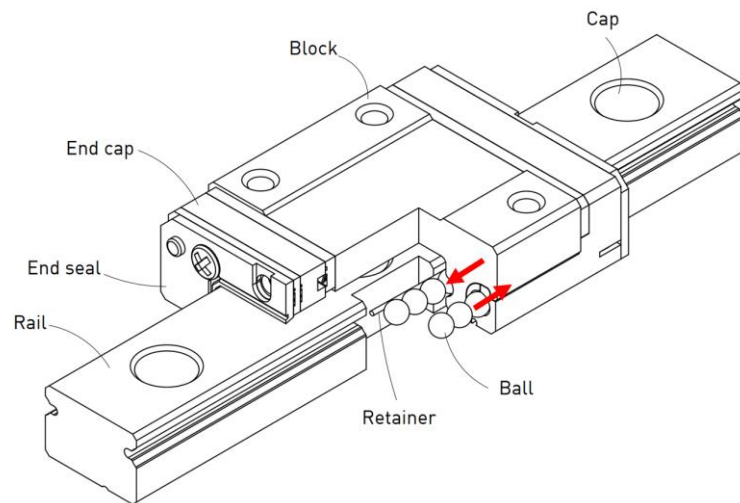


Figure 5.12. Recirculation of balls on a linear bearing [15]

5.2.2. MFG Design

In this section, the design of the MFG to be used in the experiment is discussed. Firstly, the problems faced in the previous experiments [3] are addressed. Then, they are attempted to be solved in the new design. Properties, advantages and weaknesses of the new design are discussed.

5.2.2.1. Problem Statement

Before the designing the MFG, one should have an estimate of the frictional losses at the sliding rails used on links 3 & 5 of the MFG. Similar to the rail cart system, a rough estimate of friction is made with a measurement with a force sensor leading to a frictional force of 2-5 Newtons. This frictional force has been considered to be high for the MFG design since the force delivered to (and retrieved by) the machine is expected to be in the order of 10 Newtons. Therefore, possible reasons of the high friction (such as friction due to the misalignment of the two sliders connected to each of links 3 and 5 and friction due to the preload on sliding rails) are investigated.

Using the experimental setup built in [3], the motion of the MFG with two identical slider-crank mechanisms has also been investigated. There was great resistance around specific angle of the crank, and rotation of slot profile is observed during motion. The joint connecting slot profile to the ground link is supposed to be prismatic. Therefore, a rotation is not expected. Reason of this rotation has been estimated to be non-symmetric dimensions. Recalling that the proposed MFG mechanism in [3] is overconstrained, each dimension must be exact for a smooth operation. Large tolerances in the dimensions would cause some links to deform. However, workmanship errors in the manufacturing and assembly processes are highly possible. Manufacturing with very small dimensional tolerances is expensive and requires high skill. Thus, in this study an option to add a degree of freedom to link 3 & 5 and to be able to remove the over-constrain is implemented.

5.2.2.2. MFG Slider Alignment

Details of the prismatic joint between link 3 and the ground link are depicted in Figure 5.13. In the figure, the rail beds are fixed by bolts using the points A, B, C, and D. The misalignment is exaggerated in the figure. In reality, the misalignment is not visible to eye. One may determine the misalignment by using specific gadgets. If the misalignment is large, by moving link 3 and observing the increase in friction, one may suspect the misalignment.

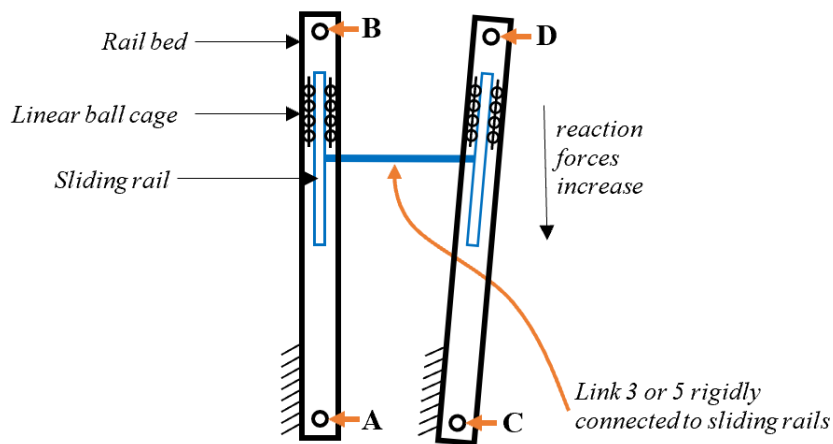


Figure 5.13. Over-constrain problem due to the misalignment

The aforementioned misalignment can be corrected by unfastening the rail beds and fastening them with a specific order. The holes on the rail bed that are drilled for fastening purposes are generally designed with clearance such that one may make alignments during mounting. The mounting procedure used in the experiment is given below.

1. Fasten one of the rail beds tightly and the other one loose.
2. Connect the sliding rails by mounting link 3 (or 5).
3. Slide link 3 (or 5) such that the sliding rails travel through the whole stroke.

4. Fasten tightly one end of the loose connections and repeat step 3 to self-align the second rail.
5. Fasten the remaining loose connection.
6. If there is still high friction on a specific region, loosen the last connection.

5.2.2.3. Reducing the Preload on Sliding Rails

The sliding rails used in this experiment are designed for drawers. A specific preload is applied to the linear ball cages in order to obtain a comfortable friction force. Since this frictional force is large for the MFG application the preload is decreased by deforming the sliding rail. By doing so, the frictional force is reduced below 15 grams which is below the sensitivity of the force sensor.

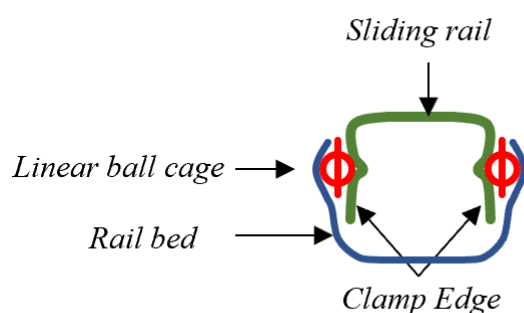


Figure 5.14. Cross-section of sliding rail

The clamping method used to reduce the preload is demonstrated in Figure 5.14. The sliding rail is clamped (bent inwards) from the clamp edges shown in the figure. Excessive clamping will result in rail play in a direction perpendicular to the motion direction and too much clamping would cause the balls to drop during the motion and thus, prevent the motion of the sliding rail.

5.2.2.4. Cylinder in slot joint option for MFG

In order to add an optional rotational freedom to the slot profiles, a strip with pins is connected between the sliding rails (see Figure 5.15). The number of pins on the metal strip is configurable. The pins are fastened to the strip by means of bolts from behind. If only the pin in the middle is mounted, then the slot profile may rotate and translate with respect to the ground link. If more than one pin is used, then rotation of the slot profile with respect to ground is not possible. Thus, the joint will be a prismatic joint.

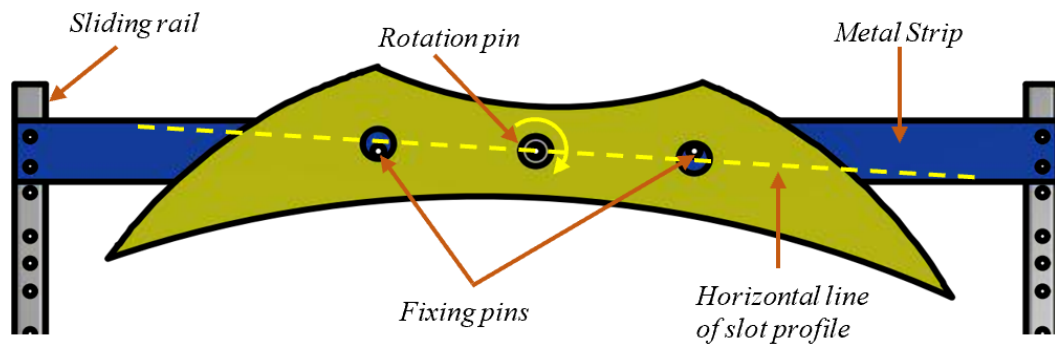


Figure 5.15. Cylinder in slot option to slot profile – ground joint

The metal strip is connected to the sliding rails by means of bolts and nuts. Since the holes on the sliding rails have large clearance, obtaining a rigid connection is quite difficult. One may use metal epoxy to permanently and rigidly connect the two components.

5.2.2.5. Spring Connections

The springs used to store elastic energy in the MFG are connected between the metal strips and the connection components at the top and bottom of the main frame. In this study, the connection components that are readily available from the previous study [3] has been used. Spring displacement from the free length vs spring tension force is shown in Figure 5.16. From the figure, it is obvious that when the spring is at free

length, the spring tension is non-zero. Therefore, the MFG springs are extension springs with initial tensions as well.

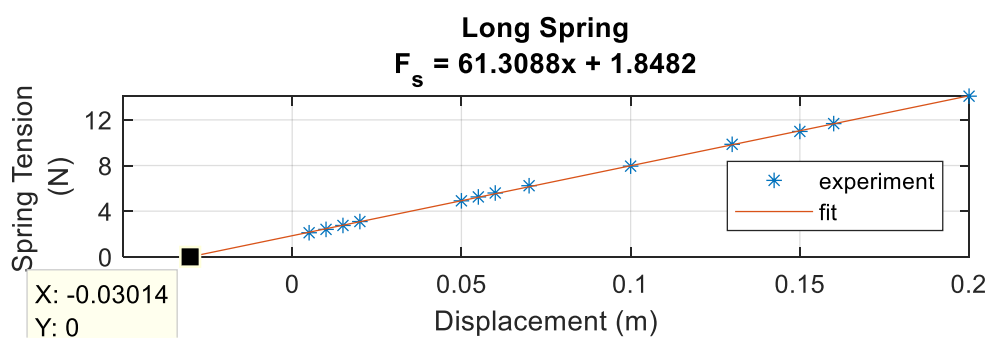


Figure 5.16. Spring coefficient measurement

The design of the MFG allows one to insert multiple springs between link 3 (or 5) and the ground. The endpoints of the MFG springs on the experimental setup are shown in Figure 5.17 and Figure 5.18.



Figure 5.17. MFG spring endpoints on the ground link side

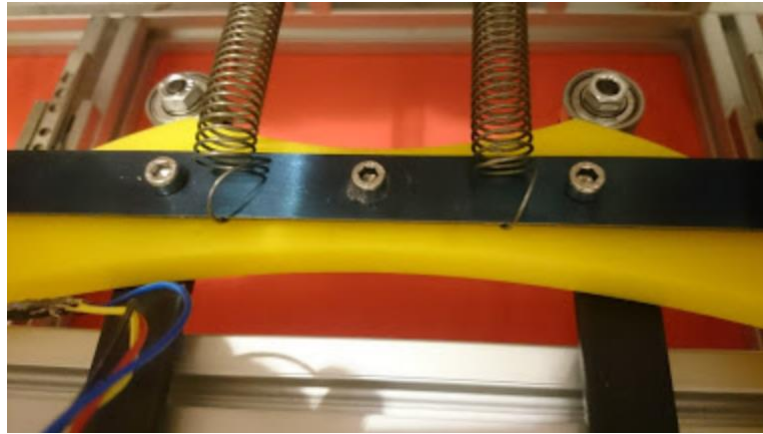


Figure 5.18. MFG spring endpoints on link 3 side

5.3. Experimental Setup Electrical Hardware

Hardware of the experimental setup consisting of the electromechanical components / devices are described in this section.

5.3.1. Problem Statement

In order to actuate the mechanism, an actuator and an equipment to control the actuator are required. One could use benchmark motion control solutions for the experiment. However, they are rather expensive. Furthermore, finding appropriate solutions for all of the design requirements is difficult. Therefore, the motion control system is built by using cheaper components.

In the previous experiment [3], the components of the VEX educational set has been used [18] for control purposes. The components used from the educational set were the ARM microcontroller, the motor driver, a small DC motor with gearbox, and an encoder for angle measurements. These components have not been used due to several reasons that are listed below.

Microcontroller:

- The Integrated Developer Environment (IDE) for the microcontroller board is not configurable. For example, using a motor or encoder other than VEX components is difficult, or not supported.
- Inadequate information about advanced topics like high-frequency real-time control by using the VEX module in web.

Motor:

- The motor has a fragile gearbox and the teeth of the gears are not designed for impact.
- The motor cannot supply the rated torque due to the temperature protection components on the motor. The motor heats up very quickly and the protection component opens the circuit until temperature is below a specified limit.

Driver:

- The driver has low frequency (0.5-2 kHz) PWM output to DC motor and it is unconfigurable.

Encoder:

- It has low resolution (360 ticks per revolution) for precise control.
- It has big size.
- It is not connected to the motor. Hence, additional effort is required to couple the encoder to the motor shaft

Defining the actuator and sensor performance requirements are the main challenges in equipment selection. The MFG design assumes the motion of the machine is perfectly realized with the experimental setup hardware and software. In order to achieve a precise control, already available electro-mechanical components are replaced with better counterparts as much as possible (considering the cost, learning time, and performance).

5.3.2. Electronic Hardware Configuration

The hardware connection diagram is provided in Figure 5.19. The communication methods between the components are shown on the connection lines in the figure.

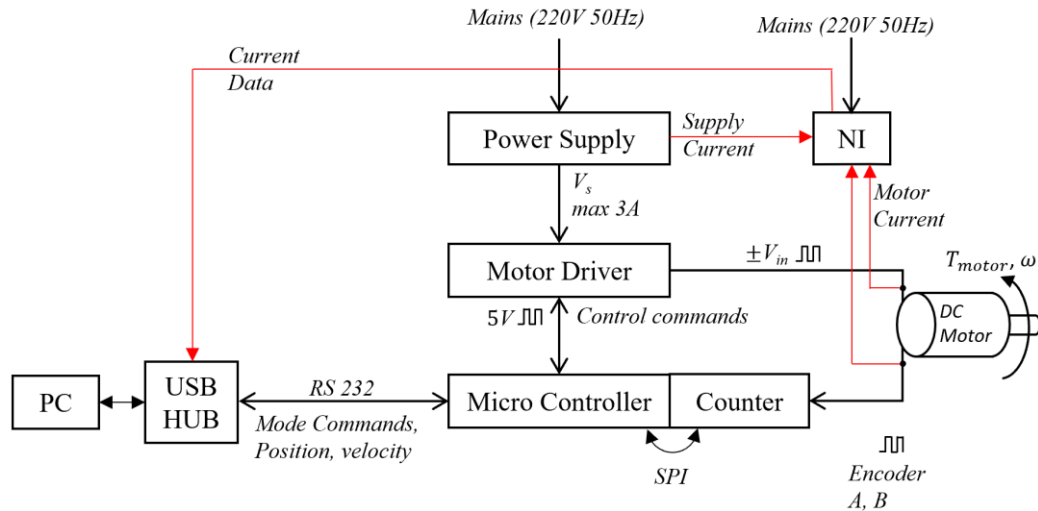


Figure 5.19. Hardware schematics of the experimental setup

The hardware components and their models are listed in Table 5.1. The hardware used for verification purposes and other measurements are also included in the list.

The electronic boards are mounted on a wooden base and (see Figure 5.20).

5.3.3. Motor

The properties of the DC motor used in the experiment are given in Table 5.2. The parameters given in the table should be considered as design parameters. Indeed, the design parameters of the actual product may be different.

The motor is procured as second hand as an assembly (with its encoder and gearbox). After a while the encoder board on the motor stopped working properly. Therefore, a new encoder board has been bought from the Nexus Automation company. DC motor assembly and its components and whole assembly of the motor is given in Figure 5.21.

Table 5.1. Hardware components used in the experiment

Hardware	Model	Company
DC Motor	2342CR012	FAULHABER
Microcontroller	Mega 2560	Arduino
Counter	3 Axis Encoder Counter Arduino Shield	robogaia
Motor Driver	L293N Motor Driver Board	Shenzen Robotlinking Technology Co. Ltd.
Encoder	DC MOTOR 16002 encoder board	Nexus Automation
Power Supply*	GPS-4303	GW INSTEK
PC	Surface Pro 4	Microsoft
Force Sensor	Portable electronic scale	WeiHeng
Current Sensing*	NI9239	National Instruments
	NI cDAQ-9174	

* Equipment used from the previous experiment [3]

The gearbox mounted on the DC motor has a reduction ratio of 1/64 (with planetary gears). The producer company of the gearbox is unknown. An optical incremental encoder with A and B phases is used for the position measurement of the motor shaft. Two OMRON EE-SX 1103 model phototransistors are used for detecting the light transitions while the motor shaft rotates. The encoder disk has 12 wings as can be seen from Figure 5.21. The number of pulses on each revolution can be calculated by using the gear ratio and the number of wings on the encoder disk, yielding

$$\#pulsePerRev = GearRatio \cdot \#Wings \cdot 4 \quad (5.3)$$

The result is multiplied by 4 in order to include two channels and for each wing, there are two transitions which are the rising edge and the falling edge. The number of pulses per revolution for this motor is 3072.

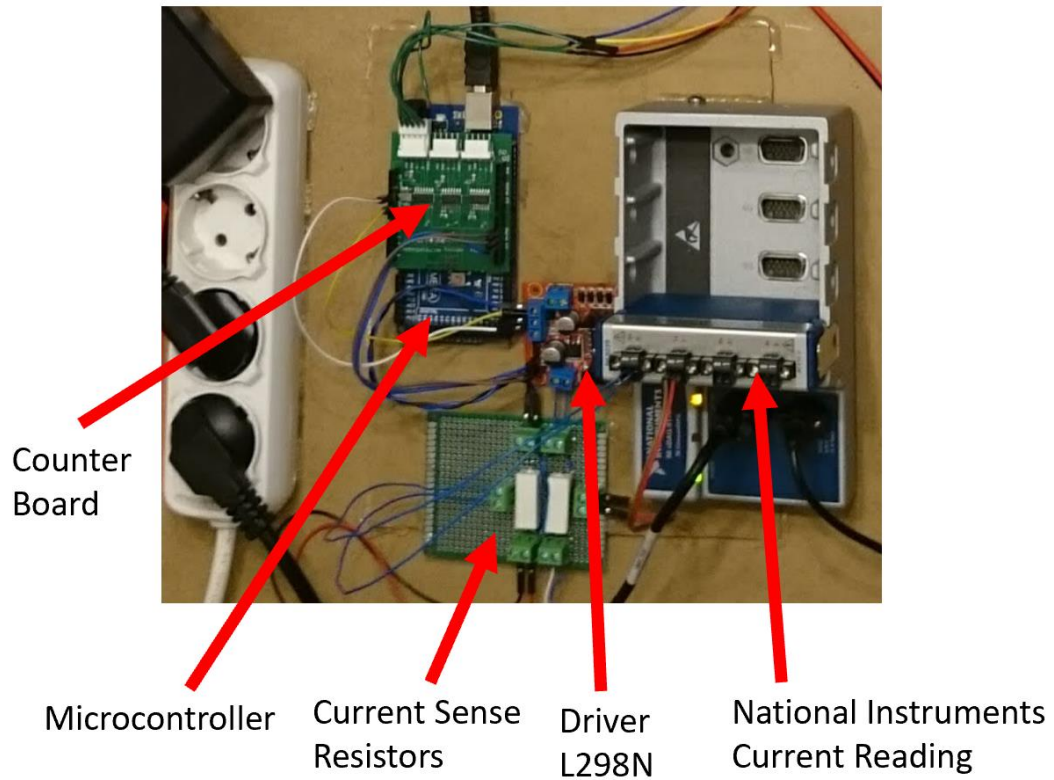


Figure 5.20. Electronic hardware of the experimental setup

Table 5.2. DC motor important properties without considering gearbox [11]

Parameter	Value	Unit
Nominal Voltage	12	V
No-load speed	8100	rpm
No-load current	0.075	A
Friction torque	1	mNm
Back-EMF constant	0.0134	V/(rad/s)
Torque constant	0.0134	Nm/A
Rotor inertia	$5.7 \cdot 10^{-7}$	$\text{kg} \cdot \text{m}^2$
Rotor inductance	65*	μH
Terminal Resistance	1.9	Ω
Rated Current	1.5	A
Rated Torque	17	mNm
Rated Speed	6090	rpm

* Measured in 1kHz

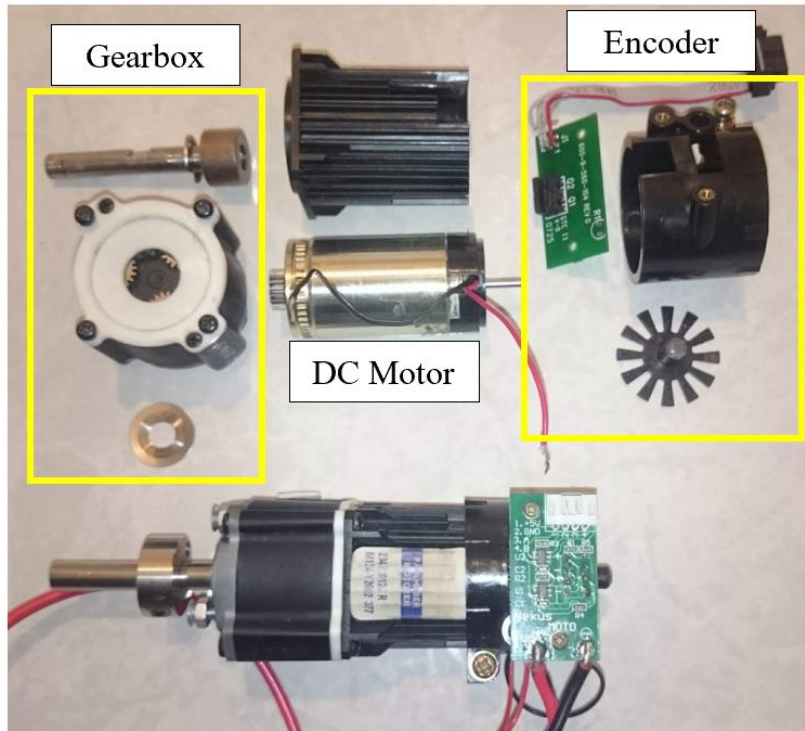


Figure 5.21. DC Motor assembly with its components

5.3.4. DC Motor Driver

The current output of a microcontroller is generally not enough to drive a DC motors on its own. The motor driver used in this experiment acquires signals from the microcontroller to transfer power from the power supply to the motor. The input signals are modulated in order to achieve an adjustable voltage output to the motor.

L298N integrated circuit is a well known and widely available DC motor driver [19]. It can support continuous output current of 2A without a heatsink connection (which is above the current limitation of the DC motor). Maximum switching frequency is specified as 40 kHz, which is higher than the audible frequency. A 20 kHz switching is used in the experiment.

The motor driver circuit offers different options for driving. During the ON time of the pulse width modulated signal (PWM), the driver outputs the voltage of power supply in the direction commanded by the microcontroller. During the OFF time, the available options of driving method are listed below.

- Output may be adjusted to be the negative of the power supply during the ON time.
- Output may be 0 V, which is equivalent to shorting the terminals of the motor (fast motor stop in the datasheet [19]).
- The remaining current flows to the power supply from the flyback diodes and the motor runs as if its terminals are not connected (free running motor stop in the datasheet [19]).

These options are investigated in more detail in the DC chopper section of the power electronic books [20]. In the experimental study, the second option is selected due to its linear behavior in the motor duty-speed tests. Results of duty-speed tests are given in Figure 5.22.

Since the motor terminals are shorted during the OFF-time, the motor back emf reduces the current and acts as a braking mechanism. This is why this option is called as fast stop type. If this braking torque is not enough, the polarity of input voltage is reversed by the controller to acquire required torque. Therefore, the braking method used in the experiment is of the plugging type.

The H bridge circuit used to drive the DC motor is shown in Figure 5.23. In the figure, there are 4 switches, (namely Q1, Q2, Q3, and Q4) which are opened or closed according to the signal received from the microcontroller and the logic inside the driver. Due to the nature of the switches, some power loss occurs in the driver depending on the switching frequency and the current passing through the switches.

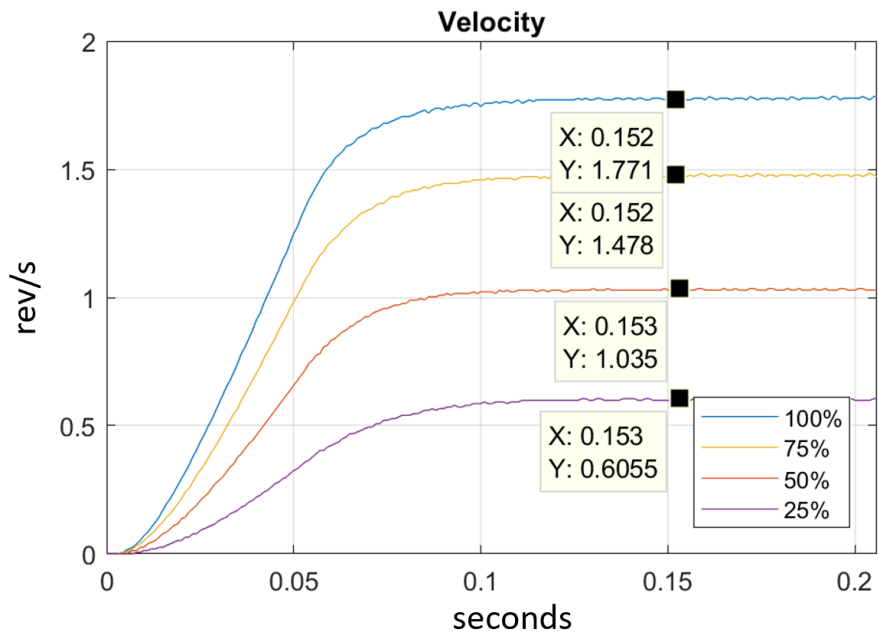


Figure 5.22. DC Motor speed-time plot for various duty cycles (in percent)

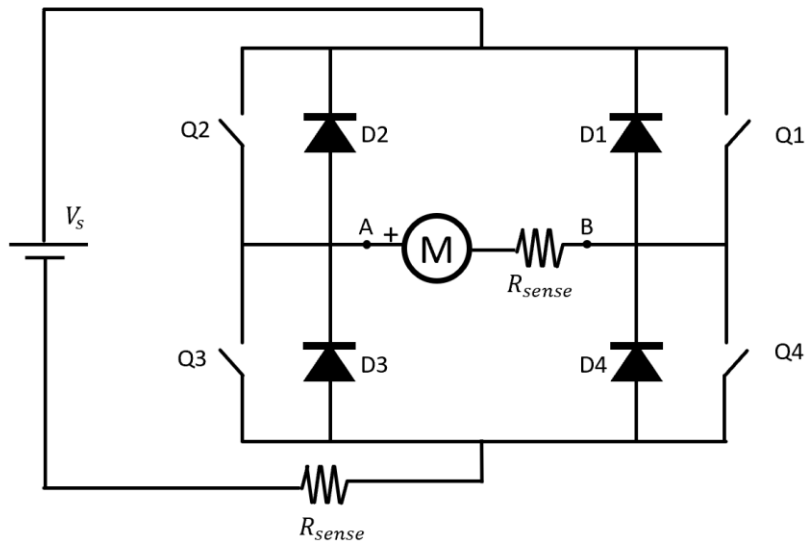


Figure 5.23. H Bridge with Flyback diodes

5.3.5. Current Sensing

The currents are measured by using the National Instruments analog input module (NI9239). In order to calculate the currents, the potential drop across the sense resistors are read by the hardware and sent to the PC. The module has built in anti-aliasing filter. Thus, an additional filter is not required. In this study, the current drawn by the motor and the current supplied by the power supply are measured.

5.3.6. Microcontroller

Arduino may be one of the most popular electronics platforms throughout the world over the decade. From hobbyists to engineers, from starters to professionals it has a very large community and it has an open source database [21]. Therefore, it is easy to solve the problems in this study by using Arduino since most of them are already solved and published on the internet.

In this study, Arduino Mega board is used since it can support real-time control up to 1 kHz with its 16 MHz internal clock. It can generate PWM signals up to 80 kHz frequency, with a 1/200 duty resolution. The resolution increases as the PWM frequency decreases, since the ratio of frequency to duty resolution is equal to the internal clock rate of the board.

The board supports reading analog data up to 10 bits resolution. Higher resolution data can be obtained by connecting an extra hardware that can communicate with Arduino by using either SPI, I2C or serial communication protocols. It can communicate with the encoder board with its built in SPI interface, and it can communicate with the PC via the USB port using serial communication.

5.4. Experimental Setup Software

The software algorithms designed for conducting the experiments are described in this section.

5.4.1. Problem Statement

The design of the MFG assumes the motion profile is perfectly realized. There are several difficulties on the software side. The control algorithm drives the actuator according to the incremental optical encoder data. The encoder data, by nature has quantization errors. Since the velocity of the motor is also controlled, a good estimation algorithm is required to achieve precise control. In addition to state estimation, the controller should have a high bandwidth to react to sudden load changes coming from the machine. A good digital control practice requires precise sampling time. Therefore, real-time control is required. While doing all these, the microcontroller has to send experimental data to the PC. The main challenges stated above are summarized below.

- Precise estimation of position and velocity from the incremental optical encoder.
- Controller design.
- Precise sampling time for control and estimation.
- High bandwidth.
- Collect experimental data on the PC.

5.4.2. Real-time operation

Performances of running the control and estimation algorithms on the PC and on the microcontroller are compared; and the second option is selected (due to its higher bandwidth and eligibility to control in hard real-time). Controller sampling frequency is selected as 1 kHz. Encoder position is measured at the same rate. At the end of the calculations of the current period, the microprocessor waits for the sampling period to complete and then proceeds to the next time step. If the current calculations take longer than the sampling period, then the microcontroller stops the actuator command, lights up the internal LED (light emitting diode) of the board to indicate that real-time control has not been achieved. Then, the microcontroller goes into an infinite loop until the next restart of the microcontroller.

Precise timing is achieved by using the internal clock of the microcontroller board which has a 16 MHz.

5.4.3. Data transfer

The experimental data are collected on the microcontroller. Due to its very low dynamic memory, the option of collecting data to an external memory (like external SD card or external flash memory) during the experiment and sending it slowly to the PC when the motion is finished is compared with the option of sending data directly to the PC during the motion using serial connection with a high data transfer rate. The second option is selected since the data transfer to PC was more stable and experimental data size to be sent in each period was small enough. Data packet contents and size to be sent from microcontroller to the PC are given in Table 5.3. Note that for data transfer, only the size is important. Therefore, during the experiment, other variables, such as controller error or time duration of calculations, can be replaced with the parameters in the data type for observation.

Table 5.3. Data packet contents to be sent at each period

Parameter	Units	Data Type	Size (Bits)
Motor shaft acceleration	1/3072 rev/s ²	float	32
Reserved	-	uint16	16
Control command	PWM%	uint16	16
Motor shaft position	1/3072 rev	float	32
Motor shaft velocity	1/3072 rev/s	float	32
		TOTAL	128

In order to send 128 bits using 1 kHz and allowing time for other calculations, 256000 baud/sec data transfer rate has been selected. With this speed, the time spent for only sending the data is calculated as 625 μ s. Note that for 1 kHz, time allocated to the microcontroller to finish all of its tasks is 1 ms. Thus, most of the time is spent on communication. One may refer to [22] for detailed information on data transfer with

RS232 serial protocol. This data transfer rate was tested with MATLAB and the Python programming languages on platform Windows 10; and it was observed that only Python was successful. Therefore, the data transfer has been realized by using Python script.

Since the operating system of the PC is not real-time, commands sent to the microcontroller may have delays. This is not acceptable due to the implemented real-time design explained in 5.4.2. Therefore, the PC sends commands only seldomly (for instance it sends commands for mode and parameter changes). Thus, closed-loop data transfer is not performed between PC and the microcontroller as a result.

5.4.4. Position & Velocity Estimation

The encoder data is used for position measurement since its resolution (360/3072 degrees) has been considered to be acceptable. The simplest way to calculate velocity from the encoder data is to apply backwards Euler differentiation via the equation

$$\hat{\omega}(kT) = \frac{2\pi}{P} \frac{N(kT) - N(kT - 1)}{T} \quad (5.4)$$

where T corresponds to the sampling period of encoder data, P corresponds to the number of encoder lines per revolution, which is 3072 for this experiment, and N corresponds to the encoder count. The maximum error in this approach is calculated in [23] as:

$$e_{max} = \frac{1}{PT} \text{ (rev/s)} \quad (5.5)$$

Since the sampling time is small, maximum error in this experiment has been calculated as 0.3255 rev/s. It is obvious that the control performance will be poor for speeds up to 2 rev/s. Therefore, Tustin method given in [24] is applied in order to have smooth velocity profile, i.e.,

$$G_s(z) = \frac{s}{\tau s + 1} \Big|_{s=\frac{2z-1}{Tz+1}} = \frac{z - 1}{\left(\tau + \frac{T}{2}\right)z - \left(\tau - \frac{T}{2}\right)} \quad (5.6)$$

Note that this method has no steady state error at constant speed. The error can be calculated by applying the final value theorem to the transfer function given in equation (5.6) with a ramp input.

As the time constant increases, the velocity estimation will be smoother but it will have more delay, where both will reduce control performance. By simulation and motor tests 100 ms time constant has been found acceptable. Performances of the Tustin Method and the backward Euler differentiation have been compared by using the data collected with the DC motor (see Figure 5.24). During the test, the DC motor was driven with 100% duty for 5 seconds and then with 0% duty for 10 seconds. The motor reaches to its maximum no load speed around 0.04 seconds. Notice the delay in the Tustin method. Note that the jump magnitude of the Euler method is around 0.33 which is similar to the error value calculated by using equation (5.5).

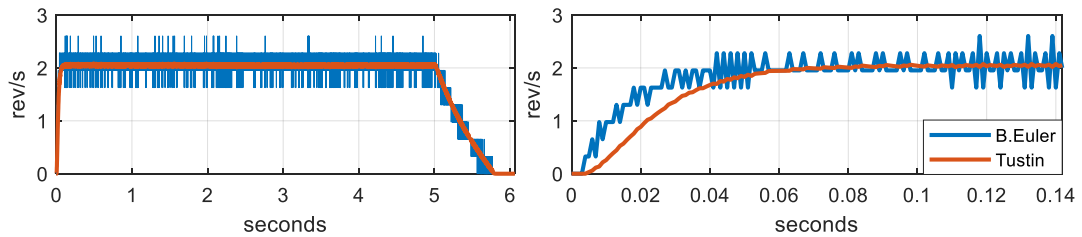


Figure 5.24. Speed estimator performance comparison of the Tustin and Backward Euler Methods (right plot is the zoomed version of the left one)

For the derivative control action, acceleration is also estimated using the same method. The test results from the same experiment are shown in Figure 5.25.

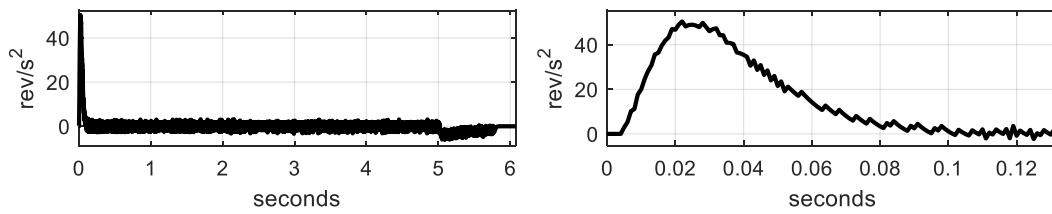


Figure 5.25. Acceleration estimation performance using the Tustin method (right plot is the zoomed version of the left one)

5.4.5. Control algorithm

In the microcontroller, PI control has been implemented. The system block diagram is given in Figure 5.26. As the DC motor can apply limited torque, there are saturation blocks at the end of integral and control sum terms. In the figure, θ_{enc} refers to the encoder position measurement and $\hat{\omega}$ is the angular speed estimation of the motor output shaft. ω_{ref} , on the other hand, corresponds to the reference angular speed.

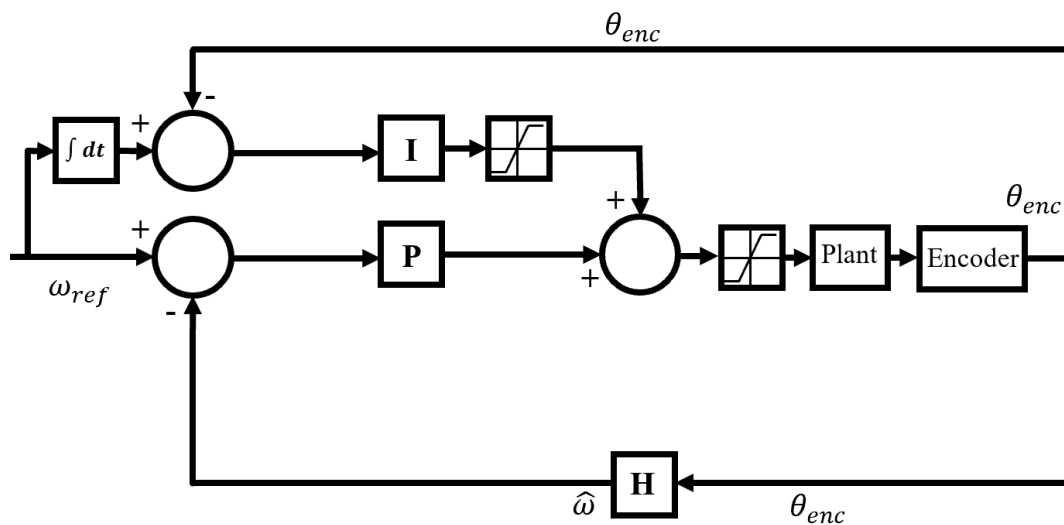


Figure 5.26. The control system block diagram

P (proportional) and I (integral) parameters are experimentally determined. Since the acceleration measurement has delay and high noise, the control performance with D (derivative) action was not acceptable. Therefore, D action has not been used in the

control algorithm. The experimental results with these two parameters were satisfying. The velocity percent error results of the experiments will be discussed in Section 6.4.

5.4.6. LabVIEW Current Reading

In order to read the current from the National Instruments hardware, LabVIEW software is used. The data rate of the reading is set as close as possible to the control rate (1 kHz), which is 1.612 kHz. Due to the limitation of the hardware, the same sampling rate could not be achieved. The obtained current data has been down-sampled to 1 kHz in this study.

The block diagram of the software is given in Figure 5.27. The software is converted to an .exe application to be called from the MATLAB script via the system commands. The .exe application accepts the reading time as the input. As soon as it is called, it begins reading the current values and writes to Excel file to be read and be evaluated by the MATLAB script.

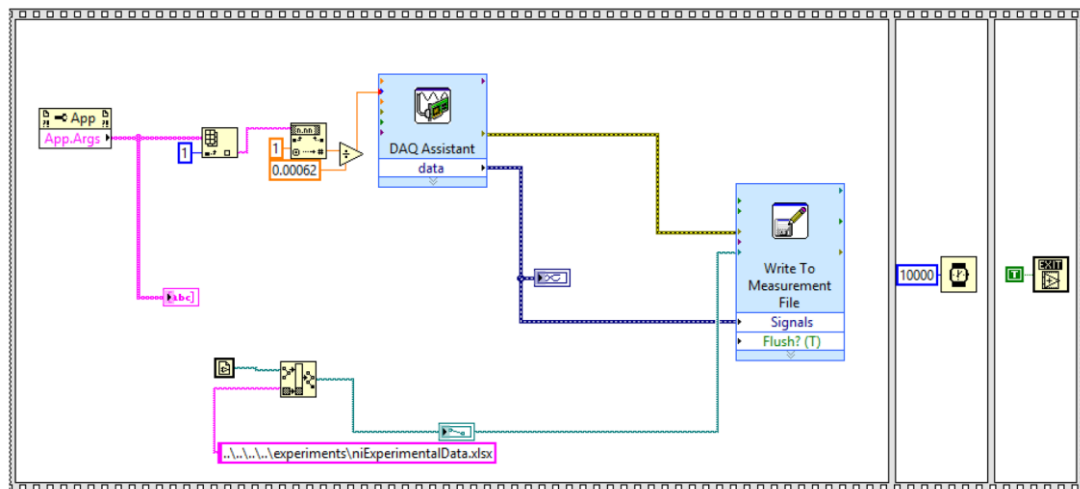


Figure 5.27. LabVIEW software block diagram

5.4.7. Software Use Case

The actuator and the data collection are commanded from the PC. The experimental setup software consists of MATLAB, Python, LabVIEW and Arduino. The experiment conductor configures the mission parameters on the MATLAB script and then runs the code. The rest is handled by the script, which will be referred as the main script from now on.

The mission parameters consist of the duration of experiment, the mode of operation and the extra parameters that belong to the mode. The modes of the software are given in Table 5.4. Only the modes 2 to 5 are implemented in the main script. The other modes are implemented for safety and stability and are used in the Python script.

Table 5.4. Software modes of the microprocessor

MODE	Definition	Extra Parameters & Data Types
1	Full Stop (0% Duty)	None
2	Full Speed (100% Duty)	None
3	PWM Mode	PWM% (int16)
4	Position Control	P (float32), I (float32), D(float32), reference position in unit encoder ticks (float32)
5	Velocity Control	P (float32), I (float32), D(float32), reference velocity in unit encoder ticks (float32)
16	Start Logging	None
17	Stop Logging	None

After the user runs the main script, firstly the current reading application is called. Then, while the application is running, the mission parameters are sent to the Python script by calling it via system command. The Python script and the current reading application run at the same time. The main script waits for both tasks to finish.

The Python script restarts the microprocessor and then starts the communication. The algorithm for the Python script is summarized below.

1. Read the mission parameters.
2. Start communication with the microprocessor.
3. Start microprocessor logging.
4. Start the mission by sending the microprocessor the mode and the extra parameters.
5. Read and log the experimental data received from the microprocessor and count the received packets.
6. Once the number of received packets is equal to the number of packets expected in the simulation time, stop logging.
7. Stop motor.
8. Save the logged data to a file.

The Python script prints a message in each step, in order to monitor the success of the process. Once the Python script and the current reading tasks are finished, the main script reads the experimental data and plots the results.

CHAPTER 6

EXPERIMENTAL CASE STUDY

6.1. Introduction

In this chapter, experimental performance improvement of DC motors driving a machine with the existence of an MFG is realized. The MFG used is the one that is designed in Chapter 4 and implemented physically in Chapter 5. Various experiments are conducted with two different crankshaft speeds. Performance of the MFG, when link 3 and link 5 are connected to ground link with cylinder in slot joint, is compared with the performance when there is a prismatic joint between these links.

Control performance in setting speed control of the motor shaft is investigated. Power and energy consumptions of the cases are obtained experimentally. The results are compared with the results of the simulations. Performance of the MFG design is assessed by using the performance measures defined in Section 3.3.2. New performance measurement indices are defined.

6.2. Description of Test Cases

In this study, experiments are conducted for six different configurations and two different motor shaft speed. The cases are classified with respect to three criteria that are explained below.

- **Loading:** Machine is either loaded with a spring between links 2 & 4 (see Figure 4.1 and Figure 5.10) or not. When the machine is not loaded, the motor does work against the Coulomb and viscous friction at the joints and against the MFG forces and moments (when applied).
- **Joint Type:** The joint between link 3 and link 1 (the ground link), and the joint between link 5 and link 1 is either a cylinder in slot joint (Cs) or a prismatic

joints (P) (see Figure 1.1 for the link numbering). For the physical construction of the aforementioned joints see Appendix A.

- **Application of MFG:** Machine may be operated with or without the MFG.

The six cases considered in this study are given in Table 6.1.

Table 6.1. Descriptions of the six different cases

Case #	Loading	Joint Type	Application of MFG
1	Yes	N/A	No
2	No	P	Yes
3	No	Cs	Yes
4	No	N/A	No
5	Yes	P	Yes
6	Yes	Cs	Yes

N/A: Not Applicable

P: Link 3 – Link 1 and Link 5 – Link 1 joints are prismatic joint

Cs: Link 3 – Link 1 and Link 5 – Link 1 joints are cylinder in slot joint

In Chapter 4, the MFG has been designed to eliminate the effect of the spring load on the motor. A perfect MFG would apply appropriate forces on links 2 and 4 such that the effect of the spring load force is cancelled. Therefore, Cases 1, 2 and 3 should have similar power consumption profiles. Note that in the first three cases, there exists either the load or the MFG forces. See Figure 4.1 for the external forces on the machine.

On the other hand, since the MFG forces should cancel the effect of the load forces, when the load and the MFG are connected to the machine, the system would behave as the machine without the load forces. Therefore, cases 4, 5 and 6 should have similar power consumption profiles as well.

If the designed mechanical components are manufactured and installed perfectly on the system, the prismatic joint and cylinder in slot configurations of the MFG's should

have the same power consumption profile. Otherwise, the prismatic joint configuration expected to consume more power.

The aforementioned six experimental cases are conducted with two different motor shaft speeds (ω), which are 0.1 rev/s and 1 rev/s. Since the spring forces are not dependent on the shaft speed and the inertial forces of the machine are neglected in the MFG design, the same design can be used with two different speeds. However, since the inertial forces and the frictional forces increase with higher motor shaft speeds, a decrease in performance is expected. Recall from Chapter 4 that, the load forces are selected such that the motor can hardly drive the mechanism at 0.1 rev/s. It is obvious that the motor cannot drive the system at higher speeds, as the frictional and the inertial forces increase and the torque output of the motor decreases. The main objective of the experiments with the higher speed of 1 rev/s is to demonstrate that the motor can also drive the system at 1 rev/s with the aid of the MFG.

6.3. Initial Conditions Associated with the Experiments

The initial values of the crank angle (θ) and the power supply voltage (V_s) are given in Table 6.2.

Table 6.2. Initial conditions associated with the six experimental cases

Case #	Initial Crank Angle (rad)	Power Supply Voltage (V)
1	π	16
2	0	17
3	0	17
4	π	16
5	π	16
6	π	16

The spring load forces try to pull links 2 & 4 closer to each other. Thus, at the minimum stroke, which is when s_2 is minimum, the system is at the stable equilibrium state. Therefore, the initial crank angle is selected as π rad for the Cases 1, 4, 5 and

6. Since the MFG forces effectively eliminate the effects of the spring forces, π is the unstable equilibrium for Cases 2 and 3. In order to prevent injury or damage to the system, the initial crank angles of these cases are selected as 0 rad.

The angular speed of the motor shaft (ω) is constant, and the direction of it is counter-clockwise (i.e., the direction is parallel to +z axis of the ground link reference frame shown in Figure 4.1). Since ω is constant, in the cases other than Case 2 and Case 3, the sliders reach to the maximum stroke at $t = T/2$ seconds and then return to the maximum stroke at $t = T$, however, in cases 2 and 3, the sliders reach to minimum stroke at $t = T/2$ seconds and then return to minimum stroke at $t = T$, where the period T is equal to the time it takes the motor shaft to complete one revolution.

The duration of the experiments is one period (i.e., $T=10$ s) when $\omega = 0.1$ rev/s, and three periods when $\omega = 1$ rev/s. Longer durations are not selected so that the motor, or its driver are not overheated (since they are already operated with harsher conditions compared to their rated limits).

In the experiments for the Cases 2 and 3, the motor could not drive the system with a 16 V power supply input. In order to conduct these experiments successfully, the voltage of the power supply has been increased to 17 V.

In all of the experiments, the same control parameters have been used. The values of the controller parameters are given in Table 6.3.

Table 6.3. Controller Parameters

P	0.5
I	5

A photograph of the experimental setup for the 2nd case is shown in Figure 6.1. A photograph of the setup for Case 4 is shown in Figure 6.2. Note that the springs connected to the MFG are unmounted; and link 3 and link 5 are pulled to a location where the mechanism does not contact the MFG links during the motion.

6.4. Control Performance Analysis of the MFG Design

Control performance of the MFG is assessed via the percent error of shaft rotational speed given by:

$$\omega_{err}(i, \omega_{ref}) = \frac{\omega - \omega_{ref}}{\omega_{ref}} \cdot 100 \quad (6.1)$$

where i denotes the case number, ω_{ref} denotes the reference speed and ω is the measured rotational speed of the shaft.

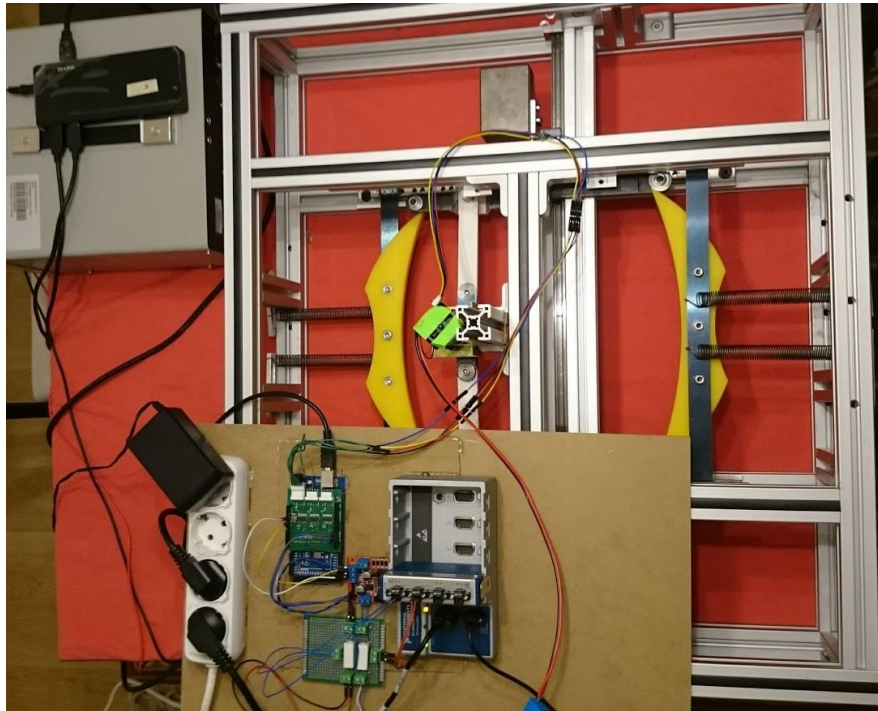


Figure 6.1. Experimental setup for Case 2

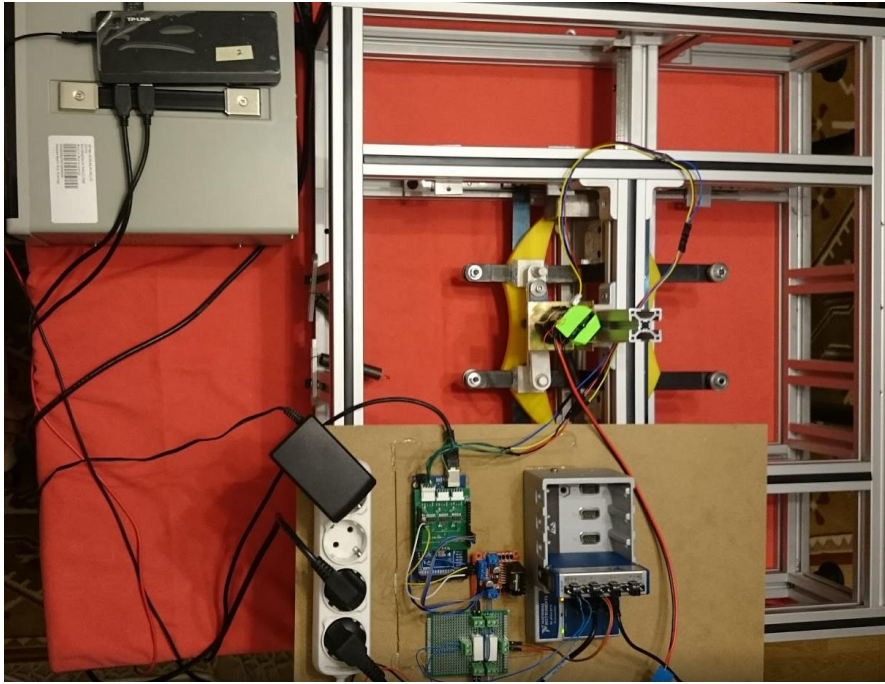


Figure 6.2. Experimental setup for Case 4

Percent errors of motor shaft speeds for the six cases and for the two reference speeds are given in Figure 6.3. In the right column of the figure, corresponding to the 1 rev/s, the results of the last period are given, such that initial transient errors of the cases are not seen. However, in the left column, corresponding to the 0.1 rev/s, the transient errors may be seen. These transient errors are included in the calculations to be given in the following sections. In Figure 6.4, controller duties for each case and for each reference speed are given.

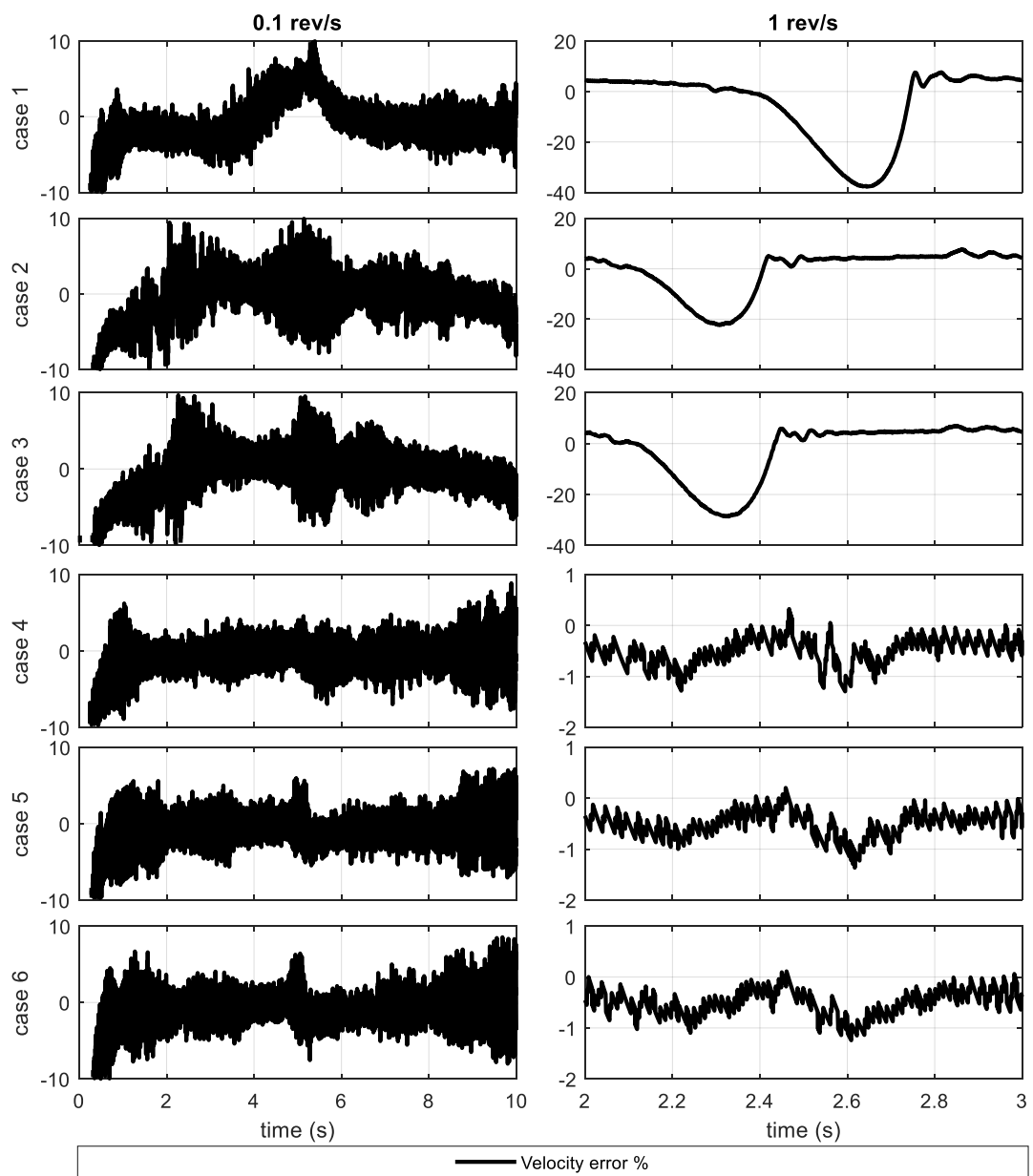


Figure 6.3. Percent error of motor shaft rotational speed

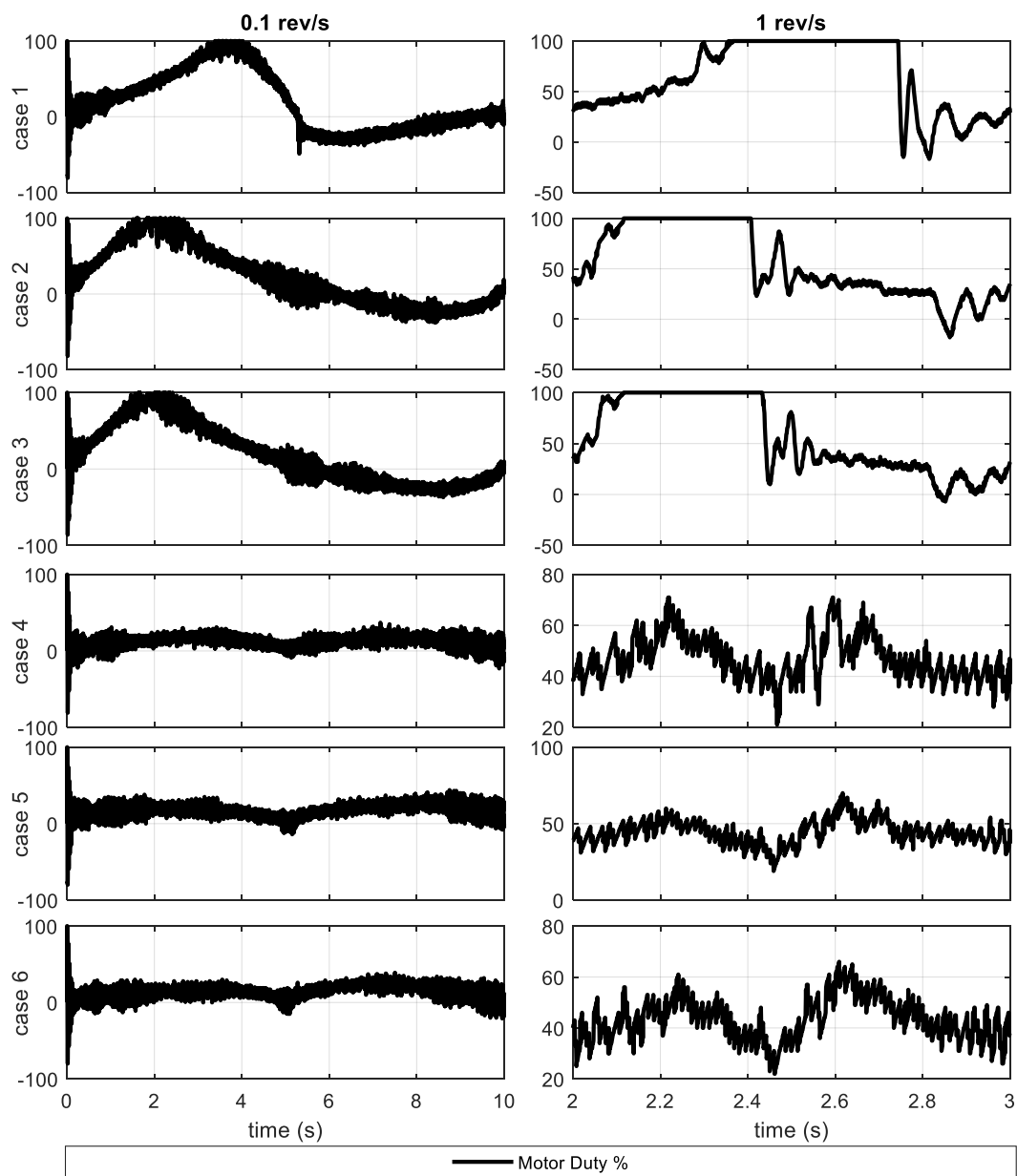


Figure 6.4. Controller Duty for each case and for each reference speed

Referring to Figure 6.3, it is obvious that control could not be established in the first three cases when the reference speed is 1 rev/s. From Figure 6.4, it can be seen that the control command is saturated, thus the maximum torque of the motor was not sufficient.

From Figure 6.3, it can be seen that when the reference speed is 0.1 rev/s, percent errors for all cases are below 10%. When the reference is 1 rev/s, the percent errors are below 1%. The difference between the two reference speeds is mainly due to the quantization errors of the encoder measurements, as explained in Section 5.4.4. It could be improved by using better estimation algorithms or by using an encoder with higher resolution.

Although PI control is used, there exists some steady-state error in all cases. This is more apparent in Cases 4 to 6 in the right column of the figure. This might be due to the control method (see Figure 5.26), where P is multiplied by the velocity estimation and I is multiplied by the encoder error measurement. The error bias would not change by increasing I. Thus, the bias might be due to the discrepancy between the measurements and the velocity estimation.

In the first three cases, with the 0.1 rev/s reference speed, there is a small jump in the error at the middle of the plots. Around that time, the direction of the motor torque changes due to the spring forces in Case 1 and the MFG forces in Cases 2 and 3. The jumps happen at the minimum and the maximum strokes, when the crank angle is either π or 0 (when $t = T/2$), with a noticeable sound. The reason of this behavior is the backlash in the gearbox. Note that in the other experiments and reference speeds this behavior is not observed since the spring load is either balanced, or does not exist.

In the first three cases of the control duty plot with 0.1 rev/s reference speed, it can be observed that the duty plot of Case 1 is the reverse (in the sense of time reference) of cases 2 and 3, starting from the half of the period. This is expected since the direction of forces are opposite for the MFG and the load, and the starting position is shifted

due to initial conditions given in Table 6.2. This time shift is demonstrated further in Section 6.5.3.

6.5. Power Analysis for the MFG

In the following subsections, the motor power output calculations are given. The experimentally calculated motor power outputs are compared with the simulations. Finally, the results of the test cases are compared with each other.

6.5.1. Motor Power Consumption Calculation of the Experiments

In this section, the motor output power corresponding to each experiment is calculated using the motor current and the shaft speed measurements. The DC motor model given in Section 3.2.2 is used here with the values of the components in Figure 6.5. The nodes A and B in the figure are connected to the output ports of the driver. See 5.3.4 for the driver schematics.

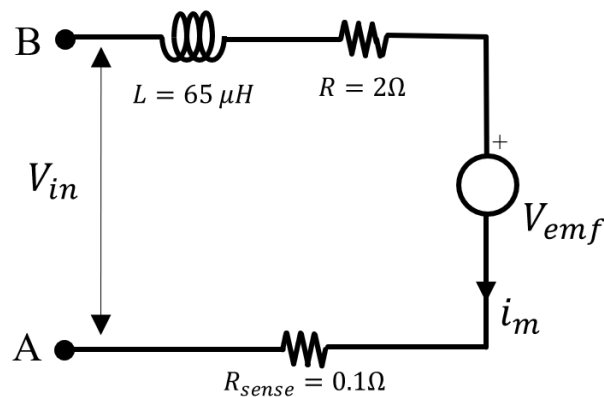


Figure 6.5. DC Motor model used in experimental calculations

The back emf constant of the motor is determined experimentally by connecting A and B nodes in Figure 6.5 to the power supply which provides 12 V constant voltage. The current drawn is read from the power supply current display. Then, the speed of the motor is measured with the microcontroller. Later, the back emf constant (k_E) is calculated by using the following equation.

$$k_E = \frac{V_{in} - i_m R}{\omega} = \frac{12V - 0.05A \cdot 2\Omega}{2 \cdot 2\pi \text{ rad/s}} = 0.947V/(\text{rad/s})^{-1} \quad (6.2)$$

The sense resistor was not used in the experiment. Therefore, it is not seen in equation (6.2).

Note that when SI units are used in the description of the back emf constant, the back emf constant and the torque constant are the same as given in equation (3.17). If one neglects the losses on the motor given with equation (3.18), then the output torque of the motor can be estimated by multiplying the current with the torque constant given in equation (3.20). Therefore, the output power of the motor can be calculated by using the motor current measurement, the speed measurement, and the back emf constant measurement as follows.

$$P_{motor}^e = T_{motor} \omega \approx (k_E i_m) \omega \quad (6.3)$$

where the superscript e in P_{motor}^e is used to denote that this value is an experimental value. The notation P_{motor} , on the other hand, is used for the simulation results of the motor power.

By using the dynamic force analysis of the slider-crank mechanism with the assumptions given in Section 4.2.5, the required motor torque T_{motor} is calculated using the forces acting on links 2 and 4. The torque is multiplied by the reference speed in order to obtain the motor power, i.e.,

$$P_{motor} = T_{motor} \omega_{ref} \quad (6.4)$$

The forces and their application points are given in Figure 4.1. Recall that the friction forces acting on links 2 & 4 are taken into account, which are assumed to be constant in magnitude. All of the inertial forces and moments are also considered in the analyses. The MFG forces on links 2 and 4 are calculated by the dynamic analysis of the MFG as described in Section 2.7. The same slot profile is used for both of the reference speeds.

6.5.2. Comparison of the Experimental Motor Power with the Motor Power Obtained from the Simulations

The comparison of the experimental motor power with the motor power obtained from the simulations are shown in Figure 6.6. In order to smooth out the noise, the experimental results are filtered with moving average filter with 101 points.

For the motor power simulations, the notation $P_{motor}(i, \omega_{ref})$ is used, where i refers to the case number and ω_{ref} refers to the reference speed of the motor shaft. For the experimental calculations of the motor power, the notation $P_{motor}^e(i, \omega_{ref})$ is used.

In Figure 6.6, it is observed that the difference in the simulation and experimental results is minimum in $P_{motor}^e(4,0.1)$ and $P_{motor}(4,0.1)$. Recall that in Case 4, the MFG and the load spring are not mounted in the system. Since the reference speed is low, the reaction forces acting on the joints are low as well. Therefore, the Coulomb friction acting on the joints is negligible. Hence, it can be concluded that the constant friction value is good enough to model the machine at low speeds.

From Figure 6.6, it is also observed that in Case 4 at 1 rev/s, the simulation results closely match the experimental results. This shows that the inertial forces and moments are modeled correctly. The small difference in this case is due to the losses at the joints.

Note that, $P_{motor}^e(1,1)$, $P_{motor}^e(2,1)$ and $P_{motor}^e(3,1)$ should not be taken into account, since the motor could not drive the mechanism at the reference speed.

In the Case 1 with 0.1 rev/s reference speed, recall that the spring forces increase and reach to a maximum at the time $t = 5$ s. As the spring forces increase, so does the frictional forces and moments. Thus, the discrepancy between the simulation and experimental results increases, which is seen in the figure as expected. The same comment also applies to Cases 2 and 3.

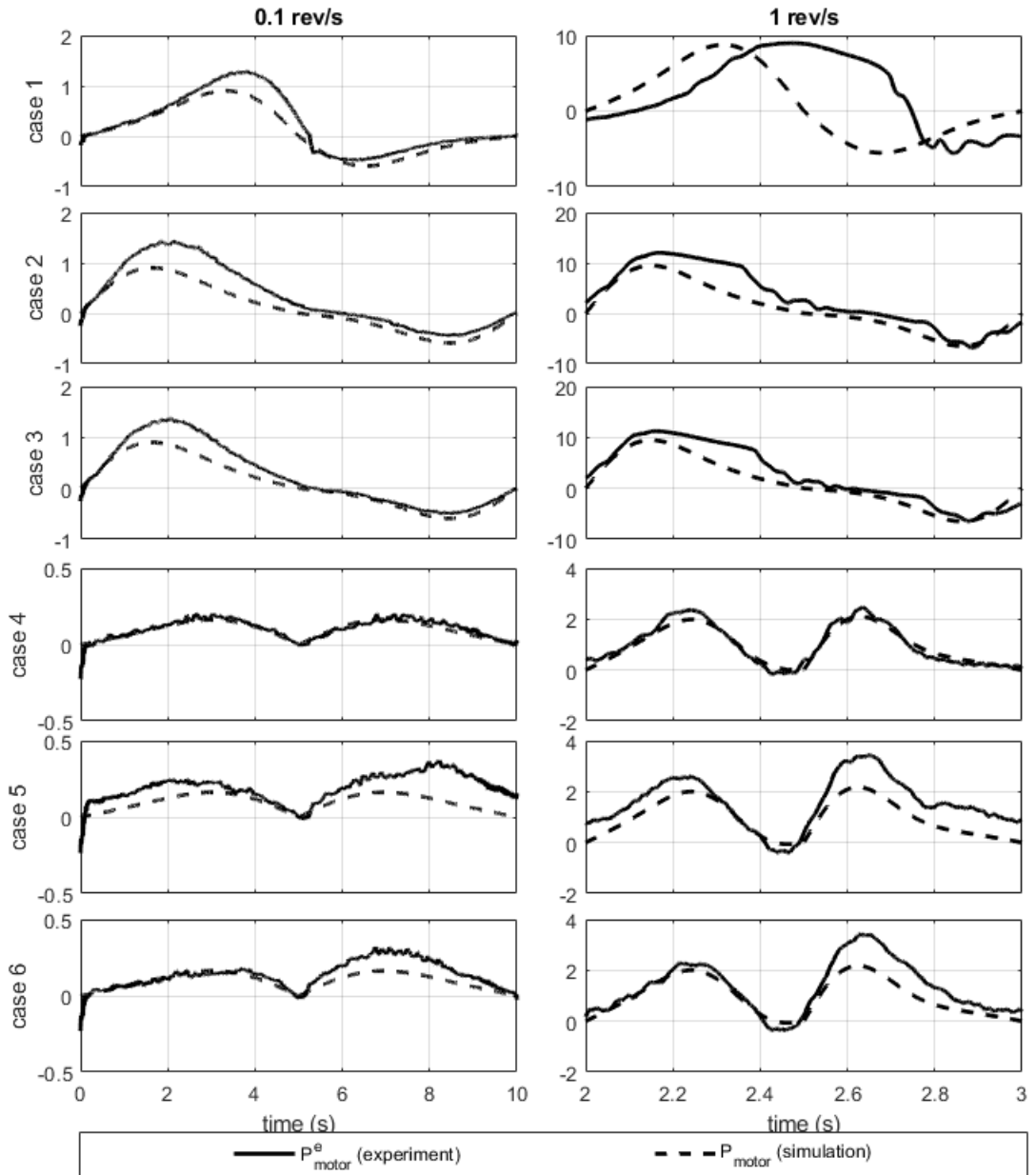


Figure 6.6. Motor output power of the experiments and the simulations

6.5.3. Comparison of Experimental Results with Each Other

In order to compare motor power output results of Cases 1, 2 and 3, the plots corresponding to Cases 2 and 3 must be time-shifted. This is due to the shifted initial conditions given in Table 6.2 and due to the fact that the MFG forces are in reverse direction of the spring forces. The modification of Cases 2 and 3 plots are made such that the new time starts with $t = T/2 + t_s$ of the old time, where t_s denotes additional time shift in order to compensate for the bias error in the velocity control. The new time reference progresses in the reverse direction. The time-shift is demonstrated in Figure 6.7. The shifted plot is given on the right. The right plot time starts with t_0 and ends with t_T . The corresponding times for the original results are given in the left plot.

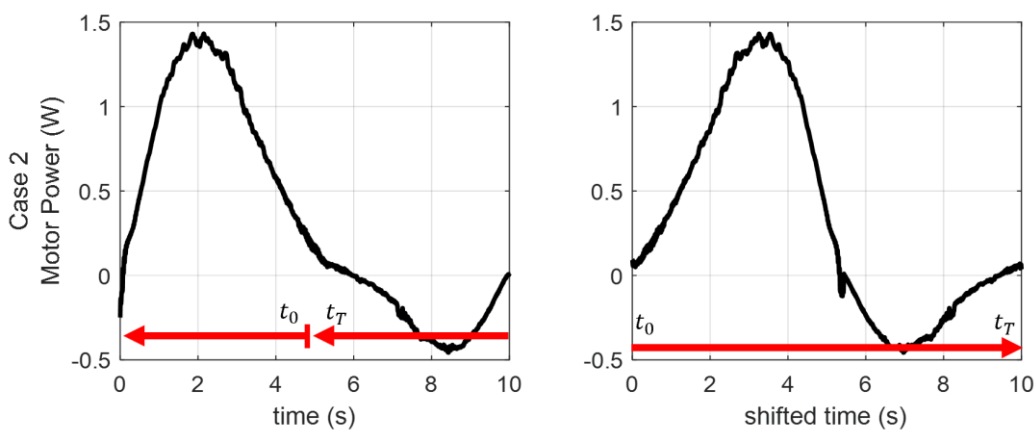


Figure 6.7. Time-shift demonstration for Case 2

In Figure 6.8 the experimental results of the motor power corresponding to Cases 1, 2 and 3 are compared. Shifted plots are used for Cases 2 and 3 as mentioned above. In the figure, it can be observed that the power profile of Cases 1,2 and 3 are similar. The total energy consumed will be analyzed in the next sections. In the right plot of Figure

6.8, $P_{motor}^e(1,1)$ is not provided since the reference speed was not be able to successfully tracked.

Comparison of motor power plots of Cases 4, 5 and 6 are given in Figure 6.9. Recall that Case 4 corresponds to the power consumption of the original mechanism without the external load. The power consumption increases when the MFG and the load are mounted in Cases 5 and 6. The increase in Case 5, where the MFG is in the prismatic joint configuration, is larger than the cylinder in slot configuration as expected. The energy consumption values of the cases will be inspected in the following section.

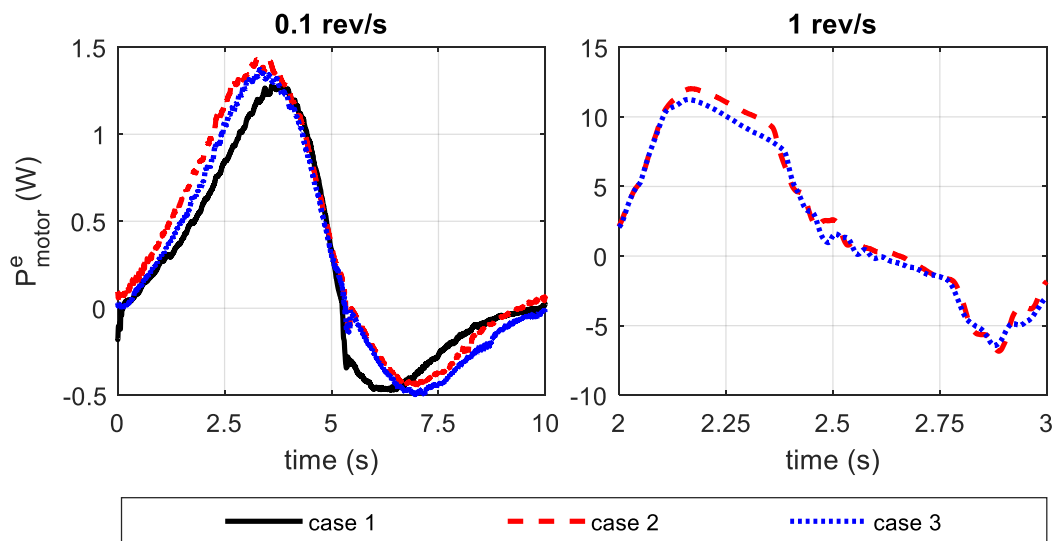


Figure 6.8. Motor output power comparison of the experimental cases 1, 2 and 3

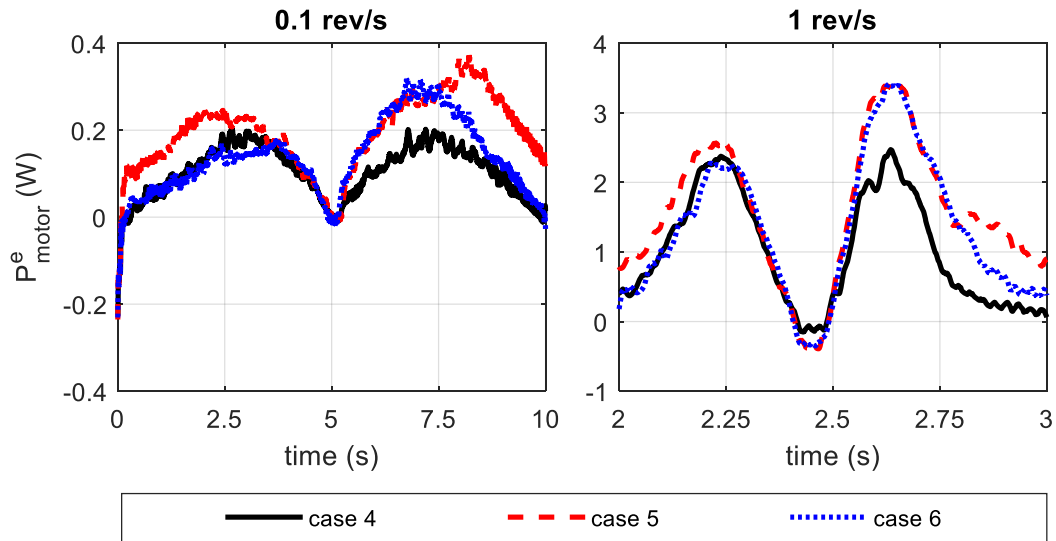


Figure 6.9. Motor output power comparison of the experimental cases 4, 5 and 6

6.6. Energy Consumption Analysis of the MFG

In this section, the energy consumption values are experimentally calculated and compared with the simulations.

6.6.1. Energy Consumption Calculation of the Experiments

Energy consumption of the mechanism (i.e., which is the work done by the motor in one period (T) of the motor shaft rotation), is calculated by integrating the motor power by using trapezoidal integration rule, i.e.,

$$E_{motor}^e(i, \omega_{ref}) = \int_0^T P_{motor}^e(i, \omega_{ref}) dt \quad (6.5)$$

Note that $E_{motor}^e(i, \omega_{ref})$ will yield the “net” energy consumption if $P_{motor}^e(i, \omega_{ref})$ becomes negative during one period.

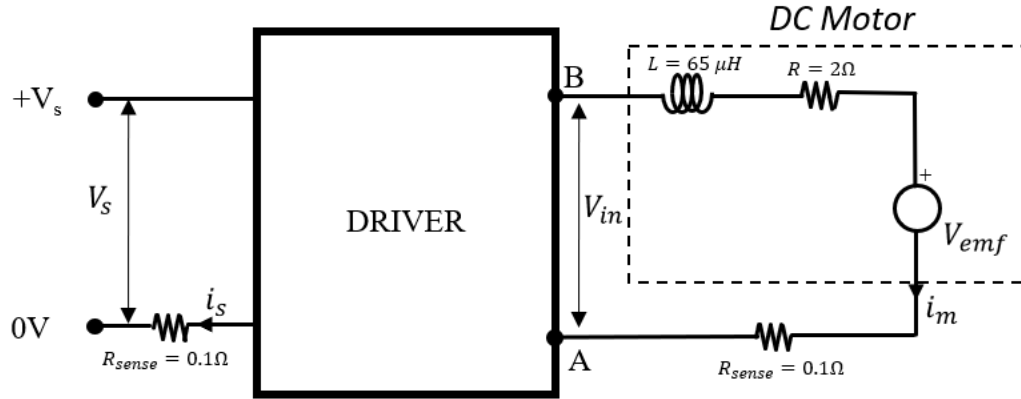


Figure 6.10. Circuit diagram for energy consumption calculation

The simulation values of the motor output energy (E_{motor}) are calculated similarly using the simulation values of the motor output power (P_{motor}), i.e.,

$$E_{motor}(i, \omega_{ref}) = \int_0^T P_{motor}(i, \omega_{ref}) dt \quad (6.6)$$

The notation, i and ω_{ref} is used to denote the experimental case number and the reference motor shaft speed, respectively. The superscript associated with e denotes, again, that the quantity is evaluated using the measurements obtained in the experiment.

The energy consumption of the motor is evaluated by integrating the absolute value of the sum of copper losses (see Section 3.2.2.1) and the motor power measurement, (since braking method of the motor is plugging type as explained in the Section 5.3.4), i.e.,

$$E_{in}^e(i, \omega_{ref}) = \int_0^T |P_{motor}^e(i, \omega_{ref}) + i_m^2(R + R_{sense})| dt \quad (6.7)$$

Note, again, that the $P_{motor}^e(i, \omega_{ref})$ may be negative. The motor torque (T_{motor}) from the dynamic force analysis is used to calculate the simulation values of the motor input energy (E_{in}) via the following equation.

$$E_{in}(i, \omega_{ref}) = \int_0^T \left| P_{motor}(i, \omega_{ref}) + \left(\frac{T_{motor}}{k_T} \right)^2 (R + R_{sense}) \right| dt \quad (6.8)$$

Recall that the motor is driven with the pulse width modulation (PWM) method, and the actual current passing through the motor has ripples in the PWM frequency. The ripples are filtered for anti-aliasing since the current reading frequency is much lower than the PWM frequency. Since the ripples cannot be measured, the copper loss calculations will be lower than the actual copper loss. In Section 3.2.2.3, the ratio between the estimated power loss using the filtered (average) current and the actual power loss is calculated. In the 50% duty case, this value may reduce down to 0.02 with the motor used in the experiment. This value can be considered to be the worst case, since the discrepancy between the RMS and the mean value of the current is maximum at 50% duty; and the ratio of the power values is even higher for low torque values since the current can have negative values as seen in Figure 3.4. If the terminal voltage between the nodes A and B could be measured, a more accurate estimation of the power consumption could be made by using the following equation.

$$E_{in}^e(i, \omega_{ref}) = \int_0^T |V_{in} i_m| dt \quad (6.9)$$

However, since V_{in} is greater than the capacity of the voltage reading hardware (which is 10 V), this method could not be used in the experiment.

The energy consumed by the power supply is denoted as $E_s^e(i, \omega_{ref})$, which is calculated by integrating the product of the constant power supply voltage (V_s) and the supply current (i_s). The supply current is read from the sense resistor placed on the return cable of the power supply as seen in Figure 6.10. Hence, one obtains

$$E_s^e(i, \omega_{ref}) = \int V_s i_s dt = V_s \int i_s dt \quad (6.10)$$

6.6.2. Comparison of the Results

Energy consumption values calculated from the simulations and from the measurements obtained in the experiments are given in Table 6.4.

Table 6.4. Energy consumption values (in Joules) of the DC motor obtained from simulations and the experiment results

case#	ω_{ref}	E_{motor}	E_{motor}^e	E_{in}	E_{in}^e	E_s^e
1	0.1	0.960	2.389	17.581	28.025	85.345
1	1	0.960	*2.462	5.294	*7.779	*11.596
2	0.1	0.960	3.333	17.591	37.071	120.608
2	1	0.960	*3.059	5.401	*8.966	*15.227
3	0.1	0.960	2.606	17.591	32.963	111.808
3	1	0.960	*2.636	5.401	*8.722	*12.117
4	0.1	0.960	1.041	1.664	3.065	19.740
4	1	0.960	1.010	1.043	1.361	5.250
5	0.1	0.960	1.926	1.664	6.293	33.616
5	1	0.960	1.569	1.051	2.038	5.854
6	0.1	0.960	1.361	1.664	4.336	25.883
6	1	0.960	1.337	1.051	1.802	5.507

*Cases where the motor could not drive the mechanism at the reference speed

Since the spring load and the inertial forces and moments are conservative, work done by these forces are zero in one period of the motion. Therefore, all of the values in Table 6.4 correspond to the energy spent for the losses in the system. The mechanical energy loss can be observed from the column of E_{motor}^e , which includes the losses in the electromechanical conversion. The sum of estimated copper losses and the braking losses can be calculated by subtracting the values of work done by the driver and the

work done by the motor, i.e., by calculating $E_{in}^e - E_{motor}^e$. As discussed in the previous section, the copper losses are estimated values since the current ripples are not taken into account. Losses on the driver can be calculated by subtracting the work done by the power supply and the work done by the driver, i.e., by calculating $E_s^e - E_{in}^e$. Note that this value contains the estimation errors of the copper losses as explained in previous subsection.

In Table 6.4, one may immediately observe that the simulation results of work done by the motor (E_{motor}) are the same for all cases and for all reference speeds. This is due to the fact that external forces used in the simulations are not dependent on the reference speed of the motor shaft, (the forces depend only on the position and the direction of the motion of links 2 and 4). Furthermore, since the frictional losses are not considered in the MFG, the simulation results corresponding to the work done by the motor are the same for all cases and reference speeds.

The difference $E_{motor}^e - E_{motor}$ corresponds to the frictional losses that are not modeled in the machine. For example, one can see that the difference in case 4 with 0.1 rev/s reference speed is $E_{motor}^e(4,0.1) - E_{motor}(4,0.1) = 1.041 - 0.960 = 0.081 J$, which is very small. This can also be confirmed visually, by checking the power consumption plots given in Figure 6.6. It is evident that as the load on the machine increases, the difference of the energy consumption between the experimental and the simulation values increase. The increase in the difference is due to the increase in Coulomb friction acting on the joints (as the reaction forces and the moments on the joints increase). For the cases with the same reference speed, viscous friction effects can be considered to be the same.

One may also calculate the additional friction due to the spring load by calculating the difference of energy consumptions in different cases. For example, the additional frictional work by mounting load spring at 0.1 rev/s may be obtained as given in the following equation.

$$E_{motor}^e(1,0.1) - E_{motor}^e(4,0.1) = 2.389 - 1.041 = 1.348 \text{ J} \quad (6.11)$$

In the table, one can see that the energy consumption of Cases 4, 5 and 6 with 1 rev/s reference motor shaft speed are smaller than the cases with 0.1 rev/s. This is related to the increased motor efficiency at higher motor shaft speeds.

The vast difference between the power supply output energy (E_s^e) and the work done by the motor (E_{motor}^e) can be explained with the low performance of the driver and the error in the copper loss calculations. Note that in Case 1 with 0.1 rev/s reference speed, the motor duty around $t=4\text{s}$ is 100% as can be seen in Figure 6.4. Since current ripple does not exist when the duty is 100%, one may calculate the potential drop, denoted as V_{drop} , as follows.

$$\begin{aligned} V_{drop} &= V_s - V_{in} \\ &= V_s - V_{emf} - i_m(R + R_{sense}) \\ &= V_s - k_E \omega - i_m(R + R_{sense}) \end{aligned} \quad (6.12)$$

$$\begin{aligned} &= 16V - 0.947 \frac{V}{rad/s} \cdot (0.1 \cdot 2\pi rad/s) - (2.46A) \cdot (2.1\Omega) \\ &= 10.23V \end{aligned}$$

It is seen that most of the energy is lost on the driver, since it has a very high voltage drop. Note that the above calculation is only valid when there is no current ripple and the motor duty is 100%. Thus, it would not be meaningful to use it to calculate the energy loss of the driver.

It is evident that the loss associated with the driver is very large. From the datasheet of the driver [19], it can be seen that the device allows up to 2A of continuous operation (without application of a heatsink). In the experimental setup, there is a heatsink on the driver. However, the current passing through the driver is still high. The potential drop across the driver is due to the drop across its components, which are transistors and diodes.

As the experiments are repeated to obtain meaningful results, it has been observed that the same power supply voltage was not enough after some time. In the first trial, Case 1 with 0.1 rev/s reference speed could be operated with 14 V on the power supply. However, as the tests has been repeated, the performance of the system decreased and the initial supply voltage (14 V) was not enough to perform the same experiment. Therefore, the supply voltage has been increased to 16 V. This shows the reduction in the performance of the driver and/or the motor as the experiments are repeated.

As the load on the machine increases, the energy output of the power supply (E_s^e) increases as expected. This can be observed by comparing Cases 1, 2, and 3 with Case 4.

One can also compare the energy consumptions of the MFG by using Table 6.4. The table clearly indicates that the configuration with the prismatic joint, denoted as (MFG)P, has a higher energy consumption compared to the cases with the cylinder in slot joint, denoted as (MFG)C (see Section 1.3.2.3 for further definition of the MFG configurations).

6.7. Maximum Torque and Maximum Power Results

Maximum values of T_{motor} , T_{motor}^e , P_{motor} and P_{motor}^e are given in Table 6.5. The calculations based on the experiments are given with the superscript e in the table. In the calculation of the torques in the experiments, the motor current (i_m) is multiplied with the torque constant (k_T) and then the values are smoothed with 101 point Moving Average Filter, i.e.,

$$T_{motor}^e(i, \omega_{ref}) = k_T i_m \quad (6.13)$$

The experimental power (P_{motor}^e) calculation is given in Section 6.5.1. The simulation torque and power values (T_{motor} , P_{motor}) are obtained from the dynamic force analysis as discussed in Section 6.5.2.

In Table 6.5, the results for the 1 rev/s reference speed for the Cases 1, 2, and 3 are for information only; and they are not to be compared with the remaining cases. Recall that the motor could not drive the load at 1 rev/s reference speed.

One should note that the experimental values may change slightly when an experiment is repeated. For example, the experimental maximum torque of Case 5 in Table 6.5, has a smaller maximum torque when the reference speed is 1 rev/s. When this experiment is repeated, the values change slightly. Thus, the maximum torque value for the 0.1 rev/s reference speed can be measured larger than the value obtained for 1 rev/s reference speed. However, for the loaded cases (Cases 1, 2 and 3) the maximum values are always larger than the cases 4, 5 and 6.

Table 6.5. Maximum torque and Powers of simulations and the experiments

Case	ω_{ref}	$max(T_{motor})$ Nm	$max(T_{motor})^e$ Nm	$max(P_{motor})$ W	$max(P_{motor})^e$ W
1	0.1	1.436	2.135	0.902	1.284
1	1	1.396	*1.836	8.770	*9.002
2	0.1	1.437	2.482	0.903	1.432
2	1	1.510	*2.168	9.486	*12.023
3	0.1	1.437	2.278	0.903	1.373
3	1	1.510	*2.071	9.486	*11.254
4	0.1	0.259	0.378	0.163	0.205
4	1	0.335	0.444	2.106	2.472
5	0.1	0.259	0.646	0.163	0.372
5	1	0.346	0.601	2.176	3.449
6	0.1	0.259	0.563	0.163	0.319
6	1	0.346	0.596	2.176	3.414

*Cases where motor could not drive the mechanism at reference speed

6.8. Performance Improvement Analysis

In this section, the performance of MFG is evaluated using the previously defined performance measures. New performance measures are also defined.

6.8.1. Definition of Performance Measures

In this section, the performance of MFG with its two different configurations (i.e., (MFG)P and (MFG)C) are compared. The performance improvement is compared to the results of the simulations. In the comparison of the performances with the simulation results, the performance measures discussed in Section 3.3.2 are used. They are repeated here for convenience.

The minimization of the maximum power performance is measured via the performance measure J_P obtained from the simulations is given by

$$J_P = \frac{\max(P_{motor})}{\max(P_{task})} \quad (6.14)$$

where P_{task} is the power output of the motor when MFG is not connected to the machine.

The experimental performance measure J_P^e (i.e., which corresponds to the minimization of the maximum motor power output) is obtained using the following equation.

$$J_P^e = \frac{\max(P_{motor}^e(i, 0.1))}{\max(P_{motor}^e(1, 0.1))}$$

where; (6.15)

$i = 5$ for prismatic joint configuration of MFG

$i = 6$ for cylinder in slot joint configuration of MFG

The minimization of the maximum torque performance is measured via the performance measure J_T is given by

$$J_T = \frac{\max(T_{motor})}{\max(T_{task})} \quad (6.16)$$

Similarly, T_{task} is the motor torque when MFG is not connected to the machine.

The experimental performance measure J_T^e (i.e., which corresponds to the minimization of the maximum motor torque) is obtained using the following equation.

$$J_T^e = \frac{\max(T_{motor}^e(i, 0.1))}{\max(T_{motor}^e(1, 0.1))}$$

where; (6.17)

$i = 5$ for prismatic joint configuration of MFG

$i = 6$ for cylinder in slot joint configuration of MFG

The minimization of the motor input energy (minimization of the copper losses) performance is measured via the performance measure J_E is given by

$$J_E = \frac{\int_0^T T_{motor}^2 dt}{\int_0^T T_{task}^2 dt} \quad (6.18)$$

The experimental performance measure J_E^e (i.e., which corresponds to the minimization of the copper losses) is obtained using the following equation.

$$J_E^e = \frac{\int_0^T T_{motor}^e(i, 0.1)^2 dt}{\int_0^T T_{motor}^e(1, 0.1)^2 dt}$$

where; (6.19)

$i = 5$ for prismatic joint configuration of MFG

$i = 6$ for cylinder in slot joint configuration of MFG

Using the experimental data, additional performance measures are introduced. The improvement in the motor output energy obtained by applying the MFG is measured via the performance measure J_M^e given by

$$J_M^e = \frac{E_{motor}^e(i, 0.1)}{E_{motor}^e(1, 0.1)} \quad (6.20)$$

where;

$i = 5$ for prismatic joint configuration of MFG

$i = 6$ for cylinder in slot joint configuration of MFG

The performance improvement in the input energy of the motor obtained by applying the MFG is measured via the performance measure J_{in}^e given by

$$J_{in}^e = \frac{E_{in}^e(i, 0.1)}{E_{in}^e(1, 0.1)}$$

where;

(6.21)

$i = 5$ for prismatic joint configuration of MFG

$i = 6$ for cylinder in slot joint configuration of MFG

The performance improvement in the output energy of the power supply obtained by applying the MFG is measured via the performance measure J_s^e given by

$$J_s^e = \frac{E_s^e(i, 0.1)}{E_s^e(1, 0.1)}$$

where;

(6.22)

$i = 5$ for prismatic joint configuration of MFG

$i = 6$ for cylinder in slot joint configuration of MFG

6.8.2. Evaluation of the Performance Measures

Performance measures obtained by the simulation and the experiments at 0.1 rev/s reference speed are given in Table 6.6 using the Cases 1, 5 and 6. The performance measures of the experiments cannot be applied to the results with the 1 rev/s reference speed cases since the control of the speed could not be tracked. However, the simulation values for 1 rev/s are given in Table 6.7. Comparing the simulation performances of the 1 rev/s cases in Table 6.7 with the 0.1 rev/s cases in Table 6.6, one can easily observe that as the reference speed is increased, the inertial forces of the system reduce the performance of the MFG.

Table 6.6. Performance indices of the simulations and experiments at $\omega_{ref} = 0.1$ rev/s using Cases 1, 5 and 6

Abbrev.	J_T	J_T^e	J_P	J_P^e	J_E	J_E^e	J_M^e	J_{in}^e	J_S^e
(MFG)P	0.180	0.302	0.180	0.290	0.052	0.183	0.806	0.225	0.394
(MFG)C	0.180	0.264	0.180	0.248	0.052	0.120	0.570	0.155	0.303

(MFG)P: Prismatic joint connection of link 3 and link 5 to ground
(MFG)C: Cylinder in slot connection of link 3 and link 5 to ground

Table 6.7. Performance indices of the simulations at $\omega_{ref} = 1$ rev/s

J_T	J_P	J_E
0.24808	0.24808	0.06443

By inspecting the experimental results in Table 6.6, it can be observed that for all cases, the application of MFG reduce the energy consumption, since the values are below 1. It can be also observed that the performance of the MFG with cylinder in slot joint is better than the MFG with the prismatic joint.

6.8.3. Comparison of MFG Performance with the Motor Braking Methods

In this section, the performance of applying an MFG to a machine is compared with the performance that will be obtained by using a DC motor with a regenerative, dynamic or plugging type braking. The braking types were discussed in Section 3.2.2.2.

In order to see if any power could be saved using dynamic or regenerative braking methods, one needs to plot the power P given by equation (3.24) versus time. The plot of P versus t for Case 1 with 0.1 rev/s reference speed is given in Figure 6.11.

Note that Case 1 corresponds to the machine with the spring load and without the MFG. From the P vs t plot in Figure 6.11, it is seen that the power is always positive. Thus, no energy could be saved by using dynamic or regenerative braking. Thus, the performance of dynamic and regenerative braking types will be the same as the plugging braking type.

Now suppose that a different motor is used such that the copper losses on the motor are negligible. For this case, the power consumption of motor with the plugging, dynamic and regenerative braking methods are given in Figure 6.12.

The total energy consumptions of the motor by using different braking methods and by using (MFG)C are given in Table 6.8. In the last column of the table, the energy consumption of MFG with cylinder in slot configuration is given. It can be seen that the energy consumption obtained by the MFG application is much less than the energy consumptions obtained by applying dynamic or regenerative braking for this application.

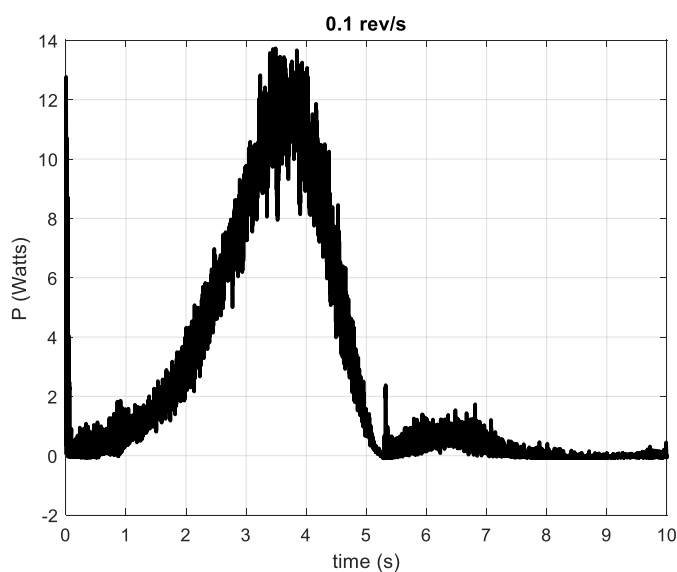


Figure 6.11. P in equation (3.24) vs time plot

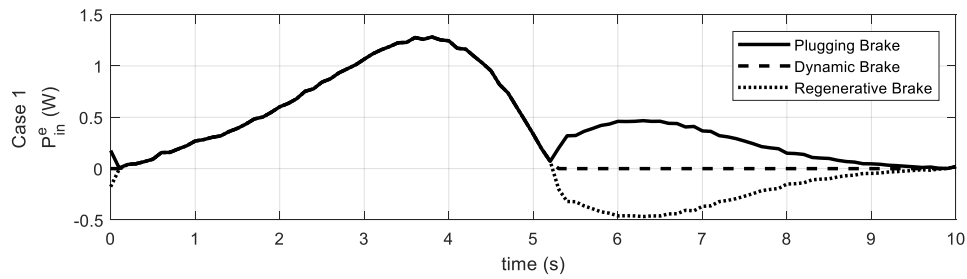


Figure 6.12. Power consumption of a motor without copper losses for different braking methods

Table 6.8. Motor energy consumption of a motor without copper losses (in Joules) for different braking methods

Plugging	Dynamic	Regenerative ($\eta = 1$)	(MFG)C
4.591	3.4899	2.3888	1.361

6.9. Additional Experiments by Using Regular MFG

In this section, in order to assess the performance improvements of a machine by applying a regular MFG [i.e., (MFG)PC, see Section 1.3.2.3], additional experiments are conducted. The experimental results for the motor power output are given in Table 6.9. Due to the changes in the performance of the components of the experimental setup (i.e., wear in driver, motor and mechanical components due to transportation and excessive testing), some experiments that were previously performed are repeated. The change in the performance can be observed by comparing the energy consumption of the machine in Table 6.9 with Table 6.4. From Table 6.9, comparing the energy consumption values when the MFG is applied to the machine (i.e., last three rows on the table), it can be inferred that (MFG)P has the highest and the (MFG)C has the lowest energy consumption. The order of the energy consumptions (i.e., the frictional losses) of the three MFG configurations are as expected. This is due to the fact that the conditions mentioned in Section 1.3.2.3 hold approximately.

Some performance indices (given in Section 6.8.2) of the experiments are given in Table 6.10. It can be observed that the performance indices of the three MFG configurations are in the expected order as well.

Table 6.9. Work done by motor in one period (in Joules)

Load	MFG Configuration	E_{motor}^e
Yes	Not Applied	2.508
No	Not Applied	1.320
Yes	(MFG)P	1.998
Yes	(MFG)PC	1.879
Yes	(MFG)C	1.556

Table 6.10. Performance indices obtained from experiment results

Abbrev.	J_E^e	J_M^e	J_{in}^e	J_s^e
(MFG)P	0.176	0.797	0.219	0.398
(MFG)PC	0.169	0.749	0.211	0.385
(MFG)C	0.136	0.620	0.173	0.329

6.10. Discussion of Results

In this chapter, it has been shown, experimentally, that the energy consumption of a machine can be reduced extensively by using a properly designed MFG. Furthermore, the maximum torque and the maximum power requirement of the motor are also reduced.

Recall that the motor in the experiment could not drive the machine for a reference speed of 1 rev/s without the application of the MFG. However, when the MFG is coupled to the machine, it was possible to drive the machine (using the same motor) for the reference speed of 1 rev/s. Hence, it has been demonstrated that a machine can be operated with less powerful motors by using the MFG.

The same slot design has been used for different speeds. However, as the reference speed increases, a decrease in the MFG performance is observed. This is due to the

increase in the inertial forces and inertial moments of the links of the MFG and the machine.

Note that the inertial forces and moments have not been taken into account while designing the MFG. If the inertial forces and moments are taken into account during the design, however, it will be possible to obtain better performance improvements by coupling the MFG to the machine. Note also that the loading on the MFG that is used in the experiments is not ideal (since the external forces are not balanced). Furthermore, center of masses of link 2 and link 4 of the MFG are not ideally located. Hence, the frictional losses associated with the MFG are higher than the frictional losses that would occur in an appropriately designed MFG.

Finally, it has been observed that the frictional losses (due to the differences in realizing the designed MFG parameters, i.e., differences in kinematic dimensions) of the three MFG configurations are in expected order. The frictional losses of the (MFG)C is the minimum, the losses of the (MFG)P is the maximum, and the losses of the (MFG)PC is in between these two.

CHAPTER 7

CONCLUSIONS

In the first chapter, the model for MFG has been introduced. The necessary special kinematic dimensions and the constraints to be satisfied by the external forces have been discussed. Open slot profile, closed slot profile, one-sided and two-sided slots have been defined. Alternative configurations of MFG, depending on the joint type between the slot profile links (link 3 and 5) and the ground link have been discussed. The conditions for the alternative MFG configurations to be kinematically equivalent have been stated. It has been pointed out that if the aforementioned conditions are satisfied “approximately”, then the frictional losses will be maximum for the overconstrained MFG [i.e., (MFG)P], and minimum for the relaxed MFG [i.e., (MFG)C]. Furthermore, the frictional losses for the regular MFG [i.e., (MFG)PC] will be somewhere in between (MFG)P and (MFG)C. In Chapter 6, the frictional losses of these three configurations have been experimentally compared and it has been observed that the magnitude of the frictional losses corresponding to the three configurations are in the expected sequence.

In the second chapter, already existing MFG parameter design methods have been improved and the equation of motion for the spring elongation has been derived. In addition to extension and compression springs, extension springs with an initial tension have also been included in the equation. By inspecting this equation, it has been concluded that either extension or compression spring can be used to obtain a given MFG power variation. Moreover, using this equation, a necessary condition for the existence of a physically realizable solution is obtained. A parameter design algorithm is proposed. In this study, an iterative method to solve the equation of motion of spring elongation (which is a non-linear ordinary differential equation) has been used. It has been pointed out that this algorithm is inefficient when the inputs of the equation are discontinuous or when the inertial parameters of the MFG are large.

In the third chapter, methods to obtain the optimum MFG power variation (which is an input to the MFG parameter design) have been introduced. Firstly, the energy balance equations associated with power losses of the components of the system have been identified. Using the balance equations, three optimization methods have been proposed. The first optimization method minimizes the maximum power output of the motor, the second method minimizes the maximum torque output of the motor and the last one minimizes the copper losses of the motor. Although the outputs of these optimization methods satisfy the first constraint on the MFG power output, they may not satisfy the second one (see Section 1.2.5 for the definition of the constraints). Compensation methods have been proposed to modify the MFG power variation such that both constraints are satisfied. It has been shown theoretically that, after the application of MFG, the mechanical power output of the motor is always positive. Thus, dynamic and regenerative braking methods are not required. Moreover, it has been shown that when the angular speed of the motor shaft is constant, then the obtained MFG power output is the same for all of the three optimization methods proposed in this study.

Furthermore, in the third chapter, a method to predict the slot profile type (open or closed) has been introduced (by using motion of the input links and MFG power variation). A method to obtain an approximate MFG power variation (if the MFG power variation leads to a close slot profile) that will lead to an open slot profile has been proposed. Note that an open slot profile is preferable since it is easier to manufacture. The proposed method is applicable only when the magnitude of the velocity of link 2 is a single-valued function of the position of link 2. The proposed method may be improved by obtaining an optimum MFG power variation that will lead to an open slot profile.

The optimization methods and the proposed modification method for the MFG power variation such that one obtains an open profile have been applied to a mathematical case study of the previous work [4]. The results have been compared with the results obtained in the previous work and it has been shown that better results may be obtained

by using the methods derived in this study. It has been found that the required maximum torque output, the maximum power output, and the energy consumption of the motor driving the machine reduce to 5% of their respective values when compared with the case where the machine is driven by the motor only (i.e., without the MFG). Hence, it is evident that one may use smaller motors to perform the same task. Moreover, the cost of energy consumed by the motor decreases by the application of MFGs.

In the fourth chapter, the case study related to the experiment has been analyzed. The model of the symmetrical slider-crank mechanism (i.e., the machine) is introduced. Due to the practical constraints, the sliders of the slider-crank mechanism are shared with the input links of the MFG. Using the methods given in Chapters 2 and 3, MFG for the case study has been designed. It has been shown that one may obtain smaller and lighter slot profile links by increasing the initial MFG spring preload. However, by doing so, it has been observed that the normal forces that the rollers apply on the slot profile links increase.

In the fifth chapter, the experimental setup has been discussed. The hardest challenge in the realization has been the small size constraints. This constraint has been dealt with by using thin, short links and small bearings. Several options to adjust the slider masses and the spring between the slider links of the machine have been provided. Although it is possible, varying the mass of the slider has not found feasible since one needs to disassemble the whole symmetrical slider-crank mechanism. This may be realized in future works. The friction on MFG's slider rails has been decreased by reducing the preload. Misalignment of the slider rails has been reduced. MFG slot profile links have been designed such that the joints connecting the ground link to links 3 and 5 can be selected to be either a cylinder in slot or a prismatic joint. As a result, performances of alternative MFG configurations have been compared experimentally.

In order to increase the accuracy of the experiments, the electronic hardware and the DC motor used in the experimental setup have been modified. Real-time control, with 1 kHz frequency, has been achieved. In order to improve the velocity readings, a first order filter has been used. PI control has been used to control the velocity of the motor shaft. In the case of 0.1 rev/s reference speed, a maximum of 10% percent velocity error has been obtained. In the case of 1 rev/s, a maximum of 1% velocity error has been obtained. The performance degradation in 0.1 rev/s speed has been related to the encoder resolution and the quality of the velocity estimation method. A compact software has been designed to run the experiment. The main script calls an executable (.exe) to read currents, then sends commands to the microcontroller, retrieves data and processes it.

In the sixth chapter, the experiments that have been conducted for various configurations have been discussed. The experiments indicate that the conservative external load applied on the machine could be compensated by MFG. It has also been observed that the motor can drive greater external loads by the application of MFG. The experiments indicate that, the same slot profile links may be used with different reference speeds (with a reduced performance, which depends on the values of the inertial forces of the machine and the MFG links) if the load is not velocity dependent.

As future work, one may investigate the performance improvements of a machine having non-conservative loads, with the application of MFG. Performance of MFGs with closed and open slot profiles may be compared experimentally. One may also experimentally investigate the symmetrical control of twin machines and merging methods to couple MFGs with the machines.

REFERENCES

- [1] R. Soylu, "A Mechanical Force Generator and Related Kinematic Chains, " T.R. Patent WO/2015/069207, Application Number: 2013/13064, PCT/TR2014/000413, 2013. (Pending)
- [2] R. Soylu and H. Mencek, "An Overconstrained, Energy Efficient, Shaking Force Free Mechanical Force Generator and Related Mechanisms - Part 1: Mechanical Force Generator," (to be published).
- [3] H. Mencek, "Theoretical and Experimental Dynamic Performance Optimization of Planar Mechanisms Using Adjustment Systems and Mechanical Generators," Ph. D. Thesis, Middle East Technical University, 2015.
- [4] U. Erdinç, "Practical Application of Overconstrained Machines with Favorable Dynamic Properties," M. Sc. Thesis, Middle East Technical University, 2017.
- [5] J. E. Shigley, *Mechanical Engineering Design 5th Ed.* McGraw-Hill 1989.
- [6] R. Soylu and H. Mencek, "An Overconstrained, Energy Efficient, Shaking Force Free Mechanical Force Generator and Related Mechanisms - Part 3 : Dynamic Force Analysis," (to be published).
- [7] Electro-Craft Corporation U.S.A., *DC Motors Speed Control Servo Systems*, Pergamon Press 1977.
- [8] Product Application Note 178, Reduction of PWM power losses using additional inductances. [Online]. Available: https://www.faulhaber.com/fileadmin/user_upload_global/support/MC_Support/Drive_Electronics/AppNotes/Faulhaber_AN178_EN.pdf. [Accessed: 26-Jul-19].
- [9] PWM Power Stage, Current Ripple and External Motor Chokes. [Online]. Available: https://support.maxongroup.com/hc/en-us/article_attachments/360009984893/ENGLISH_MotorChokeCalculation_V1-00en.pdf [Accessed: 28-Jul-19].

- [10] H. B. Hamilton, “Losses in Chopper-Controlled DC Series Motors” University of Pittsburgh, 1982
- [11] FAULHABER, DC-Micromotors Series 2342 ... CR. [Online]. Available: <https://www.faulhaber.com/en/products/series/2342cr/>. [Accessed: 26-Jul-19].
- [12] D.E. Kirk. *Optimal Control Theory*, Dover Publications 1970
- [13] C. R. de Boor, *A Practical Guide to Splines*. Springer-Verlag, New York: 1978.
- [14] R. Baraniuk, *Signals and Systems*. Rice University 2003.
- [15] HIWIN, Linear Guideway Technical Information. [Online]. Available: https://www.hiwin.com/pdf/linear_guideways.pdf. [Accessed: 26-Jul-19].
- [16] E. Söylemez, *Mechanisms*. Middle East Technical University, 2013.
- [17] “Dogus Kalıp 2018 Fiyat Listesi”. [Online] Available: <http://doguskalipweb.cabiltek.com/imgsrv/Upload/files/636622627314995000.pdf>. [Accessed: 26-Jul-19].
- [18] “VEX Robotics Website”. [Online] Available: <http://www.vexrobotics.com>. [Accessed: 26-Jul-19].
- [19] “L298N datasheet”. [Online] Available: <https://www.st.com/resource/en/data-sheet/l298.pdf>. Accessed: [Accessed: 26-Jul-19].
- [20] N. Mohan, T. M. Undeland and W. P. Robbins, *Power Electronics, Converters, Applications and Design 2nd Ed.* John Wiley & Sons 1995.
- [21] “Introduction to Arduino”, [Online] Available: <https://www.arduino.cc/en/Guide/Introduction>. [Accessed: 26-Jul-19].
- [22] Sparkfun, Serial Communication, [Online] Available: <https://learn.sparkfun.com/tutorials/serial-communication/all>. [Accessed: 26-Jul-19].
- [23] H. A. Toliyat and G. B. Kliman, *Handbook of Electrical Motors 2nd Ed.* CRC Press, 2004

[24] A. Tilli and M. Montanari, "A Low-Noise Estimator of Angular Speed and Acceleration from Shaft Encoder Measurements" *ATKAAF*. 42. 169-176 (2001).

APPENDICES

A. CAD Drawing of Symmetrical Slider Crank Machine with MFG

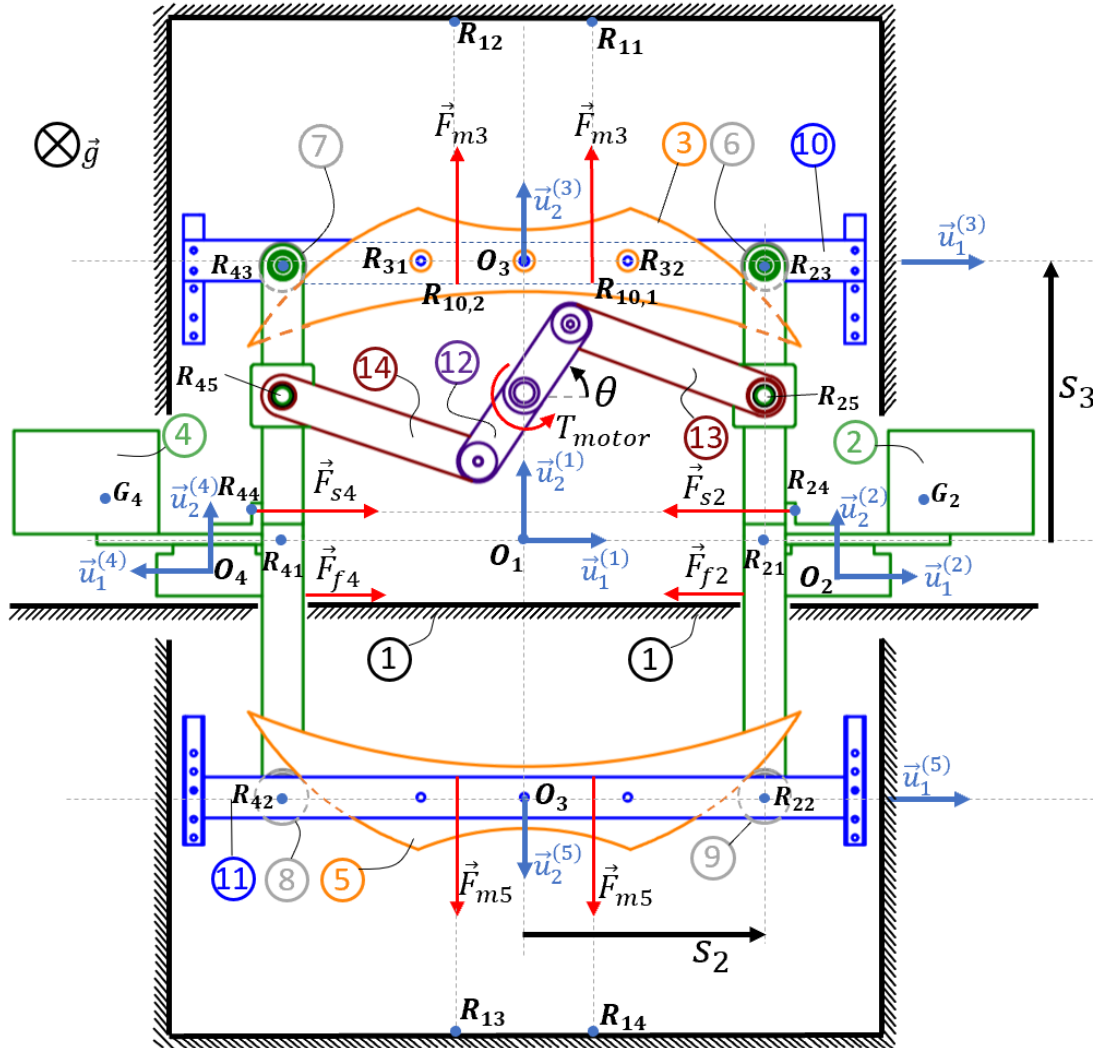


Figure A.1. Front view of the system from the CAD drawing

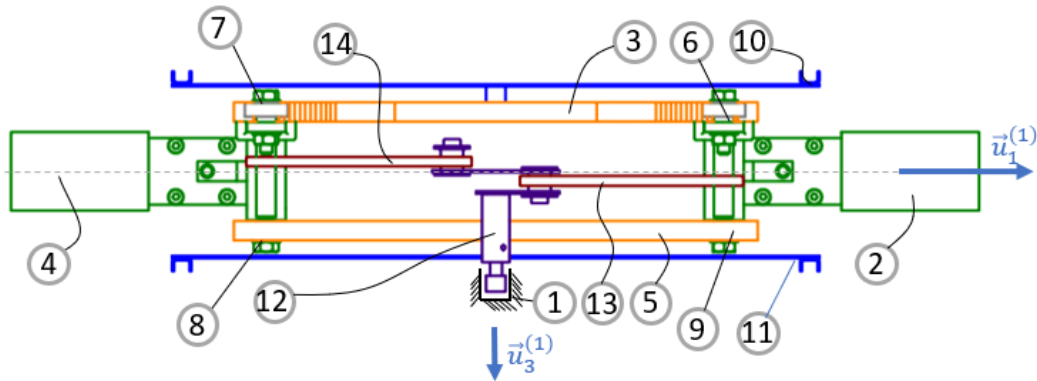


Figure A.2. Top view of the system from the CAD drawing

Front and top views of the links from the CAD model of the experimental setup is given in Figure A.1 and Figure A.2, respectively. When link 3 in Figure A.2 is connected to link 10 rigidly, link 3 used in the MFG design (see Figure 1.1) is considered connected to the ground link by means of a prismatic joint. If the joint between link 3 and link 10 is a revolute joint from the reference point O_3 in Figure A.2, then in MFG design link 3 has cylinder in slot connection to ground link. In Figure A.2, link 3 is connected to link 10 by a pin on O_3 , such that link 3 can rotate with respect to ground link. To rigidly connect links 3 and 10, extra pins are connected to R_{31} and R_{32} in Figure A.1. The same applies to link 5.

B. Important Dimensions of the MFG from CAD file

Important dimensions of link 2 of the MFG is given in Figure B.1. For the dimensions of link 3, one should calculate the slot profile centerline in Section 4.6.1.2.

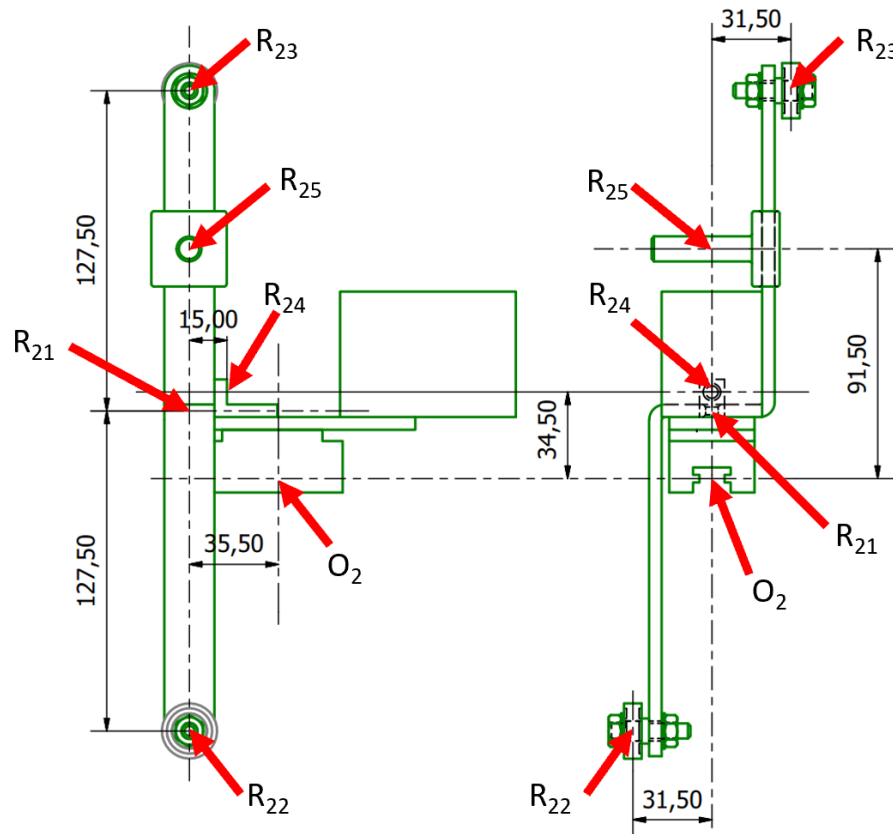


Figure B.1. Front view of the system from the CAD drawing